UNIVERSITY OF CALIFORNIA, SAN DIEGO

Investigation of Proton Focusing and Conversion Efficiency for Proton Fast Ignition

A dissertation submitted in partial satisfaction of the
requirements for the degree
Doctor of Philosophy

in

Engineering Sciences (Engineering Physics)

by

Teresa Jean Bartal

Committee in charge:

Farhat Beg, Chair
Fred Driscoll
Sergei Krasheninnikov
Pravesh Patel
Cliff Surko
George Tynan

2012

The dissertation of Teresa Jean Bartal is approved, and it is acceptable in quality and form for publication on microfilm and electronically:

_____

_____

_____

_____

_____

_____
Chair

University of California, San Diego

2012

DEDICATION

To my Grandpa, my hero.

TABLE OF CONTENTS

LIST OF FIGURES

LIST OF TABLES

ACKNOWLEDGEMENTS

This thesis would not be possible without the support of my academic advisor Prof. Farhat Beg. Over five years ago he had enough faith in me to bring me on as a graduate student at UCSD. During my years as a graduate student, I am thankful for his guidance and support in order to reach my goal of obtaining a Ph.D. Also, I would not have gotten this far in my academic career if it wasn't for the help and guidance of my technical advisor Pravesh Patel at Lawrence Livermore National Laboratory. Thank you for the long discussions about physics and life. In addition, thanks to Mark Foord at Lawrence Livermore National Laboratory for performing the simulations to go along with the experimental data in this thesis. The physics story would not have been complete without the simulations. Thanks to Mike Key for pushing me to think outside of the box, challenging my findings, and making me a better physicist.

During my time as a graduate student, I am thankful that I have had the opportunity to perform research at a national laboratory, work with some amazing scientists and developed friendships that helped me throughout my journey. Most of the data collected for this thesis would not be possible without the help of the Trident team at Los Alamos National Laboratory: David Montgomery, Randy Johnson, Tom Shimada, Ray Gonzales, Shaw-Marie Reid, Fred Archuleta, Cort Gautier, Sam Letzring, and Tom Hurry. A special thanks is given to Kirk Flippo, Sandrine Gaillard, and Dustin Offermann. Thank you for the long hours and your hard work to make the experiments happen. Most of all, thanks for the friendships that were created along the way.

Thank you to my experimental collaborators and colleagues who helped me in some way, shape, or form: Claudio Bellei, Sugreev Chawla, Hui Chen, Emilio Giraldez, Daniel Hey, Drew Higginson, Charlie Jarrott, Sebastien Le Pape, Andrew MacPhee, Derek Mariscal, Harry McLean, John Pasley, Bin Qiao, Markus Roth, Richard Stephens, Mingsheng Wei, and Toshi Yabuuchi. To Sophia Chen, Tammy Ma, Cliff Chen and Tony Link: thank you for making the long hours spent in the laboratory and the rough patches throughout graduate school a more bearable. Thanks to Simon Bott for the much needed coffee breaks and letting me walk into

his office anytime for help or just to chat about life. When analyzing data for months on end, those moments helped me keep my sanity.

Last, but not least, thank you to my friends and family for all your love and support. To my mom and dad, thanks for always encouraging me to pursue a higher education even when it involved me moving to the other side of the county. Most of all, thanks to my loving husband who supported me throughout the last four years. Even through the challenges of grad school and driving me to the airport a countless number of times (he could probably drive to the airport with his eyes closed now), thank you for sticking by my side and asking me to become your wife; changing my life forever. Thank you for your unending love and words of encouragement.

This work was performed under the auspices of the U.S. Department of Energy by Lawrence Livermore National Laboratory under Contract DE-SC0001265.

Chapter 5 contains material that is partially a reprint of the material as it appears in **T. Bartal**, K. A. Flippo, S. A. Gaillard, D. T. Offermann, M. E. Foord, C. Bellei, P. K. Patel, M. H. Key, R. B. Stephens, H. S. McLean, L. C. Jarrott and F. N. Beg, "Proton focusing characteristics relevant to Fast Ignition," *IEEE Transactions on Plasma Science*, Vol. 39, Issue 11, part 1, p. 2818-2819, 2011 and **T. Bartal**, M. E. Foord, C. Bellei, M. H. Key, K. A. Flippo, S. A. Gaillard, D. T. Offermann, P. K. Patel, L. C. Jarrott, D. P. Higginson, M. Roth, A. Otten, D. Kraus, R. B. Stephens, H. S. McLean, E. M. Giraldez, M. S. Wei, D. C. Gautier, and F. N. Beg, "Focusing of short pulse high intensity laser accelerated proton beams," *Nature Physics*, Vol. 8, p. 139-142, February 2012. The dissertation author was the primary investigator and author of these papers.

VITA

2006	B.A. in Physics, Goshen College
2008	M.S. in Engineering Sciences (Engineering Physics), University of California, San Diego
2012	Ph.D. in Engineering Sciences (Engineering Physics), University of California, San Diego

PUBLICATIONS

T. Bartal, M. E. Foord, C. Bellei, M. H. Key, K. A. Flippo, S. A. Gaillard, D. T. Offermann, P. K. Patel, L. C. Jarrott, D. P. Higginson, M. Roth, A. Otten, D. Kraus, R. B. Stephens, H. S. McLean, E. M. Giraldez, M. S. Wei, D. C. Gautier, and F. N. Beg, "Focusing of short pulse high intensity laser accelerated proton beams," *Nature Physics* **8**, p. 139-142 (2012).

T. Bartal, K. A. Flippo, S. A. Gaillard, D. T. Offermann, M. E. Foord, C. Bellei, P. K. Patel, M. H. Key, R. B. Stephens, H. S. McLean, L. C. Jarrott and F. N. Beg, "Proton Focusing Characteristics Relevant to Fast Ignition," *IEEE Transactions on Plasma Science* **39**, Issue 11, part 1, p. 2818-2819 (2011).

T. Yabuuchi, H. Sawada, **T. Bartal**, D. Batani, L. Gizzi, M. Key, A. Mackinnon, H. McLean, P. Norreys, P. Patel, R. Stephens, C. Spindloe, W. Theobald, M. Wei, and F. Beg, "Proton radiography of intense laser irradiated wire- attached cone targets," *IEEE Transactions on Plasma Science* **39**, no. 11, pp. 28222823 (2011).

D. T. Offermann, K. A. Flippo, J. Cobble, M. J. Schmitt, S. A. Gaillard, **T. Bartal**, D. V. Rose, D. R. Welch, M. Geissel, and M. Schollmeier, "Characterization and focusing of light ion beams generated by ultra-intensely irradiated thig foils at the kilojoule scale," *Phys. Plasmas* **18**, 056713 (2011).

D. P. Higginson, J. M. McNaney, D. C. Swift, **T. Bartal**, D. S. Hey, R. Kodama, S. Le Pape, A. Mackinnon, D. Mariscal, H. Nakamura, N. Nakanii, K. A. Tanaka, and F. N. Beg, "Laser generated neutron source for neutron resonance spectroscopy," *Phys. Plasmas* **17**, 100701 (2010).

K. U. Akli, P. K. Patel, R. Van Maren, R. B. Stephens, M. H. Key, D. P. Higginson, B. Westover, C. D. Chen, A. J. Mackinnon, **T. Bartal**, F. N. Beg, S. Chawla, R. Fedosejevs, R. R. Freeman, D. S. Hey, G. E. Kemp, S. Le Pape, A. Link, T. Ma, A. G. MacPhee, H. S. McLean, Y. Ping, Y. Y. Tsui, L. D. Van Woerkom, M. S. Wei, T. Yabuuchi, and S. Yuspeh, "A Dual Channel X-Ray Spectrometer for Fast Ignition Research," *Journal of Instrumentation* **5**, P07008 (2010).

D. S. Hey, M. E. Foord, M. H. Key, S. L. LePape, A. J. Mackinnon, P. K. Patel, Y. Ping, K. U. Akli, R. B. Stephens, **T. Bartal**, F. N. Beg, R. Fedosejevs, H. Friesen, H. F. Tiedje, and Y. Y. Tsui, "Laser-Accelerated Proton Conversion Efficiency Thickness Scaling," *Phys. Plasmas* **16**, 123108 (2009).

C. D. Chen, P. K. Patel, D. S. Hey, A. J. Mackinnon, M. H. Key, K. U. Akli, **T. Bartal**, F. N. Beg, S. Chawla, H. Chen, R. R. Freeman, D. P. Higginson, A. Link, T. Ma, A. G. MacPhee, R. B. stephens, L. D. Van woerkom, B. Westover, and M. Porkolab, "Bremsstrahlung and Kα fluorescence measurements for inferring conversion efficiencies into fast ignition relevant hot electrons," *Phys. Plasmas* **16**, 082705 (2009).

D. T. Offermann, R .R. Freeman, L. D. Van Woerkom, M. E. Foord, D. Hey, M. H. Key, A. J. Mackinnon, A. G. MacPhee, P. K. Patel, Y. Ping, J. J. Sanchez, N. Shen, **T. Bartal**, F. N. Beg, L. Espada, and C. D. Chen, "Observations or proton beam enhancement due to erbium hydride on gold foil targets," *Phys. Plasmas* **16**, 093113 (2009).

H. Chen, N. L. Back, **T. Bartal**, F. N. Beg, D. C. Eder, A. Link, A. G. MacPhee, Y. Ping, P. M. Song, A. Throop, and L. Van Woerkom, "Absolute calibration of image plates for electrons at energy between 100 keV and 4 MeV," *Rev. Sci. Instruments* **79**, 033301 (2008).

L. Van Woerkom, K. U. Akli, **T. Bartal**, F. N. Beg, S. Chawla, S. D. Chen, E. Chowdhury, R. R. Freeman, D. Hey, M. H. Key, J. A. King, A. Link, T. Ma, a. J. Mackinnon, A. G. MacPhee, D. Offermann, V. Ovchinnidov, P. K. Patel, D. V. Schuamacher, R. B. Stephens, and Y. Y Tsui, "Fast electron generation in cones with ultraintense laser pulses," *Phys. Plasmas* **15**, 056304 (2008).

ABSTRACT OF THE DISSERTATION

Investigation of Proton Focusing and Conversion Efficiency for Proton Fast Ignition

by

Teresa Jean Bartal

Doctor of Philosophy in Engineering Sciences (Engineering Physics)

University of California, San Diego, 2012

Farhat Beg, Chair

Recent advances in generating high energy (> 50 MeV) protons from intense laser-matter interactions has opened up new areas of research, with applications in radiography, high energy density physics, and ion-proton beam fast ignition (FI). The ability to focus the proton beam has made these applications more attractive. Fast ignition (FI) is an evolved concept of conventional inertial confinement fusion (ICF). In proton FI, a collimated beam of protons is used to deliver the necessary ignition energy to the compressed Deuterium-Tritium (DT) fuel capsule instead of the original concept of a beam composed of relativistic electrons. In cone-guided FI, a cone is embedded into the side of the fuel capsule where the proton source foil is placed within the cone. The cone provides a clear path to the dense core

and protects the proton source foil from radiation during the compression of the capsule. The proton source foil is a segment of a hemispherical shell target used to help focus the proton beam to the core to spark ignition. The viability of proton FI requires focusing of the generated proton beam to a 40 μm spot at the compressed fuel and a laser to proton conversion efficiency of $\sim$15%.

Here, proton focusing and the laser to proton conversion efficiency are investigated using flat foils and hemispherical shell targets. Experiments were conducted on the 200 TW short pulse laser at Los Alamos Laboratory. The 1053 nm laser pulse delivered 70-80 J on target in 500-600 fs focused by an f/8 parabolic mirror. The generated proton beam from the target was examined by placing a mesh downstream of the target, which the proton beam would pass though and then imaged with a pack of radiochromic film (RCF). A 3D ray-tracing technique was developed to determine the focal position and focal spot size of the generated proton beam by tracing the proton trajectories from the image of the mesh collected by the RCF back through the mesh to the central axis.

The focal position calculated from the ray-tracing technique for the flat foils resulted in a real focus, contrasting the convention wisdom of a virtual focus [1]. Investigation of the proton expansion from flat foils established that initially the protons are accelerated normal to the surface, due to the fact that the electrostatic sheath field generated by the escaping hot electrons is only a few microns beyond the rear surface of the foil. As time progresses and more electrons are accelerated into the target by the laser irradiation, the sheath expands away from the rear surface of the foil, developing a bell-shaped curvature. The protons are then accelerated normal to the sheath field, which is at the leading edge of the expansion. Due to the bell-shaped curvature, protons that are accelerated further away from the central axis of the laser interaction experience gradients within the expansion causing the protons to gain radial velocity, which changes the angle of divergence of the protons. The radial velocity gained by the protons affects the trajectory of the protons, resulting in a calculated real focal position when trajectories are calculated the ray-tracing technique. The trajectories of the protons are further affected by the mounting technique. When the foils are mounted to washers for

stability, electrons accelerated in the foil escaped into the washer creating a field along the interior wall of washer. The field affects the proton trajectories near the wall and decreases the laser to proton conversion efficiency.

With the understanding gained from the flat foil targets, proton focusing is further investigated using freestanding hemispherical shell targets. Using the 3D ray-tracing technique, the calculated focal position is determined to be located inside the radius of curvature of the hemisphere, which is less than the distance of $1.7R$ (where R is the radius of curvature of the hemispherical shell) determined from proton heating experiments [2]. With the aid of particle-in-cell (PIC) simulations, using the code LSP (large-scale-plasma), it was determined that proton trajectories are not straight, but actually bend near the focal region. A hot electron pressure gradient in the expansion beam sets up a radial electric field, $E_r \approx kT_{ehot}/R$, where here R is the radial scale length of the beam and kT_{ehot} is the hot electron temperature. When the radial electric field surpasses the radial acceleration force, the proton trajectories are bent away from the focal axis.

The first demonstration of the generation and focusing of a proton beam from a hemispherical shell in a FI geometry is presented, where the beam is generated from a curved focusing surface, which propagates and is channeled via surface fields through an enclosed cone structure. A segment of a hemispherical shell is placed within a novel cone-shaped target. The proton focusing and conversion efficiency are calculated for the structured targets and are compared to the freestanding hemispherical shells. Particle-in-cell (PIC) simulations are presented for further understanding. It is clearly shown that the focusing is strongly affected by the electric fields in the beam in both open and enclosed (cone) geometries, bending the trajectories near the axis. It is also reported that in the cone geometry, a sheath electric field effectively channels the proton beam through the cone tip, substantially improving the focusing properties. The sheath electric field on the wall of the cone is generated by electrons that escape the hemispherical shell and travel into the surrounding structure. Focusing of the proton beam is improved by the sheath electric field on the wall of the cone; however, the laser to proton conversion efficiency is decreased due to the hot electrons escaping the shell reducing

the amount of energy available to accelerate the protons.

Chapter 1

Introduction

Fusion energy is a clean and abundant energy source, which involves harnessing the power of the stars here on earth. Fusion energy is generated by nuclear fusion processes. In fusion reactions, two light nuclei fuse together to create a heavier nucleus, releasing energy in the process. The amount of energy released is calculated by Einstein's energy equation, $\Delta E = \Delta mc^2$. The mass of the fused nucleus is lighter than the total mass of its constituents and the amount of energy that is released, in the form of the kinetic energy of the resulting particles, is the difference in the binding energies. The binding energy is defined as the least amount of energy required to disassemble a nucleus into the same number of free unbound neutrons and protons, in which it was composed, where the nucleons are far enough apart so that the strong nuclear force can no longer cause the particles to interact. The binding energy is the least for the isotopes of hydrogen. Table 1.1 lists the possible fusion reactions that use the isotopes of hydrogen. Fusion research mainly focuses on the interactions involving Deuterium and Tritium (DT) because of the relatively large cross-section for the reaction and the large amount of energy released at 10 keV temperatures [3]. In order for DT to fuse, the isotopes, which are positively charged, need enough kinetic energy to overcome the Coulomb repulsion force. Giving the nuclei enough kinetic energy to overcome the Coulomb barrier can be achieved by heating the material to ∼keV temperatures. Once the isotopes overcome the Coulomb forces, the attractive nuclear forces can come into play, which are effective over distances 10^{-15} m, and the nuclei can fuse, releasing

Table 1.1: Possible fusion reactions and their products.

D+T $\rightarrow \alpha$ (3.5 MeV) + n (14.1 MeV) D+D $\rightarrow$ ^{3}He (0.82 MeV) + n (2.45 MeV)

D+D $\rightarrow$ T (1.01 MeV) + p (3.03 MeV)

D+^{3}He $\rightarrow$ ^{4}He (3.6 MeV) + p (14.7 MeV)

energy. A cartoon of a fusion reaction is seen is Fig. 1.1. To achieve high gain, the

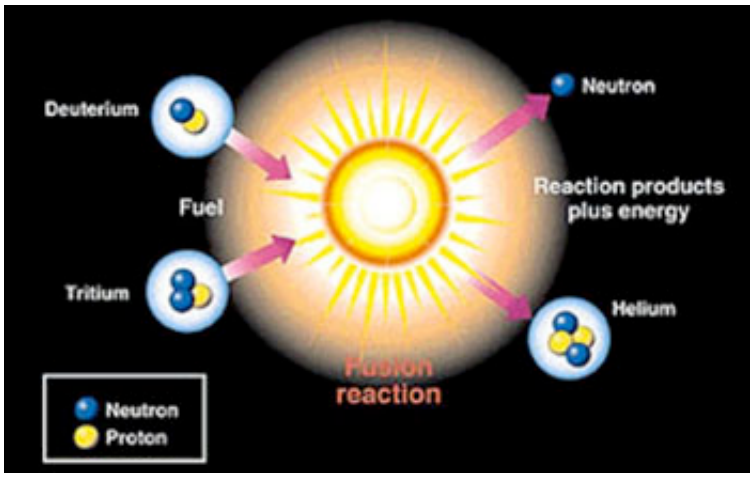

Figure 1.1: Cartoon of a DT fusion reaction. Image courtesy of Lawrence Livermore National Laboratory.

fusion reaction also needs to occur a sufficient number of times. The parameter $< \sigma v >$ is the reaction cross section, which is a measure of the reactivity of the reaction, where v is the velocity of the two nuclei, σ is the fusion cross section and the product is averaged over a Maxwellian energy distribution [4]. This quantity is proportional to the number of reactions per unit density per unit time. The reaction cross section for each fusion reaction in Table 1.1 is plotted in Fig. 1.2 for a range of temperatures. The DT reaction contributes the most to the energy yield over all temperatures.

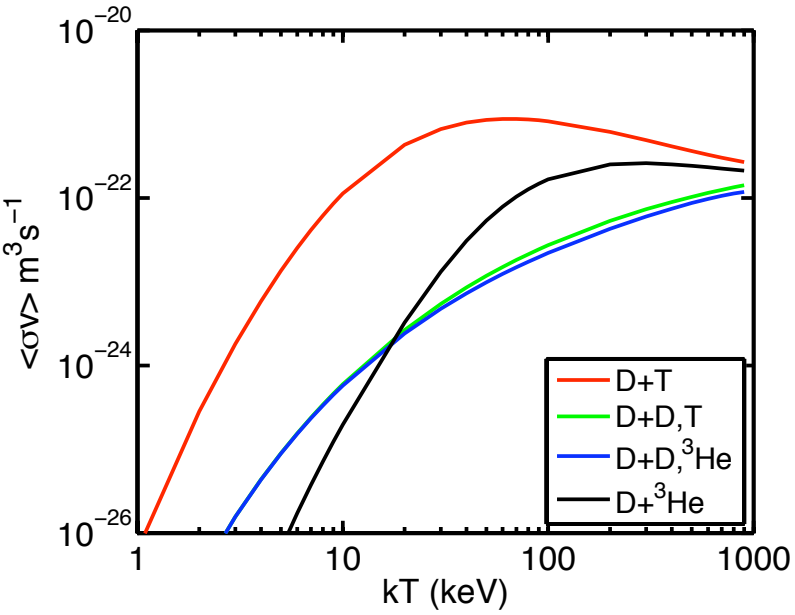

Figure 1.2: The reactivity parameter $< \sigma v >$ for each fusion reaction in Table 1.1. The D+T reaction is the reaction of choice due to the high reactivity throughout the range of temperatures. Curves constructed from data tabulated by J. R. McNally Jr. [5].

1.1 Concept of Inertial Confinement Fusion

One scheme to create fusion energy is inertial confinement fusion (ICF). In ICF, powerful lasers are used to compress and heat a fuel capsule to a temperature of $\sim$10 keV reaching a density 20 times that of lead in a confinement timescale of $\sim 10^{-10}$ s to spark ignition in a fuel capsule [6, 7]. A schematic displaying the processes in ICF is shown in Fig. 1.3. Central hot spot (CHS) ignition is the conventional process of ICF. High power nanosecond duration lasers ($> 10^{14}$ Wcm^{-2}) (direct drive) or an intense soft x-ray source (indirect drive) uniformly irradiate the outer surface of a full capsule approximately 2 mm in diameter. The target is usually a smooth, hollow spherical shell filled with low density gas ($\leq$ 1.0 mg/cm^3) with an outer layer, which forms the ablator, composed of C, Be or a polymer and an inner layer of DT ice $\sim$0.1 mm thick, which forms the main fuel [4, 7]. The irradiation ablates the outside surface of the capsule causing a

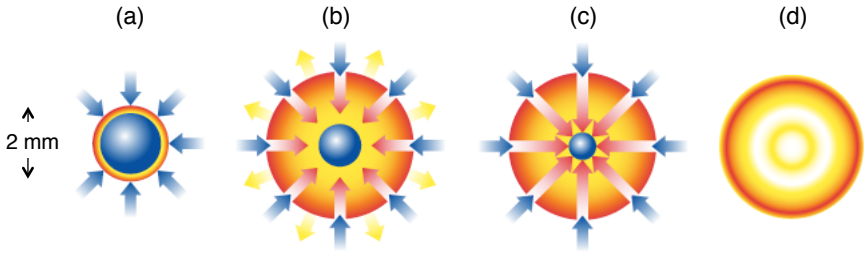

Figure 1.3: Inertial Confinement Fusion: (a) Direct laser irradiation or x-rays spherically irradiate the outer surface of a fuel capsule ∼2 mm in diameter. (b) The irradiation causes the outer surface to ablate creating a rocket-like reaction toward the center. (c) Shock waves converge on the center of the fuel capsule, heating the fuel and sparking ignition. (d) After ignition, a thermonuclear burn wave spreads radially outward to the outer surface resulting in high gain.

rocket-like reaction inward and compressing the target. The amount of work done by the imploding fuel is the product of the volume enclosed by the shell and the pressure from the ablation. A larger thinner shell that encompasses more volume can be accelerated to a higher velocity than a thicker shell of the same mass at a given pressure.

The convergence of shock waves at the center heats the low density region of the fuel formed by the implosion; this region is known as the hot spot. During the compression of the target, ignition within the hot spot needs to occur before the capsule disassembles. The confinement time, τ_C, of the capsule scales as $R/T^{1/2}$, where R is the radius of the fuel capsule and T is the temperature. In order to produce high gain with a reasonable amount of driver energy being delivered to the fuel capsule, a certain amount of the fuel in the capsule needs to be burned before the target disassembles. Tritium in the fuel is burned at a rate

$$\frac{dn_T}{dt} = -n_T n_D < \sigma v >, \tag{1.1}$$

where n_T and n_D are the density of Tritium and Deuterium, respectively. Eq. (1.1) can be converted to the total fuel burn rate by using the total fuel number density, $n = 2n_T = 2n_D$, resulting in

$$\frac{dn}{dt} = -\frac{n^2}{2} < \sigma v > . \tag{1.2}$$

Integrating eq. (1.2) from zero to the confinement time and defining the burn fraction as $f_b = 1 - n/n_0$ where n_0 is the initial density, the burn fraction can be written as

$$f_b = -\frac{\rho R}{\rho R + \beta(T)}, \tag{1.3}$$

where $\beta(T) = 8 m_{DT} c_s / < \sigma v >$, m_{DT} is the mass of the DT nucleus (2.5 AMU), ρ is the initial mass density given by $\rho = n_0 m_{DT}$, and c_s is the sound speed [8]. A burn fraction of approximately $\frac{1}{3}$ is required for high gain. To achieve the appropriate burn fraction, the assembled fuel is required to have $\rho R \approx 3\ gcm^{-2}$. The areal density requirement can be written in terms of the fuel number density and the confinement time resulting in $n\tau_C = 2 \times 10^{15}$ cm^{-3}s [8], which is referred to as the Lawson criteria for ICF. The Lawson criteria must be meet in order for ignition to occur.

The compression of the DT fuel, makes ignition feasible in the laboratory. The amount of DT that is required to achieve a burn fraction of $\frac{1}{3}$ and $\rho R \approx$ 3gcm^{-2} is given by

$$M = \frac{4\pi}{3} \frac{(\rho R)^3}{\rho^2}. \tag{1.4}$$

Therefore, for a density of 400 gcm^3 with a sphere of radius r and shell thickness of $r/2$, 5 mg of DT would yield $6{\times}10^8$ J [4]. This amount of energy is readily obtainable compared to the $3{\times}10^{14}$ J that 2.5 kg of DT with the same requirements if the DT was at the normal liquid density of 0.21 gcm^{-3}.

Even though the overall density of the fuel is high, the density of the hot spot in the center must remain low to spark ignition. At the final stage of compression of the capsule is isobaric at pressures up to $\sim$ 200 Gbars [4], where the hot spot, containing $\sim$ 2-5% of the fuel, is in pressure equilibrium with the surrounding dense fuel region comprising the rest of the mass. The shock waves created from the rocket-like reaction converge at the center of the shell heating the fuel to 10 keV, sparking ignition. Once ignition is sparked in the core, the resultant alpha particles must travel to the outer layers of the shell to create the thermonuclear burn wave. At 10 keV, if the hot spot has the areal density of $\rho_{HS} R_{HS} = 0.3$ gcm^{-2}, the 3.6 MeV alpha particles that are created in the reaction, deposit their energy into the hot spot raising the temperature to 30-40 keV [8]. This then creates

enough alpha particles which will travel into the adjacent layers of the cold, high density material, which heats up the material, resulting in a propagating burn wave to the outer surface.

In inertial confinement fusion with spherical implosion, the implosion of the shell is susceptible to hydrodynamic instabilities: in particular the Rayleigh-Taylor instability [4, 6]. Nonuniform irradiation or unevenness in the smoothness of the outer layer of the shell can be referred to as small perturbations that can grow exponentially in time. These perturbations are Rayleigh-Taylor like instabilities since they occur at the interface of fluids at different densities, where lower density material is being accelerated toward material with higher density [6]. This instability can occur during the initial implosion of the outer shell causing the shell to burst and during the final stages of the implosion where the cold fuel in the center can mix with the hot surrounding plasma, diminishing ignition. Due to the onset of the Rayleigh-Taylor instability, the process of CHS ignition requires high spherical implosion symmetry, a high degree of target smoothness and inefficiently utilizes driver energy in compressive heating.

1.2 Fast Ignition

In 1994 Tabak *et al.* [9] proposed an alternative approach to ICF called fast ignition (FI). Different than CHS ignition, FI would decouple the heating and ignition processes reducing the symmetry and energy requirements [7, 9]. The capsule would be compressed with long pulse lasers, x-rays, z-pinches, etc. and then ignited with a short (1-10 ps) ultra intense laser ($\sim 10^{19}$ Wcm^{-2} [9]. The short ultra intense laser will generate particles that will deliver their energy to the compressed fuel. In the case of FI, the capsule is compressed more gradually and efficiently to form an isochoric final assembly (in contrast to the isobaric endpoint of the CHS capsule) where the fuel density is on the order of 300 gcm^{-3} and ideally uniform. Fig. 1.4 shows a comparison between the final assembled fuel configurations in CHS ignition and FI [7]. Due to the reduced peak density requirement and the more gradual nature of the implosion, FI is less sensitive to

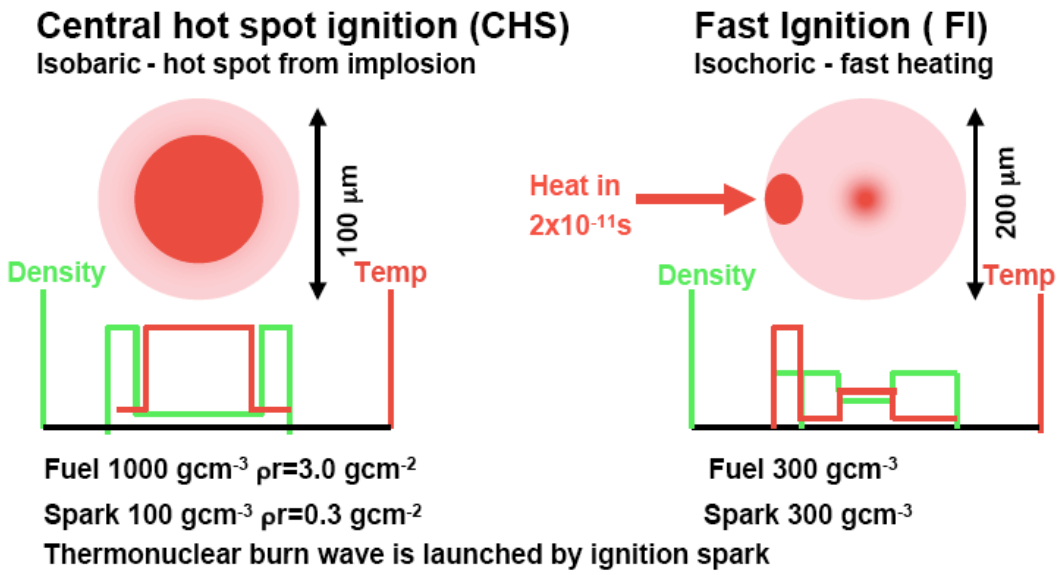

Figure 1.4: Final assembled fuel configurations for central hot spot (CHS) ignition and fast igntion(FI). In CHS, high density, cold fuel surrounds a low density, high temperature central region called the hot spot where ignition is sparked. The two regions are in pressure equilibrium. For FI, the fuel is isochorically compressed and a hot spot is created by a secondary laser that impinges the target [10].

Rayleigh-Taylor instabilities and the compression energy required from the laser or other source (e.g. z-pinch) is much reduced to be on the order of 200-300 kJ for the laser driver.

Fast ignition was initially proposed to be accomplished through hole-boring. In this approach, a hole-boring laser (with $\sim$ 100 ps pulse duration) is used to clear a path to the dense fuel by expelling coronal plasma and pushing the location of the critical surface closer to the main fuel with the ponderomotive force of the hole-boring laser in order for the ignition laser to be absorbed in a constructive way. Using a laser with an intensity of 10^{18} Wcm^{-2}, the ponderomotive pressure from the laser can push the critical surface of the coronal plasma a distance $\sim$ 1mm over 100 ps [11]. The reason being that the ignition laser energy would otherwise be absorbed a significant distance away from the dense fuel close to the position of the critical density surface (with appropriate modification for relativistic effects) [7]. At the interface of the laser and critical density, hot electrons are then produced,

some of which then heat the dense fuel to ignition temperatures (few keV).

Atzeni *et al.* [12] performed 2D radiation-hydrodynamic simulations to calculate the ignition conditions using a particle beam with uniform stopping power and range using the condition of $\rho R = 0.6$ gcm^{-2}. The energy, E_{ign}, power, W_{ign} and intensity, I_{ign} of the of the ignitor beam scales as

$$E_{ign} = 140\rho^{-1.85} \text{ kJ} \tag{1.5}$$

$$W_{ign} = 2.6 \times 10^{15}\rho^{-1} \text{ W} \tag{1.6}$$

$$I_{ign} = 2.4 \times 10^{19}\rho^{0.95} \text{ Wcm}^{-2} \tag{1.7}$$

where ρ is measured in 100 gcm^{-3}. These scalings hold for particles with a areal density range of $0.15 < \rho R < 1.2$ gcm^{-2}. With the main fuel at a density of $\rho =$ 300 gcm^{-2}, ignition is achieved with 18-20 kJ of energy delivered in a beam radius of $\leq$ 20 μm with a pulse duration of $\leq$ 20 ps, where the heated particles have a penetration depth of $\leq$ 1.2 gcm^{-2} . Delivering the needed energy within the alloted time frame is one of the major challenges of fast ignition.

This initial approach to FI has encountered a number of difficulties in its inception. Principally, the boring of a channel with a high power laser has been shown to seed the formation of numerous filamentary structures rather than a single clean channel [9, 13]. There are also problems in directing the channel toward the dense core since the rays tend to refract toward lower densities thereby missing the densest regions entirely [9, 14]. In an attempt to address these problems a new approach to FI has been envisaged. This approach is known as re-entrant cone guided fast ignition.

1.2.1 Electron cone-guided fast ignition

In the re-enterant cone guided approach, a gold cone is embedded into the side of the spherical fuel capsule. The cone allows a short pulse laser to be focused very close to the dense fuel formed by the implosion and thereby enables a useful fraction of the laser generated relativistic electrons to be absorbed in the desired location. Calculations showed that electrons should have energies of around 1-3 MeV in order to be absorbed in the most efficient manner possible from the

standpoint of ignition [7, 15]. The concept of cone guided electron FI is seen in Fig. 1.5(a).

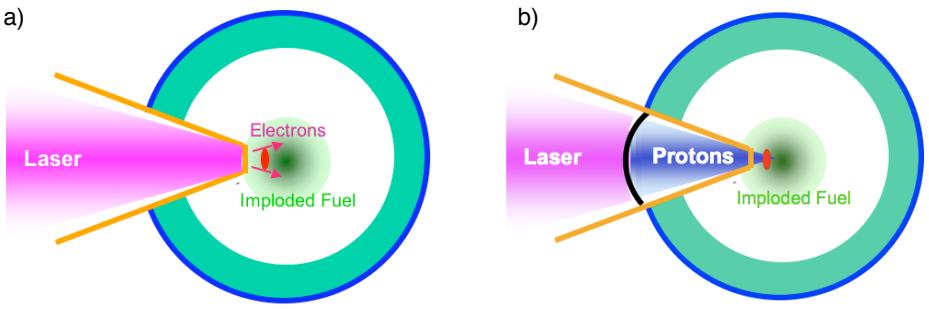

Figure 1.5: Concept of re-enterant cone guided fast ignition for (a) electron fast ignition and (b) proton fast ignition [10].

Kodama *et al.* [14] demonstrated the concept of cone guided fast ignition experimentally at the GEKKO laser facility in Japan in a substantially sub-ignition energy regime. The GEKKO laser facility provided twelve beams with nanosecond long pulses at a wavelength of 0.53 μm with a maximum energy of 15 kJ for compression and a synchronized sub-picosecond pulse delivering 60 J with a power of 100 TW for ignition. In order for the inertial energy of the core after compression was of similar magnitude to the energy available from the short pulse, the laser energy used for compression was restricted to 1.2 kJ. The laser pulsed compressed a 350 μm diameter, 6 μm thick CD shell in which a Au cone was embedded. The tip of the cone was placed 50 μm from the center of the shell to ensure that compressed plasma formed at the tip while leaving the cone intact. An increase in neutron yield of $\sim$3 orders of magnitude implied a $\sim$20% coupling between the ignitor laser and the compressed fuel.

In addition, there has been considerable difficultly in replicating the level of energy coupling inferred in the Kodama paper in experiments using other cone type targets. Recent experiments have been conducted on the OMEGA Laser Facility, including the short-pulse OMEGA EP laser, to investigate the cone-in-shell target concept for fast ignition [16]. A hollow Au cone was inserted into a $\approx$870 μm outer diameter deuterated-plastic (CD) shell with a wall thickness of 40

μm. The tip of the Au cone was placed 40 $\pm$ 10 μm away from the center of the shell with various tip thicknesses (5, 10, and 15 μm) and tip diameters (10 and 40 μm). The side wall thickness of the cone was 10 μm inside of the shell with a full inner opening angle of 34^o. The shells were at room temperature and were not filled with gas. Using the OMEGA laser as a driver, the capsule was imploded with 20 kJ of UV energy and the OMEGA EP laser delivered a short-pulse 1 kJ, 10 ps IR beam to interact with the hollow Au cone at different times with driver. Shock breakout measurements on the cone tip were performed without the short-pulse. It was determined that a thicker cone tip, 15 μm, remained intact after the capsule implosion while a 5 μm cone tip was affected by x-ray preheat from the material, which lead to premature material release inside of the cone that might affect the short-pulse laser interaction.

A fourfold increase in the neutron production was observed in the integrated shots, where the short-pulse laser was delivered within $\sim$ 100 ps of peak compression. According to simulations that were used to model the experiments. the additional production of 1.4×10^7 neutrons corresponds to a 3.5 $\pm$ 1.0% coupling efficiency of short-pulse energy into the imploded CD capsule. The 20% coupling efficiency seen in the GEKKO experiment is significantly more than the coupling efficiency seen from the recent integrated experiments. The coupling efficiency from the OMEGA experiments are based on simulations that include the hydrodynamics and the fast electron transport through the cone wall. It has been shown that the fast electron transport through the cone is sensitive to the scattering in the high-Z material, which is also affected by the resistive magnetic fields along the cone walls. In addition the formation and the amount of pre-plasma that fills the cone caused by the laser prepulse greatly affects the laser-plasma interaction and the generation of hot electrons. This then significantly lowers the amount of neutrons produced. Taking into account these physics aspects into the the simulations better predicts the coupling efficiency and can lead to an explanation regarding the difference in the conversion efficiency in the two experiments.

It is also important to consider whether this relatively high degree of coupling could be expected in a full-scale fast ignition scenario, where the compressed

fuel would be stood-off from the cone tip by a greater distance (∼100-150 μm), and the coupling of the high intensity laser to the cone may be more adversely effected by high energy prepulse (such as maybe expected for a ∼100 kJ ignitor laser) as well as other laser-plasma coupling effects which are at present and poorly understood at these energy levels and pulse durations (the ignitor pulse is expected to have a duration of ∼20 ps in full scale FI) [7, 9, 14]. Another potential problem is that in FI the energy of the relativistic electrons generated at the intensity levels required to deposit a sufficient amount of energy in the fuel in the time allow by the inertial confinement of the fuel may be too high resulting in a more diffuse energy deposition. This would result in ineffectual heating of the fuel and a failure to ignite for sensible ignitor laser energies [7].

1.2.2 Proton cone-guided fast ignition

A possible solution to this problem is proton fast ignition, which was envisioned after the observations of the generation of a quasi-neutral beam of protons from thin foils, with ∼ MeV mean energy that co-moves with the electrons [17,18]. Roth *et al.* [19] originally proposed the idea of using protons for fast ignition, which was further reviewed by Key [7]. The ignitor laser interacts with the front surface of the thin foil generating hot electrons that travel through the foil setting up a sheath field on the rear surface which ionized the present ions. Details of the proton generation, acceleration, and expansion are further discussed in detail in Chapter 2. The proton source foil is conveniently located within the cone for the re-entrant cone guided FI approach, where the cone protects the foil from the implosion of the fuel. The concept of cone guided proton FI is seen in Fig. 1.5(b). Protons have some advantages over electrons, 1) protons are less susceptible to the electromagnetic fields that are generated in the plasma, which can inhibit transport into the fuel, due to their larger mass. 2) Protons deposit the majority of their energy energy within a certain range, called the Bragg Peak. In addition, proton focusing has already been demonstrated experimentally [2, 20].

Protons tend to deposit their energy at a specific depth, called the Bragg Peak [21], in the dense fuel resulting in the formation of a compact hot spot,

which is ideal from the point of view of ignition efficiency [7, 11, 15, 19]. However, the generated proton beam is not monoenergetic resulting in the beam having a velocity dispersion. The first protons accelerated from the source foil will reach higher velocities, therefore having higher energy, and reach the compressed fuel first. The protons will deposit their energy in the plasma, heating the plasma to thermonuclear temperatures. Protons accelerated later in time from the source foil will see an increased plasma temperature, which increases the range that the proton can travel. Fig. 1.6 displays the proton range of different proton energies as a function of plasma temperature based on a plasma density of $\rho = 400$ gcm^{-3} [22]. Therefore, there is a range of proton energies, 3-15 MeV, that can be used to achieve ignition.

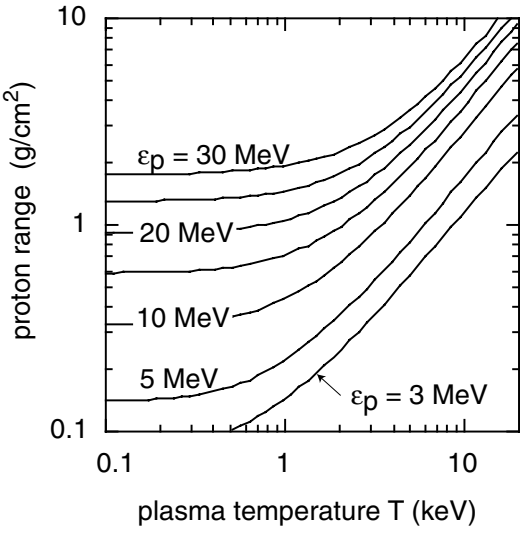

Figure 1.6: Proton range with different initial proton energy, ε_p, as a function of the temperature of the DT fuel. The plasma density is at $\rho = 400$ gcm^{-3}. Figure taken from Atzeni, Temporal, and Honrubia, Nuclear Fusion (2002) [22].

Atzeni *et al.* [22] performed 2D simulations to calculate the minimum total proton energy required to ignite the homogeneous DT fuel with a cylindrical proton beam with an average energy of T_p. The optimal value of the pulse duration t_p and proton beam focal spot radius r_b are

$$t_p = 54\ \rho^{-0.85}\ \text{ps} \tag{1.8}$$

$$r_b = 60\ \rho^{-0.97}\ \mu\text{m} \tag{1.9}$$

where ρ is in units of 100 gcm^{-3}. With a fuel density of $\rho = 400$ gcm^{-3}, the proton beam focal spot calculated from (1.9) is $r_b = 15\ \mu$m. Using these parameters, the required ignition energy, E^*_{ig}, is determined from the simulations, which is larger than that given by (1.5) since the proton energy is not constant, as assumed in the calculation of eq. (1.5). The simulations take into account the effects of the proton energy distribution, plasma hydrodynamics and proton-fuel interaction. The determined E^*_{ig} from the simulations is plotted against the average proton energy in Fig. 1.7 for three different distances from the source foil to the fuel. The

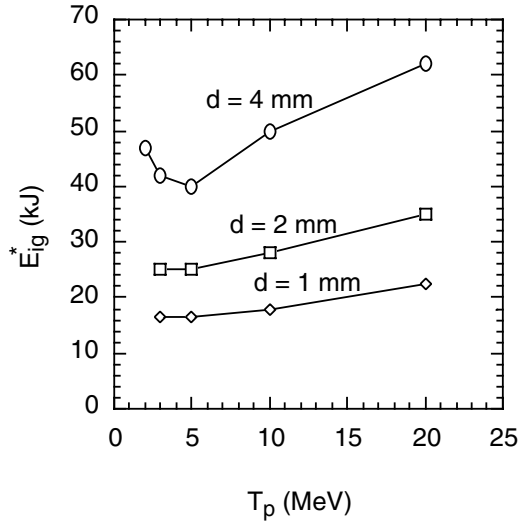

Figure 1.7: Ignition energy required for fast ignition as a function of the average proton energy T_p for protons with a exponential energy distribution. The lines correspond to the different distances, d, from the source foil to the compressed DT fuel. The compressed DT had a density of $\rho = 400$ gcm^{-3} with the proton beam having a radius of $r_b = 15\ \mu$m. Figure taken from Atzeni, Temporal, and Honrubia, Nuclear Fusion (2002) [22].

average proton energy ranges from 3 to 20 MeV at the distances (d) of 1, 2, and 4 mm. For $T_p = 5$ MeV, the simulation results are fitted by

$$E^*_{ig} \simeq 90\ d^{0.7}_{mm}/\rho^{1.3}\ \text{kJ}, \tag{1.10}$$

where ρ is in units of 100 gcm^{-3}. With the source foil 1 mm away from the compressed fuel at a density of $\rho = 400$ gcm^{-3}, using eq. (1.10), the proton beam needs

to deliver 15 kJ of energy in a 30 μm diameter focal spot, which was calculated by eq. (1.9). For a fuel density of $\rho = 300$ gcm^{-3}, which was used in the calculations for electron fast ignition, the proton beam would then need to deliver 21 kJ of energy in a 40 μm diameter focal spot. Assuming a laser to proton conversion efficiency of 15%, this would require an ultra-intense driver laser to deliver 140 kJ to the source foil. Therefore, the requirements of the laser to proton conversion efficiency of 15% and the focusing of the proton beam to a 40 μm diameter spot are the two challenges for proton fast ignition and will be the topic of this thesis.

1.3 Outline of the Dissertation

Chapter 2 provides an introduction and a theoretical description of laser plasma interaction and different laser absorption mechanisms that are pertinent to inertial confinement fusion. Proton acceleration is discussed in detail for the application of proton fast ignition. An overview of the previous studies conducted on the characteristics of protons beams is presented along with a discussion of the other applications where proton beams are used.

Chapter 3 presents a description of the Trident laser system at Los Alamos National Laboratory where the experiments were conducted and the main diagnostic used is the experiments: radiochromic film. A three-dimensional ray-tracing technique is presented to calculate the focal position and focal spot size of a generated proton beam. The method of obtaining the laser to proton conversion efficiency from the radiochromic film is also described. A description of the simulation code LSP (large-scale-plasma) is provided, which is used to further explore the experimental results.

Chapter 4 gives the details of the experimental set-up, and presents our results from flat foil targets. Results for proton conversion efficiency and focusing (i.e. position and spot size) of the proton beam generated from flat foils are presented. A proton beam generated from a flat foil is calculated using the ray-tracing technique to have a real focus instead of the a virtual focus. The proton beam expansion physics affects the proton trajectories as they are accelerated from

the foil, leading to the notion of a real focus. The expansion physics are discussed with the aid of LSP simulations. The effects on the focusing and proton conversion efficiency from the technique used to mount the foils are also presented

Chapter 5 gives the details of the experimental set-up and results from hemispherical shell targets. It is shown that the protons accelerated from a hemispherical target do not move in straight line trajectories as previously thought, but bend near the focal region. The physics of the bending of the proton trajectories is illustrated through the use of simulations. The LSP results show an electric field within the quasi-neutral proton beam that bends the proton trajectories near the focal position. Focusing results are also presented for hemispherical shell targets placed inside of a surrounding structure, which is required for the design of proton FI. The results show the surrounding structure affecting the focus of the proton beam and decreasing the proton conversion efficiency. LSP further illustrates the development of an electric field on the walls of the surrounding structure which influences the trajectories of the protons which are close to the wall.

Chapter 6 provides a summary of the experimental and simulation results and presents the conclusions from the data. A discussion regarding future work and experiments that can be conducted is presented to further explore the findings presented in this thesis.

1.4 Role of the Author

The role of the Author in the work that is presented in this thesis is described in this section. The experimental data discussed in Chapters 4 and 5 was collected during two experimental campaigns that took place at Los Alamos National Laboratory on the Trident laser system in May of 2009 and in February of 2010. The experimental campaign in May of 2009 by designed by F. N. Beg and M. S. Wei. The author was involved in the diagnostic and target set-up, conducting the experimental campaign and analyzing the data. For the February 2010 campaign, the Author designed the experiment, was the principal investigator during the campaign and analyzing the data. The ray-tracing technique, presented in

Chapter 3, which was used to analyzed the data, was developed by the Author. The calibration of the radiochromic film presented in Chapter 3 at Crocker Nuclear Laboratory at the University of California, Davis was done with D. T. Offermann. Simulations that are presented in Chapters 5 and 4 were performed by M. E. Foord, C. Bellei, and B. Qiao.

Chapter 2

Background and Theory

In order for fast ignition to be successful, a clear understanding of the laser plasma interaction, electron transport (electron fast ignition) and proton production, focusing and conversion efficiency (proton fast ignition) is required. When high power lasers are focused onto matter, extremely rapid ionization occurs on the interaction surface. The ionization creates a significant number of free electrons (referred to as hot electrons) that form a dense, highly ionized plasma. The plasma formed can therefore interact with the remainder of the laser pulse. Particle motion and various laser absorption mechanisms are presented in this chapter to understand the generation of hot electrons. The generated hot electrons will transverse the target, forming a hot electron cloud on the rear surface, leading to a strong sheath field that accelerates protons from the rear surface of the target, which are needed for proton fast ignition. The expansion of plasma is examined through a one-dimensional expansion model into vacuum. Since the observation of laser-produced proton beams [17, 18, 23], several studies have been carried out to understand the characteristics of the generated proton beam [1, 24–32]. Results of these past experiments provided the groundwork for the experimental studies that are presented in the subsequent chapters of this thesis.

2.1 Laser-Plasma Interaction

When the laser, an electromagnetic (EM) wave, interacts with a solid target, rapid ionization occurs creating free electrons which form a dense, highly ionized plasma on the front surface of the target. The EM wave travels in vacuum until it interacts with the plasma where the propagation of the wave is modified. Basic particle motion is first reviewed in this section and then is applied to the interaction of the wave with the plasma. The laser plasma interaction is further explored by discussing single electron interaction, the ponderomotive force, laser propagation and laser absorption mechanisms. The derivation and information in the following sections come from Refs. [33–36] and references within those.

2.1.1 Single electron interaction with intense electromagnetic fields

The motion of an electron in an electromagnetic (EM) wave obeys the following equation [33]

$$m\frac{d\mathbf{v}}{dt} = q(\mathbf{E} + \mathbf{v} \times \mathbf{B}) \tag{2.1}$$

where m is the particle mass, $q\mathbf{E}$ is the electric force and $q(\mathbf{v} \times \mathbf{B})$ is the magnetic force. The magnetic force causes the particle to have a circular orbit around a guiding center and the electric field causes a drift in the guiding center. In three dimensions, the trajectory of the particle is a slanted helix with changing pitch. An electron traveling in the field of an EM wave will oscillate transversely along the direction of the electric field at the frequency of the field. The motion is confined to the x-z plane, where x is the propagation axis and z is the direction of the $\mathbf{E}$ field. The velocity at which the electron oscillates is so-called the electron quiver velocity [35, 36].

$$v_{osc} = \frac{e\mathbf{E}_L}{m_e\omega_L} \tag{2.2}$$

where $\mathbf{E}_L$ is the electric field amplitude of the laser field, m_e is the electron mass, and ω_L is the laser frequency. The ratio of the electron quiver velocity over the

speed of light, c, is referred to as the normalized vector potential [34–36].

$$a_0 = \frac{v_{osc}}{c} = \sqrt{\frac{I\lambda_L^2}{1.37 \times 10^{18}}} \tag{2.3}$$

where λ_L is the wavelength of the laser in units of μm and I is the laser intensity in units of Wcm^{-2}. When $a_0 \ll 1$, the motion of the electron is non-relativistic and can be treated classically. When $a_0 \sim 1$, the electron motion becomes relativistic, where the magnetic field of the laser becomes important because $\frac{\mathbf{v}\times\mathbf{B}}{c} \sim E$, which accounts for the longitudinal component of the electron motion. To take into account the relativistic effect, the electron motion should be expressed as

$$\frac{d\mathbf{p}}{dt} = q(\mathbf{E} + \mathbf{v} \times \mathbf{B}) \tag{2.4}$$

where $\mathbf{p} = \gamma m_e \mathbf{v}$ and γ is the relativistic factor represented by [35]

$$\gamma = \sqrt{1 + \frac{p^2}{m_e^2 c^2}} = \sqrt{1 + \frac{v^2}{c^2}} = \sqrt{1 + a_0^2}. \tag{2.5}$$

When an electron is traveling in the EM wave, the fields in the equation of motion are externally applied. However, the fields in plasma are not prescribed but are a result of the movement of the particles in the plasma, which is time variant [33]. Since a plasma has a large number of particles, the electrons in the plasma move together and can be treated as a fluid. The complete description of the behavior a of collisionless plasma is provided by the Vlasov equation:

$$\frac{\partial f_i}{\partial t} + \mathbf{v} \cdot \frac{\partial f_i}{\partial t} + \frac{q_i}{m_i}\left(\mathbf{E} + \frac{\mathbf{v} \times \mathbf{B}}{c}\right) \cdot \frac{\partial f_i}{\partial \mathbf{v}} = 0. \tag{2.6}$$

The Vlasov equation characterizes the location of particles of species i in phase space as a function of time with the particles having a phase space distribution function of $f_i(\mathbf{x},\mathbf{v},t)$. Equations to describe the temporal and spatial evolution of the density, mean velocity, and pressure for each species are derived by taking different velocity moments of the Vlasov equation. Taking the second velocity moment of the Vlasov equation results in the equation of motion for a charged fluid (plasma) for each species i:

$$mn\left(\frac{\partial \mathbf{v}}{\partial t} + (\mathbf{v} \cdot \nabla)\mathbf{v}\right) = qn(\mathbf{E} + \mathbf{v} \times \mathbf{B}) - \nabla \mathbf{p}. \tag{2.7}$$

where $\nabla \mathbf{p}$ is the pressure-gradient force term that takes into account the thermal motion of the particles moving in the plasma.

2.1.2 Ponderomotive Force

Variations in the electric field pressure are generated when an excited plasma wave beats with the laser light wave. The gradient of the electric field pressure is called the ponderomotive force. The ponderomotive force pushes an oscillating particle near the center of the focused laser beam toward the area of weaker field [34, 35]. For the nonrelativistic case, neglecting the electron pressure, the equation of motion for an electromagnetic wave without an external magnetic field is [35]

$$\left(\frac{\partial \mathbf{v}}{\partial t} + (\mathbf{v}\cdot\nabla)\mathbf{v}\right) = -\frac{e}{m_e}\mathbf{E}. \tag{2.8}$$

If the variation in the electric field is small, the motion of the particle can be divided into the slow and fast components where the slow component represents the slow drift motion while the fast component represents the fast oscillation of the electrons. Therefore, $\mathbf{r} = \mathbf{r}_1 + \mathbf{r}_2$. Assuming that $\mathbf{r}_2 \ll \mathbf{r}_1$, a Taylor expansion can be done on the equation of motion around the initial position of the electron, $\mathbf{r}_0$. A Taylor expansion of the electric field gives

$$\mathbf{E}(\mathbf{r}) = \mathbf{E}_0(\mathbf{r}_0) + (\mathbf{r}_1\cdot\nabla)\mathbf{E}|_{\mathbf{r}=\mathbf{r}_0} + \ldots \tag{2.9}$$

For a field oscillating at the frequency ω, the electric field is expressed as

$$\mathbf{E}(\mathbf{r}) = \mathbf{E}_0(\mathbf{r}_0)\cos(\omega t) \tag{2.10}$$

where $\mathbf{E}_0$ is the amplitude of the laser electric field. Taking the lowest order terms, the equation of motion becomes

$$\frac{\partial \mathbf{v}_1}{\partial t} = -\frac{e}{m_e}\mathbf{E}_0(\mathbf{r}_0)\cos(\omega t). \tag{2.11}$$

Integrating the equation of motion yields the velocity of the electron given by

$$\mathbf{v}_1 = -\frac{e}{m_e\omega}\mathbf{E}_0(\mathbf{r}_0)\sin(\omega t), \tag{2.12}$$

which is the electron quiver velocity, v_{osc}, given in eq. 2.2. Integrating a second time yields the position of the electron given by

$$\mathbf{r}_1 = -\frac{e}{m_e\omega^2}\mathbf{E}_0(\mathbf{r}_0)\cos(\omega t) \tag{2.13}$$

Taking the second order terms of the Taylor expansion, the equation of motion becomes

$$\frac{\partial \mathbf{v}_2}{\partial t} = -\frac{e}{m_e}\left[(\mathbf{r}_1 \cdot \nabla)\,\mathbf{E}|_{\mathbf{r}=\mathbf{r}_0} + \mathbf{v}_1 \times \mathbf{B}_1\right]. \tag{2.14}$$

Using Maxwell's equation $\nabla \times \mathbf{E} = -\partial \mathbf{B}/\partial t$ the magnetic field is represented by

$$\mathbf{B}_1 = -\frac{1}{\omega}\left(\nabla \times \mathbf{E}_0 \sin(\omega t)\right). \tag{2.15}$$

Substituting (2.15) into the equation of motion and taking the time average of the oscillations in the laser field, the resulting force is called the ponderomotive force expressed by

$$\mathbf{F}_{pond} = m_e \left\langle \frac{\partial \mathbf{v}_2}{\partial t} \right\rangle = -\frac{e^2}{4 m_e \omega^2} \nabla \mathbf{E}_0^2, \tag{2.16}$$

which is proportional to the gradient of the electric field pressure. An electron near the center of the laser beam will then drift away from regions of higher intensity.

However, when the laser intensity increases and the electron motion becomes relativistic, the magnetic field is significant and gives the electron a longitudinal velocity component. For the relativistic case, the equation of motion is [35–37]

$$\frac{\partial \mathbf{p}}{\partial t} + (\mathbf{v} \cdot \nabla)\,\mathbf{p} = -e\left[\mathbf{E} + \frac{1}{c}\mathbf{v} \times \mathbf{B}\right]. \tag{2.17}$$

To obtain similar terms, use the vector potentials for the fields given by $\mathbf{E} = -c^{-1}\partial \mathbf{A}/\partial t - \nabla \phi$ and $\mathbf{B} = \nabla \times \mathbf{A}$ and replace the velocity, by $\mathbf{v} = \mathbf{p}/\gamma m$ to obtain

$$\frac{\partial \mathbf{p}}{\partial t} + \frac{(\mathbf{p} \cdot \nabla)\,\mathbf{p}}{\gamma m} = -e\left[-\frac{1}{c}\frac{\partial \mathbf{A}}{\partial t} - \nabla \phi + \frac{\mathbf{p} \times \nabla \times \mathbf{A}}{\gamma m c}\right]. \tag{2.18}$$

If the EM wave is a 1D plane wave moving in the longitudinal direction, the particle momentum can be separated into the transverse and longitudinal components, $\mathbf{p} = \mathbf{p}_T + \mathbf{p}_L$. The vector potential of the wave oscillates in the longitudinal direction, but only has a transverse component. The transverse component of the equation of motion is

$$\frac{\partial \mathbf{p}}{\partial t} + \frac{(\mathbf{p} \cdot \nabla)\,\mathbf{p}}{\gamma m} = -e\left[-\frac{1}{c}\frac{\partial \mathbf{A}}{\partial t} + \frac{\mathbf{p} \times \nabla \times \mathbf{A}}{\gamma m c}\right]. \tag{2.19}$$

Using the vector identity $\mathbf{A} \times (\nabla \times \mathbf{B}) = \nabla \mathbf{B} \cdot \mathbf{A} - (\mathbf{A} \cdot \nabla)\,\mathbf{B}$, where only the components with $\mathbf{A}_x$, $\mathbf{A}_y$, and d/dz survive, the equation of motion for the transverse

component becomes

$$\frac{\partial}{\partial t}\left(\mathbf{p}_T - \frac{e}{c}\mathbf{A}\right) = -\frac{\mathbf{p}_z}{\gamma m}\frac{\partial}{\partial z}\left(\mathbf{p}_T - \frac{e}{c}\mathbf{A}\right), \tag{2.20}$$

where $\mathbf{p}_z = \mathbf{p}_L$. Therefore the transverse momentum is

$$\mathbf{p}_T = \frac{e}{c}\mathbf{A}. \tag{2.21}$$

The longitudinal component of the equation of motion is then

$$\frac{\partial \mathbf{p}}{\partial t} + \frac{(\mathbf{p}\cdot\nabla)\,\mathbf{p}}{\gamma m} = -e\left[-\nabla\phi + \frac{\mathbf{p}\times\nabla\times\mathbf{A}}{\gamma m c}\right]. \tag{2.22}$$

The vector potential can be replaced by the momentum by taking the curl of the transverse momentum because the curl of (2.21) is equal to zero. The longitudinal component of the equation of motion can then be written as

$$\frac{\partial \mathbf{p}}{\partial t} + \frac{(\mathbf{p}\cdot\nabla)\,\mathbf{p}}{m\sqrt{1+\frac{\mathbf{p}^2}{m^2c^2}}} = -e\left[-\nabla\phi + \frac{\mathbf{p}\times\nabla\times\mathbf{p}}{mc\sqrt{1+\frac{\mathbf{p}^2}{m^2c^2}}}\right]. \tag{2.23}$$

where $\gamma = \sqrt{1+p^2/m^2c^2}$ [35] was substituted into the denominator. To simplify the equation, a variable $\mathbf{A}$ can be defined as $\mathbf{A} = \mathbf{p}/mc$ making the equation become

$$\frac{\partial \mathbf{p}}{\partial t} = e\nabla\phi - mc^2\left[\frac{\mathbf{A}\times\nabla\times\mathbf{A}}{\sqrt{1+\mathbf{A}^2}} + \frac{(\mathbf{A}\cdot\nabla)\,\mathbf{A}}{\sqrt{1+\mathbf{A}^2}}\right]. \tag{2.24}$$

Using the following vector identity

$$\nabla(\mathcal{A}\cdot\mathcal{B}) = \mathcal{A}\times(\nabla\times\mathcal{B}) + \mathcal{B}\times(\nabla\times\mathcal{A}) + (\mathcal{A}\cdot\nabla)\,\mathcal{B} + (\mathcal{B}\cdot\nabla)\,\mathcal{A}, \tag{2.25}$$

where $\mathcal{A} = \mathcal{B}$, the portion in the brackets in eq. (2.24) becomes

$$\frac{\mathbf{A}\times\nabla\times\mathbf{A}}{\sqrt{1+\mathbf{A}^2}} + \frac{(\mathbf{A}\cdot\nabla)\,\mathbf{A}}{\sqrt{1+\mathbf{A}^2}} = \nabla\sqrt{1+\mathbf{A}^2} = \nabla\gamma. \tag{2.26}$$

Therefore, the longitudinal component of the electron fluid momentum is [35, 36]

$$\frac{\partial \mathbf{p}_L}{\partial t} = e\nabla\phi - mc^2\nabla(\gamma-1), \tag{2.27}$$

which $\nabla\gamma = \nabla\gamma - \nabla(1) = \nabla(\gamma-1)$ is added because the rest energy is 1 and $\nabla(1) = 0$. The first term in the longitudinal component is the electrostatic force

felt by the electron. The second term in the relativistic ponderomotive force, which is the gradient of the ponderomotive potential. The ponderomotive potential is

$$U_p = mc^2(\gamma - 1). \tag{2.28}$$

Numerically, the relativistic ponderomotive potential is given by

$$U_p = mc^2 \left(\sqrt{1 + \frac{I\lambda^2}{1.37 \times 10^{18}}} - 1 \right). \tag{2.29}$$

The ponderomotive potential can be thought of as the effective temperature of the hot electrons that are accelerated by the laser. The energy of the hot electrons is associated with the potential they feel during the laser interaction. Therefore, the hot electron temperature from the ponderomotive scaling is given by [36]

$$T_{ehot} \approx 0.511\ MeV \left(\sqrt{1 + \frac{I\lambda^2}{1.37 \times 10^{18}}} - 1 \right), \tag{2.30}$$

which has been demonstrated experimentally and by simulations [36, 38]. For the experiments presented in the results chapter, with a laser intensity of $\sim 2 \times 10^{18}$ Wcm^{-2} and wavelength of ~ 1 μm, results in $T_{ehot} \approx 290$ keV.

2.1.3 Laser propagation in plasma

The propagation of the laser is modified by the movement of the free electrons in the plasma on the target surface due to the rapid ionization of the material from the laser interaction. The fluid description of plasma is used to describe the laser propagation into the plasma and the plasma characteristics. The periodic motion of the plasma can be described as a sinusoidally oscillating wave. The real components of the electric and magnetic fields are represented by

$$\mathbf{E}(\mathbf{r}, t) = E_0 \cos(\mathbf{k} \cdot \mathbf{r} - \omega t) \tag{2.31}$$

and

$$\mathbf{B}(\mathbf{r}, t) = B_0 \cos(\mathbf{k} \cdot \mathbf{r} - \omega t) \tag{2.32}$$

where $\mathbf{k}$ is the wave vector and $\mathbf{r}$ is the position vector. From the first order-linearized equation of motion, the characteristic plasma frequency is calculated.

The plasma frequency is described as the frequency of which an electron oscillates around its equilibrium when it is displaced from a uniform background. The plasma frequency is

$$\omega_p^2 = \frac{4\pi e^2 n_e}{m_e}, \tag{2.33}$$

which is a function of the electron density n_e.

For a laser light wave traveling at the speed of light before propagating into an underdense plasma with a frequency of ω_p and no initial magnetic field, the dispersion relation is [33]

$$\omega_L^2 = \omega_p^2 + c^2 k_L^2, \tag{2.34}$$

where ω_L is the laser frequency and k_L is the laser wavenumber.

As the laser propagates deeper into the plasma, the plasma density increases, which leads to the increase of ω_p and decrease of k. At a point during the propagation, a density will be reached where k becomes zero and the wave can no longer propagate. This density is defined as the critical density given by [33, 39]

$$n_c \equiv \frac{m_e \omega_L^2}{4\pi e^2}. \tag{2.35}$$

As a function of the laser wavelength, λ_L , the critical density becomes

$$n_c = 1.1 \times 10^{21} \left(\frac{1\ \mu\text{m}}{\lambda_L} \right)^2 \text{cm}^{-3} \tag{2.36}$$

When the interaction becomes relativistic, the critical density is increased by factor of γ; therefore, $n_{\gamma c} = \gamma n_c$. For the experiments presented in the results chapter, with a laser intensity of $\sim 2{\times}10^{18}$ Wcm^{-2} and wavelength of $\sim$1 μm, the relativistic critical density is approximately $n_{\gamma c} \sim 1.73{\times}10^{21}$cm^{-3}. Above this density, the value of k_L is imaginary

$$c^2 k_L^2 = i \left| \omega_p^2 - \omega_L^2 \right| \tag{2.37}$$

and the laser light wave becomes evanescent. The wave will be exponentially attenuated, due to its spatial dependence, penetrating into the overdense region a distance known as the skin depth represented by [39]

$$\delta = \frac{1}{|k_L|} = \frac{c}{\sqrt{\omega_p^2 - \omega_L^2}}. \tag{2.38}$$

2.1.4 Laser Absorption Mechanisms

The temperature, density and velocity profiles of the preformed plasma on the target will determine which mechanism will be responsible for the absorption of the laser energy into the target. The absorbed laser energy is responsible for the generation and acceleration of the hot electrons. The generation and characterization of the hot electrons is still a hot topic of research because of its applications, in particular to electron fast ignition [7]. The hot electrons that are accelerated and traverse through the target are responsible for the acceleration of the protons from the target. The four commonly discussed laser absorption mechanisms, which will be discussed here, are: inverse bremsstrahlung, resonance absorption, vacuum heating, and $\mathbf{J} \times \mathbf{B}$ heating.

2.1.4.1 Inverse Bremsstrahlung

Inverse bremsstrahlung, which is also referred to as collisional absorption, is due to electron-ion collisions in the plasma. Electrons that are oscillating in the electric field of the laser light wave can collide with ions present in the plasma causing the momentum of the electrons to change and damp the energy of the laser wave. In return, the plasma heats up. This mechanism has the greatest effect for low temperature, high density and high Z plasmas with intensities below 10^{15} Wcm^{-2} [35, 39].

The binary collisions result in a frictional drag on the electron motion. This frictional drag is taken into account in the equation of motion by including a collision damping term. The equation of motion becomes [35]

$$m\frac{\partial \mathbf{v}}{\partial \mathbf{t}} = -e\left(\mathbf{E} + \mathbf{v} \times \mathbf{B}\right) - m\nu_{ei}\mathbf{v} \tag{2.39}$$

The variable ν_{ei} is the electron-ion collision frequency given by

$$\nu_{ei} = \frac{4}{3}(2\pi)^{1/2}\frac{n_e Z e^4}{m_e^2 v^3}\ln\Lambda \backsimeq 2.91 \times 10^{-6} Z n_e T_e \ln\Lambda \mathrm{s}^{-1} \tag{2.40}$$

where n_e is the electron density in cm^{-3}, T_e is the electron temperature (eV), Z is the number of free electrons and $\ln\Lambda$ is the Coulomb logarithm.

The effect of the collisional damping term on the propagation of the wave in the plasma is understood by analyzing the EM wave equation using Maxwell's equations:

$$\nabla \times \mathbf{E} = -\frac{1}{c}\frac{\partial \mathbf{B}}{\partial t} \tag{2.41}$$

$$\nabla \times \mathbf{B} = \frac{4\pi}{c}\mathbf{J} + \frac{1}{c}\frac{\partial \mathbf{E}}{\partial t} \tag{2.42}$$

where $\mathbf{J}$ is the current density given by $\mathbf{J} = ne\mathbf{v}$. Taking the curl of eq. (2.41) and eq. (2.42) and using the vector indentity $\nabla \times \nabla \times \mathcal{A} = \nabla(\nabla \cdot \mathcal{A}) - (\nabla \cdot \nabla)\mathcal{A}$ results in

$$\nabla^2 \mathbf{E} - \frac{1}{c^2}\frac{\partial^2 \mathbf{E}}{\partial t^2} = \frac{4\pi}{c}\frac{\partial \mathbf{J}}{\partial t} + \nabla(\nabla \cdot \mathbf{E}) \tag{2.43}$$

$$\nabla^2 \mathbf{B} - \frac{1}{c^2}\frac{\partial^2 \mathbf{B}}{\partial t^2} = \frac{4\pi}{c}\nabla \times \mathbf{J}. \tag{2.44}$$

The source terms for the EM wave in the plasma are on the right hand side of the equations. The collision damping term in the equation of motion can be related to the current density in the wave equation through the electron velocity. Assuming that the fields can be described as an oscillating plane wave in 1D with the motion expressed by $exp[i(kx - \omega t)]$, the wave equations and the equation of motion can be simplified by using the following approximations: $\partial/\partial t \rightarrow -i\omega$, $\nabla \rightarrow i\mathbf{k}$, $n_e \rightarrow n_0 + n_1$, $\mathbf{J} \rightarrow -en_0\mathbf{v}_1$, and $(\mathbf{E} + \mathbf{v} \times \mathbf{B}) \rightarrow \mathbf{E}_1$. Substituting the approximations into the equation of motion and solving for the electron velocity results in

$$\mathbf{v}_1 = \frac{-1}{\omega + i\nu_{ei}}\frac{e\mathbf{E}_1}{m}. \tag{2.45}$$

Therefore the current density is

$$\mathbf{J} = -en_0\mathbf{v}_1 = \frac{i}{\omega + i\nu_{ei}}\frac{e^2 n_0 \mathbf{E}_1}{m} = \frac{i}{\omega + i\nu_{ei}}\frac{\omega_p^2}{4\pi}\mathbf{E}_1 = \sigma_e \mathbf{E}_1 \tag{2.46}$$

where σ_e is the electrical conductivity of the plasma . The value of the current density can be substituted back into the wave equation. Using the above assumptions, eq. (2.41) becomes

$$\left(-k^2 + \frac{\omega^2}{c^2} - \frac{\omega_p^2}{c^2}\frac{1}{\left(1 - \frac{\nu_{ei}}{\omega}\right)}\right)\mathbf{E}_1 = 0 \tag{2.47}$$

The dispersion relation for the laser light wave interacting with the plasma is given by setting the value in the brackets equal to zero. Damping of the wave occurs when the wavenumber, k, becomes imaginary.

In the case where the electron-ion frequency is much less than the laser frequency $\nu_{ei} \ll \omega_L$, the dispersion relation can be expanded resulting in [39]

$$\frac{k_L^2 c^2}{\omega_L^2} \approxeq 1 - \frac{\omega_p^2}{\omega_L^2} + \left(\frac{i\nu_{ei}}{\omega_L}\right)\left(\frac{\omega_p^2}{\omega_L^2}\right). \tag{2.48}$$

Therefore, when the laser wave is propagating through the plasma, the amount that the wave damps from the electron-ion collisions is represented by the imaginary part of the wavenumber. Solving the above equation for k gives

$$k \approxeq \pm\frac{\omega_L}{c}\sqrt{1 - \frac{\omega_p^2}{\omega_L^2}}\left[1 + i\frac{\nu_{ei}}{2\omega_L}\frac{\omega_p^2}{\omega_L^2}\frac{1}{1 - \frac{\omega_p^2}{\omega_L^2}}\right]. \tag{2.49}$$

The damping rate is twice the imaginary part given by

$$\kappa_{IB} \approxeq \frac{\nu_{ei}}{c}\frac{\omega_p^2}{\omega_L^2}\frac{1}{\sqrt{1 - \frac{\omega_p^2}{\omega_L^2}}}, \tag{2.50}$$

which can be estimated as [36, 39]

$$\kappa_{IB} \propto \frac{Z n_e^2}{T_e^{1/2}\sqrt{1 - n_e/n_c}} \tag{2.51}$$

inverse bremsstrahlung is the strongest for high Z-materials, high densities, low temperatures, and long plasma lengths due to the dependence on the electron-ion collision frequency and the electron density and temperature (by the means plasma frequency) . Because of its dependence on the ratio of n_e/n_c, the majority of the absorption from inverse bremsstrahlung comes from the region near n_c.

The amount of absorption that occurs depends on the distribution of the thermal ions that collide with the electrons in the laser wave. Johnston and Dawson [40] calculated the absorption coefficient for a thermal distribution of ions and a Maxwellian electron distribution in a homogeneous plasma resulting in

$$\kappa = \sqrt{2\pi}\frac{16\pi}{3}\frac{Z n_e^2 e^6 \ln\Lambda}{c\left(m_e T_e\right)^{3/2}\omega_L^2\sqrt{1 - n_e/n_c}} \tag{2.52}$$

In an inhomogeneous plasma, the absorption is highly complicated since n_e, T_e and $\ln\Lambda$ can all depend on the position in the plasma; however, n_e is the dominant factor because T_e varies much slower than n_e and the variation in $\ln\Lambda$ is negligible. Ginsburg [41] provides a detailed description of inverse bremsstralung absorption in a linear density gradient. With the scalelength L for the linear density gradient, the absorption coefficient is given by

$$\kappa_{IB} = 1 - exp\left(-\frac{32\nu_{ei}(n_c)}{15c}L\right) \tag{2.53}$$

where $\nu_{ei}(n_c)$ is the collision frequency evaluated at the critical density.

For high laser intensities present today, there are two nonlinear effects that can decrease the inverse Bremsstralung. First, the thermal velocity of the electrons can have an effective dispersion that is caused by the coherent oscillatory motion of the electrons in the laser field. This in turn will affect the Coulomb collision frequency and decrease the absorption coefficient. This effect is discussed in more detail in Ref. [42–44].

Langdon [45] explains the second nonlinear effect, which involves the electron distribution. When the laser intensity is high, electrons gain energy from the laser faster than the equilibration time, resulting in an electron distribution which is far from Maxwellian. The electrons mainly responsible for inverse bremsstralung are slow compared to the thermal velocity of the electrons; therefore, this effect decreases the amount of inverse bremsstralung absorption.

2.1.4.2 Resonance Absorption

Resonance absorption is a collisionless absorption mechanism that occurs when a laser light wave is incident on a plasma at an oblique angle [34–36]. The laser light wave must be p-polarized meaning that the longitudinal component of the electric field is along the same direction as the density gradient in the plasma (i.e. $\mathbf{E}\cdot\nabla n_e \neq 0$). For s-polarization, $\mathbf{E}\cdot\nabla n_e = 0$, and no electrostatic waves can be driven. Interacting with the plasma at an oblique angle, the laser light wave will propagate until it reaches the density of $n = n_c\cos^2\theta$, given by Snell's law, instead of the critical density, where θ is the angle measured with respect to

the target normal. At this position, part of the wave will be specularly reflected and the longitudinal component of the electric field will become evanescent and be damped exponentially. Since the distance from the reflection point to the critical density is small, the decaying electric field will tunnel to the critical density. A cartoon illustrating the process of resonance absorption is displayed in Fig. 2.1.

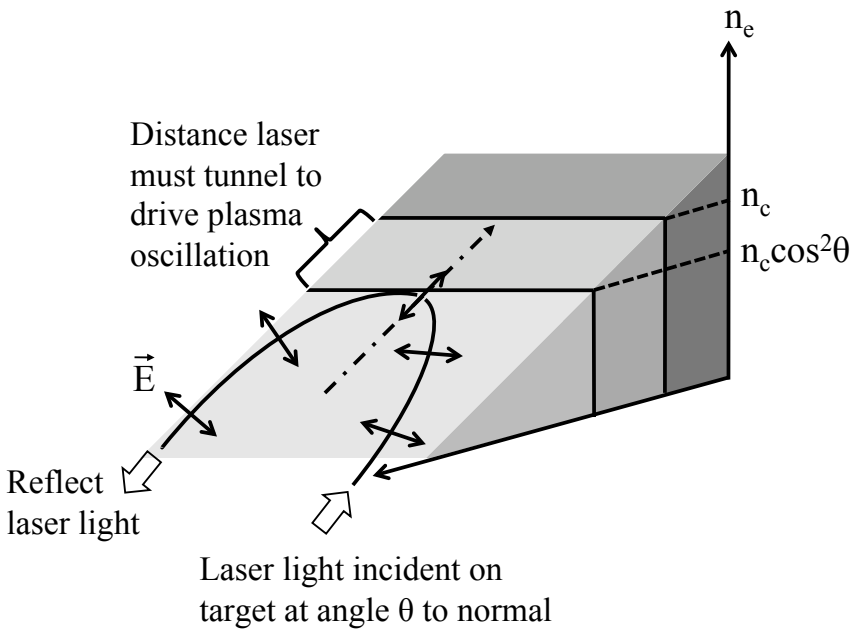

Figure 2.1: Schematic of resonance absorption where the electric field of the p-polarized laser light is along the same direction as the plasma density gradient.

The tunnelling wave will be resonantly excited at the laser frequency, oscillating electrons along the direction of the density gradient, which causes fluctuations in the plasma charge density. The fluctuations in the charge density gives rise to an associated electrostatic field that is capable of accelerating electrons in the plasma. The electrostatic field is given by [36]

$$\mathbf{E}_s = \epsilon(z)\frac{\mathbf{E}_L}{\sqrt{2\pi\omega_L L_n/c}}\phi(\tau), \tag{2.54}$$

where L_n is the density scale length and $\epsilon(z)$ is the plasma dielectric function. The function $\phi(\tau)$ describes the strength of the excitation of the wave given by

$$\phi(\tau) \cong 2.3\tau exp\left(\frac{-2\tau^3}{3}\right), \tag{2.55}$$

where τ is a parameter that relates the density scale length to the angle of incidence

$$\tau = \left(\frac{\omega_L L_n}{c}\right) \sin\theta. \tag{2.56}$$

When the rate of damping the EM wave experiences is small compared to the laser frequency, the fraction of the energy transferred to the plasma due to the excitation of the electrostatic wave at critical density is given by $f \approx \phi^2(\tau)/2$. The angle of incidence affects the amount of resonant absorption that can occur. When the angle of incidence is near normal incidence, there is hardly any longitudinal component of the electric field. On the other hand, when the angle of incidence is large, the reflection point of the EM wave is a large distance away from the critical density and the electrostatic field at critical density is not efficiently excited. Therefore, there is an optimum angle of incidence for the laser light wave, which is

$$\left(\frac{\omega_L L_n}{c}\right)^{1/3} \sin\theta \approx 0.8. \tag{2.57}$$

For laser intensities greater than 10^{15} Wcm^{-2}, where resonance absorption is the main laser absorption mechanism, collisionless heating of electrons traveling from high densities to lower densities were seen in particle-in-cell simulations [39, 46]. These hot electrons are seen to have approximately a Maxwellian distribution with an average hot electron temperature that scales as [46]

$$T_h \sim 14(I\lambda^2)^{1/3} T_c^{1/3} \text{ keV}, \tag{2.58}$$

where I is the laser intensity in units of 10^{16} Wcm^{-2}, λ is the laser wavelength in units of microns, and T_c is the temperature of the background electrons at the critical density in units of keV.

2.1.4.3 Vacuum Heating

Vacuum heating or Brunel heating was first discussed by Brunel in 1987 [47]. This mechanism occurs when the density gradient on the front surface of a target is very steep, where the density scale length is smaller than the wavelength of the incident laser light [36]. Because of the steep density gradient scale length of the plasma in front of the target, there is not sufficient space for resonance absorption

to occur. However, Brunel heating is similar to resonance absorption because the electric field of the laser still drives a plasma wave. In Brunel heating, at the plasma-vacuum interface, the intense laser electric field drives a plasma wave that pulls the electrons out of the plasma into vacuum and then sends the electrons back into the plasma with a random phase.

The fraction of laser energy absorbed by the plasma was empirically determined by Brunel to be

$$f_{BH} = \frac{\eta}{2\pi} \frac{v_{os}^3}{v_L^2 c \cos\theta} \tag{2.59}$$

where η is the efficiency factor. The efficiency factor describes how much oscillatory motion of the electrons is lost to heating the plasma, which Brunel determined to be $\eta \approx 1.75$. Kato *et al.* [48] later determined that the efficiency factor could depend on the hot electron density given by

$$\eta \approx \frac{1}{\left(1 - \omega_0^2/\omega_p^2\right)}, \tag{2.60}$$

which is the only place where the density dependence appears in the absorption fraction. Therefore, with increasing the laser intensity, density and incidence angle the fraction of laser energy absorbed by Brunel heating increases. For an intensity value around $I\lambda^2 \approx 10^{16}$ Wcm$^{-2}\mu$m^2 and small scale-lengths $L/\lambda \sim 0.1$, the absorption can be as high as 70% [35]. However, at higher intensities and shorter scale lengths, the absorption saturates to around 10-15%.

2.1.4.4 J × B Heating

For high intensities, the absorption mechanism that becomes predominant is $\mathbf{J} \times \mathbf{B}$ heating. In this case, oscillations in the ponderomotive force are the source of $\mathbf{J} \times \mathbf{B}$ heating [36]. The non-relativistic ponderomotive force is given by eq. (2.16). For a linearly polarized wave represented by $\mathbf{E} = E_0(x)\sin(\omega t)$, the ponderomotive force, which is a longitudinal force term, becomes

$$\mathbf{F}_{pond} = -\frac{m}{4} \frac{\partial v_{os}^2}{\partial x} \left(1 - \cos 2\omega t\right) \tag{2.61}$$

from using the definition of the electron quiver velocity and the power-reducing formula for the trigonometric function. The $\cos 2\omega t$ term in the parentheses is the

high-frequency component referred to as the $\mathbf{J} \times \mathbf{B}$ term. The $\mathbf{J} \times \mathbf{B}$ force oscillates the electrons at the critical surface at twice the laser frequency in the direction of the k vector of the laser. Depending on the phase of the oscillating electrons, they may gain energy from the laser EM wave, decouple, and be propelled into the overdense plasma. The number of electrons that escape the wave and get propelled into the overdense plasma depends on the strength of the oscillating force.

2.2 Proton Acceleration

The laser absorption mechanisms previously discussed results in the heating of some fraction of the electrons to energies much higher than the initial bulk plasma temperature. These hot electrons travel through the target at a speed close to the speed of light, forming a hot electron cloud at the rear surface of the target, which induces a strong sheath electric field that accelerates ions present on the surface. This mechanism is known as Target Normal Sheath Acceleration (TNSA). Hatchett *et al.* [24] and Wilks *et al.* [25] describe this process in more detail, which is presented below. This TNSA mechanism for ion acceleration can be described by a one-dimensional plasma expansion into vacuum following the derivations of Mora [49, 50] and Baitin and Kuzanyan [51]. Since the first observations of the acceleration of multi-MeV protons from the rear surface of a target [17, 18, 23], several experiments have been carried out to measure the characteristics of the generated proton beam [1,24–32]. A brief overview of the previous studies provides the background of the work presented in this thesis.

2.2.1 Target Normal Sheath Acceleration (TNSA)

In target normal sheath acceleration, the accelerated ions originate from a thin layer of contaminants on the surface of the target. The contaminant layer, which is is composed of C, O and H [26], is a result of water vapor that can be present in the vacuum chamber or due to vacuum pump oil [27, 52]. The protons from the contaminant layer are accelerated more rapidly than the other species due to their higher charge to mass ration. Very hot electrons are generated through the

laser target interaction and travel through the thin target in a broad angular beam. A few of the hot electrons will escape from the rear surface of the target, leaving a positive charge on the target. At the rear surface of the target, the electrons are expected to relax to a Boltzmann equilibrium while there is a steep ion density gradient. A Coulomb potential is built up on the target causing the rest of the electrons to become trapped, recirculating through the target and spreading out transversely. The electrons set up a sheath field with a scale length given by the Debye length of the hot electrons. A cartoon of the initial stages of target normal sheath acceleration is displayed in Fig. 2.2. The Debye length is defined as the

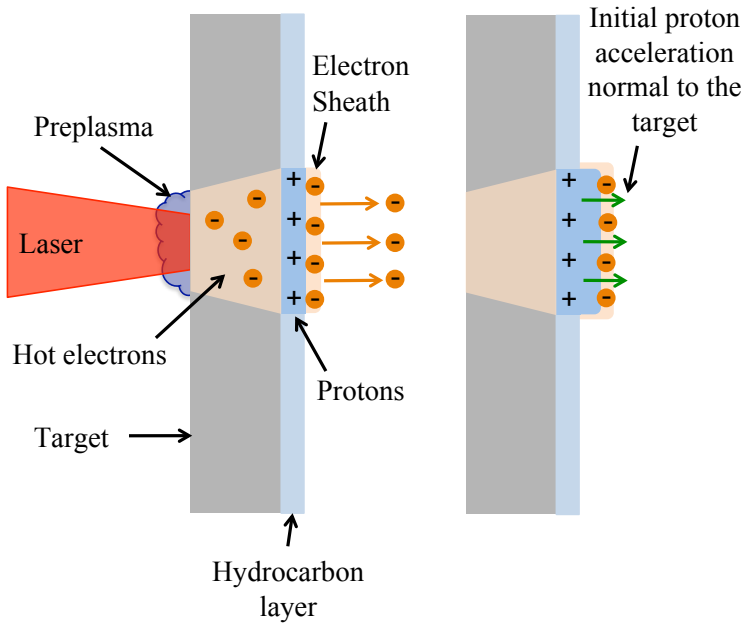

Figure 2.2: Cartoon of TNSA. Hot electrons travel through the target and a small fraction of the hot electrons escape from the rear surface creating a potential well which traps the remaining hot electrons. The hot electrons set up an electric sheath field on the rear surface which is strong enough to ionize the material and accelerate the protons, which are the lightest particles. The protons are initially accelerated normal to the target surface.

length in which the electrons screen out electric fields in the plasma, which is a function of the hot electron temperature and density, T_{ehot} and n_{ehot} respectively,

given by

$$\lambda_{De} \equiv \sqrt{\frac{kT_{ehot}}{4\pi n_{ehot} e^2}}. \tag{2.62}$$

The sheath field is

$$\mathbf{E}_{sheath} \approx \frac{k_B T_{ehot}}{e\lambda_{De}} \left(\frac{MV}{\mu m} \right). \tag{2.63}$$

For example, a laser intensity of $\sim 10^{19}$ Wcm^{-2} can produce a sheath field on the order of 10^{12} V/m. Such a strong electrostatic field can ionize the particles in the contaminant layer and accelerate the ions, where the lightest ions are the protons. The protons are initially accelerated normal to the unperturbed surface.

The electrons and protons are accelerated away from the target during the expansion. After the initial acceleration, further away from the target at the front of the expansion, the local hot electron Debye length is larger than the local ion scale length and a Debye sheath is formed. There is a net negative charge at the leading edge of the expansion followed by the ion front. Between the leading edge and the ion front, a constant electrostatic field exists, with the magnitude given by

$$|\mathbf{E}| \approx \frac{k_B T_{ehot}}{e l_{ion}}, \tag{2.64}$$

where l_{ion} is the scale length of the ions. Since the electrostatic field inversely scales with the ion density scale length, the electrostatic field is the greatest at the beginning were there is a steep ion density. Behind the ion front, the ion and hot electron density will fall off exponentially and the plasma cloud is said to be quasineutral. A representation of this mechanism is present in Fig. 2.3. The ions will continue to be accelerated after the laser pulse is over until the hot electrons lose all of their energy through accelerating the ions (i.e. adiabatic cooling).

The ions that are accelerated first come from the region near the laser axis where the most energetic electrons are located and escape the target. From experimental data, it is shown that the ion beam source size decreases with increasing ion energy because the ions that are accelerated for the longest amount of time will reach the highest energies and originate near the laser axis. As the hot electrons recirculate through the target and spread transversely, ions are then accelerated from the outer regions of the target at later times and therefore do not reach higher energies.

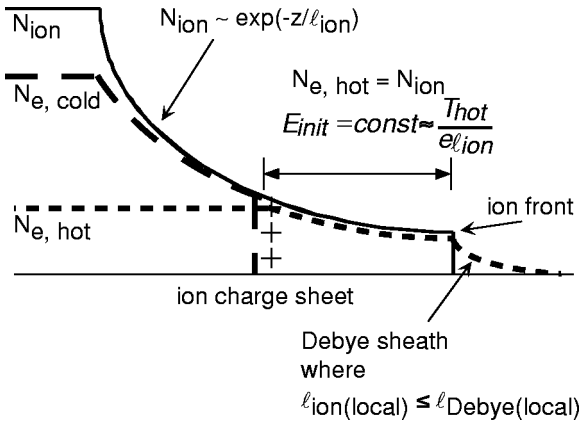

Figure 2.3: (a) Schematic of Target Normal Sheath Acceleration (TNSA). Figure taken from Hatchett *et al.*, Physics of Plasmas (2000) [24].

The acceleration of the proton beam from the target can be analyzed by looking at a one-dimensional plasma expansion into vacuum. The expansion can be treated two ways: isothermally and adiabatically. In an isothermal expansion model, an external energy source is assumed to supply the required energy to the electrons in order to maintain the electron temperature. On the other hand, an adiabatic expansion model includes energy loses of the electrons as they give up energy to the accelerating ions. We will discuss the two models below. The derivation for the isothermal model is taken from Mora [49] and the adiabatic model follows Mora [50], Baitin and Kuzanyan [51] and Hey *et al.* [53].

For simplicity in the plasma expansion model, we assume that the plasma occupies the half space $x < 0$. In the plasma, the ions are cold and initially at rest, $n_i = n_{i0}$, and there are no ions initially present where $x > 0$, $n_{i0} = 0$. At $x = 0$ there is a sharp ion boundary. On the other hand, the electrons are continuous across the boundary represented by the Boltzmann distribution

$$n_e = n_{e0} exp\left(\frac{e\phi}{k_b T_e}\right) \tag{2.65}$$

where n_{e0} is the electron density in the unperturbed plasma, ϕ is the electrostatic potential and T_e is the electron temperature. The electrostatic potential satisfies

the Poisson equation

$$\epsilon \frac{\partial^2 \phi}{\partial x^2} = e\left(n_e - Z n_i\right). \tag{2.66}$$

Before expansion, the electrons are in thermal equilibrium. During expansion, $t > 0$, the electrons are assumed to stay in equilibrium so the Boltzmann and Poisson equation still holds. For the expansion into vacuum the ions can be described by the equation of motion and the continuity equation:

$$\frac{\partial v_i}{\partial t} + v_i \frac{\partial v_i}{\partial x} = -\left(\frac{Ze}{m_i}\right) \frac{\partial \phi}{\partial x} \tag{2.67}$$

$$\frac{\partial v_i}{\partial t} + v_i \frac{\partial n_i}{\partial x} + n_i \frac{\partial v_i}{\partial x} = 0. \tag{2.68}$$

Assuming quasineutrality of the plasma, $n_e = Z n_i$ and using the Boltzmann distribution of the electrons, eq. (2.67) can be written in the form

$$\frac{\partial v_i}{\partial t} + v_i \frac{\partial v_i}{\partial x} = -\frac{c_s^2}{n_i} \frac{\partial n_i}{\partial x} \tag{2.69}$$

where c_s is the ion-acoustic velocity given by

$$c_s = \sqrt{\frac{Z k_B T_e}{m_i}}. \tag{2.70}$$

2.2.1.1 Isothermal Expansion

For the isothermal model, the electron temperature is constant during the expansion where an external source supplies the needed energy. Since the temperature is constant, the condition of the expansion is described in terms of a characteristic velocity instead of a characteristic length. Therefore, all quantities depend on the space and time parameters through the ratio x/t, which has the dimensions of velocity. The ratio is expressed by a single variable $\xi = x/t$. Using the variable ξ, a non-trivial self-similar solution can be found using the continuity equation and the equation of motion.

The derivation representation in (2.68) and (2.69) become

$$\frac{\partial}{\partial x} = \frac{1}{t}\frac{d}{d\xi} \text{ and } \frac{\partial}{\partial t} = -\frac{\xi}{t}\frac{d}{d\xi}. \tag{2.71}$$

(2.68) and (2.69) reduce to

$$(v_i - \xi)\frac{dn_i}{d\xi} + n_i\frac{dv_i}{d\xi} = 0 \tag{2.72}$$

and

$$(v_i - \xi)\frac{dv_i}{d\xi} = -\frac{c_s^2}{n_i}\frac{dn_i}{d\xi} \tag{2.73}$$

To find a non-trivial solution for the velocity, eliminate $dn_i/d\xi$ and $dv_i/d\xi$ from (2.72) and (2.73) and solve for velocity, which results in

$$v_i = c_s + \frac{x}{t}. \tag{2.74}$$

Substituting (2.74) into (2.68) results in a self-similar solution for the ion density

$$n_i = n_{i0}exp\left(-\frac{x}{c_s t} - 1\right) \tag{2.75}$$

Plugging in the self-similar solution into (2.69) gives the self-similar electric field

$$\mathbf{E}_{ss} = \frac{k_b T_e}{e c_s t}. \tag{2.76}$$

From the self-similar solution, the spectrum for the ions can also be calculated. For the spectrum, we want the number of ions per unit area per energy. The number of ions per unit area is given by the self-similar solution of the Boltzmann distribution. The distribution can be written in terms of energy by writing the ion energy as

$$\mathcal{E}_i = \frac{m_i}{2}v_i^2 = \frac{m_i}{2}\left(c_s + \frac{x}{t}\right)^2. \tag{2.77}$$

Rearranging (2.77) results in

$$\sqrt{\frac{2\mathcal{E}_i}{Zk_BT_e}} = \left(\frac{x}{c_s} + 1\right) \tag{2.78}$$

by using (2.70). (2.77) can then be substituted into the Boltzmann distribution to obtain

$$n_i = n_{i0}exp\left(-\sqrt{\frac{2\mathcal{E}_i}{Zk_BT_e}}\right). \tag{2.79}$$

The derivative can be taken with respect to the ion energy and noting that the plasma expands spatially by a distance $c_s t$, gives the number of ions per surface area and unit energy

$$\frac{dN}{d\mathcal{E}} = \frac{n_{i0}c_s t}{\sqrt{2\mathcal{E}_i Zk_BT_e}}exp\left(-\sqrt{\frac{2\mathcal{E}_i}{Zk_BT_e}}\right), \tag{2.80}$$

which is the isothermal ion distribution function. However, this model assumes constant sound speed and does not include electron energy loses, which could over predict the maximum ion energy

2.2.1.2 Adiabatic Expansion

In contrast to the isothermal model, in the adiabatic model the electron temperature is not constant because the electrons cool down when they part their energy to the ions. For the adiabatic model, the Poisson equation, equation of motion and the continuity equation still hold. Consider a one-dimensional Gaussian plasma with an initial ion density of

$$n_{i0}\left(x, t=0\right) = n_{i0} exp\left(\frac{-x^2}{R_0^2}\right), \tag{2.81}$$

where R_0 is the initial characteristic length of the plasma. The electrons are still expressed by (2.65) with the temperature as a function of time and (2.68) and (2.69) still hold. The self-similar solution given by the ion density is

$$n_i(x,t) = n_{i0}\frac{R_0}{R(t)} exp\left(-\frac{x^2}{R(t)^2}\right) \tag{2.82}$$

where $R(t)$ is the characteristic length, which is to be determined. For simplicity, in the following equations, $R(t) = R$. Plugging the self-similar solution (2.82) into (2.68) results in an ion velocity given by

$$v_i = \frac{dR}{dt}\frac{x}{R}. \tag{2.83}$$

Substituting (2.83) into (2.69) results in

$$\frac{d^2R}{dt^2} = 2\frac{c_s^2}{R}. \tag{2.84}$$

The characteristic length, R, can be related to the electron temperature by evaluating the adiabatic equation of state for motion with one degree of freedom, neglecting heat flow, which is derived by taking the moments of the Vlasov equation. The energy equation is

$$\left(\frac{\partial}{\partial t} + v\frac{\partial}{\partial x}\right)\ln p - \left(\frac{\partial}{\partial t} + v\frac{\partial}{\partial x}\right)\ln n^3 = 0, \tag{2.85}$$

where p is the electron pressure. The electron pressure is written in terms of the electron temperature by the ideal gas relationship $p = nT$. Substituting into (2.85) results in

$$\frac{n_e}{T_e}\left(\frac{\partial}{\partial t} + v\frac{\partial}{\partial x}\right)T_e - 2\left(\frac{\partial}{\partial t} + v\frac{\partial}{\partial x}\right)n_e = 0. \tag{2.86}$$

The electron density can be substituted in terms of R, assuming that the electron and ion velocities are equal, by substituting the ion velocity given by (2.83) into the continuity equation (2.68) for electrons. The energy equation becomes

$$\frac{1}{T_e}\left(\frac{\partial}{\partial t} + v\frac{\partial}{\partial x}\right)T_e = -\frac{2}{R}\left(\frac{\partial}{\partial t} + v\frac{\partial}{\partial x}\right)R. \tag{2.87}$$

This implies that $T_e = T_{e0}R_0^2/R^2$, where T_{e0} is the initial electron temperature. Therefore, (2.84) becomes

$$\frac{d^2R}{dt^2} = 2\frac{c_{c0}^2R_0^2}{R^3} \tag{2.88}$$

where $c_{s0} = \sqrt{Zk_BT_{e0}/m_i}$ is the initial value of the ion acoustic velocity. Integrating (2.88) twice, the value of $R(t)$ is obtained,

$$R(t) = \sqrt{R_0^2 + 2c_{s0}^2t^2}, \tag{2.89}$$

which makes the electron temperature

$$T_e = T_{e0}\frac{R_0^2}{R_0^2 + 2c_{s0}^2t^2}. \tag{2.90}$$

Substituting (2.89) into (2.82) and (2.83) results in

$$n_i(x,t) = \sqrt{\frac{R_0^2n_{i0}^2}{R_0^2 + 2c_{s0}^2t^2}}exp\left(\frac{-x^2}{R_0^2 + 2c_{s0}^2t^2}\right) \tag{2.91}$$

and

$$v_i = x\frac{2c_{s0}^2t}{R_0^2 + 2c_{s0}^2t^2}. \tag{2.92}$$

To describe the behavior, an energy spectrum in the form of $dN/d\mathcal{E}$ is obtained by $\frac{dN}{d\mathcal{E}} = \frac{dN}{dx}\frac{dx}{d\mathcal{E}}$, where $\frac{dN}{dx} = n_i(x,t)$. Using the energy equation, $\mathcal{E}_i = m_iv_i^2$, and substituting for the velocity, the ion energy becomes

$$\mathcal{E} = \frac{2m_ic_{s0}^4t^2x^2}{\left(R_0^2 + 2c_{s0}^2t^2\right)^2}. \tag{2.93}$$

Therefore

$$\frac{d\mathcal{E}}{dx} = \frac{4m_i c_{s0}^4 t^2 x}{\left(R_0^2 + 2c_{s0}^2 t^2\right)^2}. \tag{2.94}$$

Combining (2.91) and (2.94), the ion distribution is

$$\frac{dN}{d\mathcal{E}} = \frac{n_{i0} R_0}{\sqrt{T_{eff}\mathcal{E}}} exp\left(\frac{\mathcal{E}}{T_{eff}}\right) \tag{2.95}$$

where

$$T_{eff} = \frac{2c_{s0}^4 t^2 m_i}{R_0^2 + 2c_{s0}^2 t^2}. \tag{2.96}$$

The distribution is a function of time and is similar to a 1D Maxwellian energy distribution with an effective temperature, T_{eff}, which is also a function of time. In the limit where $t \to \infty$, the distribution relaxes to a distribution with a temperature given by the hot electron temperature,

$$\frac{dN}{d\mathcal{E}} = \frac{n_{i0} R_0}{\sqrt{T_0 \mathcal{E}}} exp\left(\frac{\mathcal{E}}{T_{e0}}\right). \tag{2.97}$$

This is the functional form of the distribution, which we will fit to our experimental data in the proceeding chapters in order to gain an understanding of the proton generation.

2.2.2 Previous Studies

The observation of the emission of energetic ions from laser-produced plasmas has been around since the early 1960's [54]. Over the past five decades, the laser has developed with the advent of chirped pulse amplification leading to higher laser intensities. This new regime allowed for a continuous study of the proton characteristics for different scenarios. Within the last decade, it was observed that a highly directional, intense proton beam can be generated during the interaction of an ultraintense laser pulse with a thin solid target [17, 18, 23]. Observations from these experiments and others revealed proton conversion efficiencies from 2% to 7%, maximum proton energy of 55 MeV and a half-cone angle of emission of 15° to 20° degrees [17, 28, 55]. The generated proton beam was observed to be highly laminar and have a smooth angular distribution [1, 29, 56]. As mentioned in chapter one, for proton fast ignition to be viable, a laser to proton conversion

efficiency around 15% is required and the proton beam needs to deliver its energy to the core in a 40 μm diameter spot. Previous studies have investigated the dependence of proton conversion efficiency on target and laser parameters [30–32]. In addition, focusing of the proton beam was demonstrated by adjusting the target geometry [2, 20, 57]. These studies are presented here.

2.2.2.1 Conversion Efficiency

The dependence of conversion efficiency and maximum proton energy on different laser parameters has been studied with a series of experiments by Fuchs *et al.* [30] using 25 μm Al foils where the laser energy and pulse length were varied for laser intensities in the range of $10^{18} - 10^{19}$ Wcm^{-2}. The experimental results were compared to the self-similar isothermal model, which was previously discussed. However, in the model the acceleration time of the ions, t_{acc}, was limited by $t_{acc} \sim 1.3\tau_{laser}$ where τ_{laser} is the laser pulse length, which was found to be in good agreement with the experimental results. Fig. 2.4 displays the dependence of the maximum proton energy and conversion efficiency on the laser energy and Fig. 2.5 shows the dependence on the laser pulse duration. It can be seen from Fig. 2.4 that the maximum proton energy and conversion efficiency increases with an increase in laser energy and intensity and is in good agreement with the isothermal model prediction. The plasma expansion model also agrees with the experimental results when the laser pulse length is varied with a constant laser energy as seen in Fig. 2.5; however, the dependence on pulse length is weak.

Within the same intensity regime Hey *et al.* [31] investigated the effect of the target thickness on the maximum proton energy and conversion efficiency. It was determined that for a target thickness greater than 20 μm, the conversion efficiency scales as $1/L$, where L is the target thickness. For targets thinner than 20 μm, the conversion efficiency is independent of target thickness because the amount of work the electrons put into the adiabatic expansion of the target is greater than the frictional loss in the bulk plasma. The maximum proton energy observed is similar for targets less than 20 μm and decreases for thicker targets.

Robson *et al.* [32] extended the work done by Fuchs *et al.* [30] by increasing

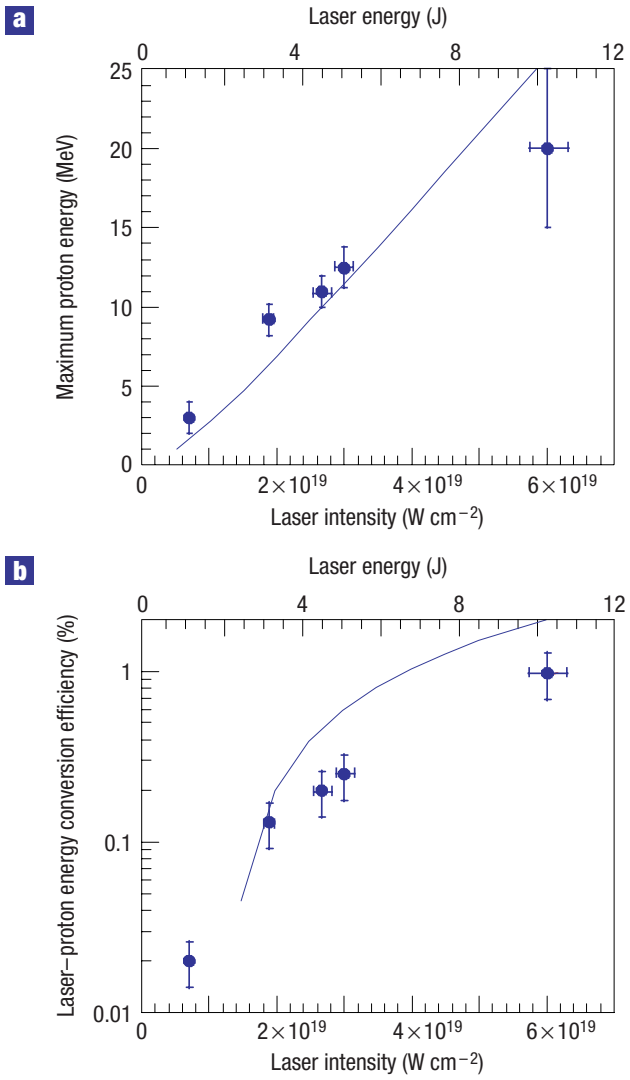

Figure 2.4: (a) Maximum proton energy and (b) proton conversion efficiency for various laser energies (top axis) and intensities (bottom axis) at a constant laser pulse length of 320 fs. The conversion efficiency is calculated for protons > 4 MeV. The targets were 25 μm thick Al foils. The blue lines are calculated from the isothermal fluid model. Figure taken from Fuchs *et al.*, Nature Physics (2005) [30].

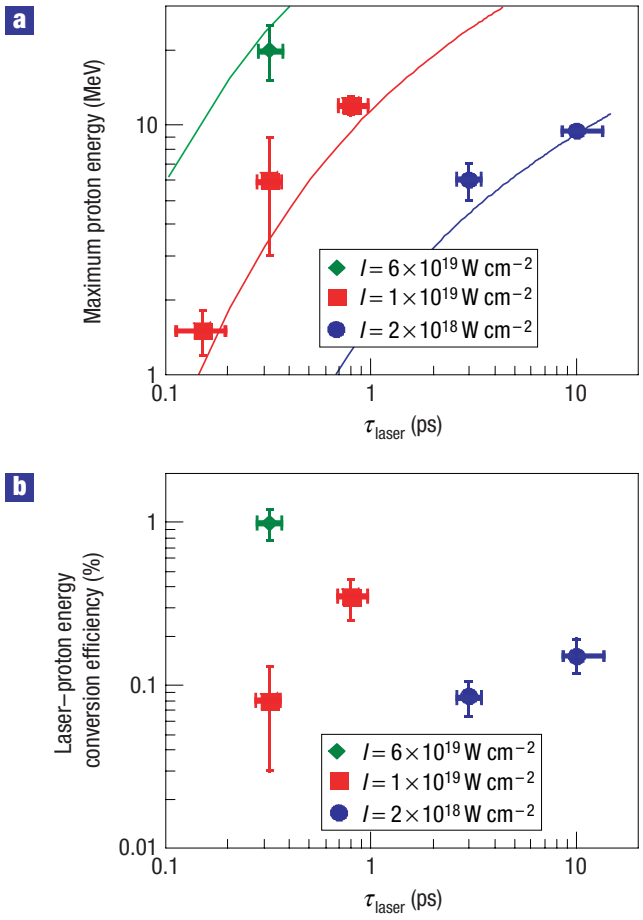

Figure 2.5: (a) Maximum proton energy and (b) proton conversion efficiency as a function of laser pulse length for three different laser intensities. The laser energy was varied to obtain different intensities for the two points at the same pulse length. The conversion efficiency is calculated for protons > 4 MeV and the targets were 25 μm thick Al foils. The lines in (a) are calculated from the isothermal fluid model. Figure taken from Fuchs *et al.*, Nature Physics (2005) [30].

the laser energy, intensity, and pulselength up to 400 J, 6×10^{20} Wcm^{-2}, and 10 ps, respectively. It was found that the isothermal plasma-expansion model accurately predicts the proton behavior for intensities up to 6×10^{19} Wcm^{-2} as presented by Fuchs *et al.* [30]. However, at an order of magnitude higher intensity, a revised model involving two phases of the electron temperature and incorporating three-dimensional effects better represents the experimental results. For the two-phase electron temperature, the electron temperature rises linearly with the pulse duration in the first phase and the second phase consists of the electron temperature decreasing adiabatically [50]. The three-dimensional effects (i.e. radial expansion of the hot electrons) are mimicked by stopping the electron acceleration when the plasma expansion in the longitudinal direction becomes twice as long as the initial transverse dimension of sheath on the back of the target. Fig. 2.6 displays the experimental results for the maximum proton energy at various laser intensities, which are compared to the analytical models. As seen in Fig. 2.6, the maximum proton energy (MeV) observed in experiments increases with increasing laser intensity using 1 ps pulses.

2.2.2.2 Focusing

Focusing of the generated proton beam has been shown in simulations where the rear surface of the target is curved [25]. Proton focusing using hemispherical shell targets was first demonstrated experimentally by Patel *et al.* [20]. In the experiment, an ultra-intense laser delivering 10 J in a 100 fs pulse duration, irradiated either 10 μm thick Al planar foils or 10 μm thick, 320 μm diameter hemispherical shells. A schematic of the experimental set-up is seen in Fig. 2.7a. The generated proton beam from these targets isochorically heated a secondary 10 μm thick Al foil placed 250 μm behind the planar foil and at the plane of the geometric center of the shell. Planckian thermal emission from the rear side of the secondary Al foil was recorded using a fast optical streak camera in order to determine the temperature and size of the heated region. The resultant images are displayed in Fig. 2.7b. With the planar foil, an emission region of 186 μm FWHM was observed. A heated region of 46 μm FWHM, a factor of four reduction in spatial extent and

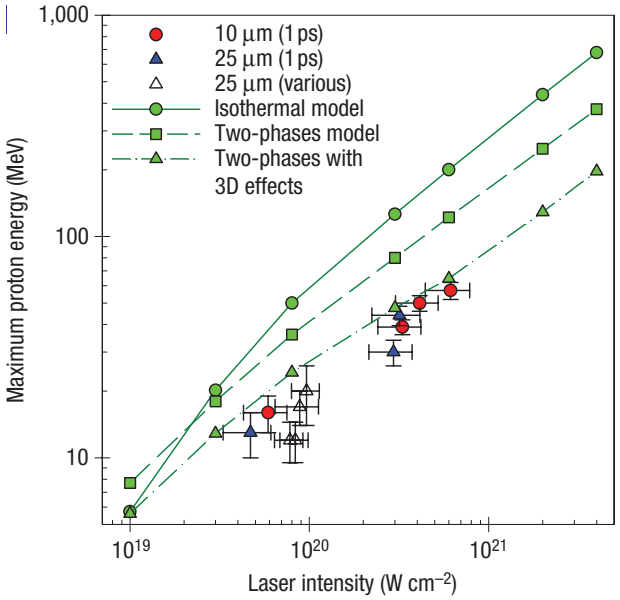

Figure 2.6: Maximum proton energy as a function of laser intensity at a constant laser pulse length of 1 ps. The targets were Al foils, where the thickness is indicated by the different markers. For the 25 μm thick foils represented by the open triangles, both the laser energy and pulse length were varied. The various green lines represent the fits for the different models. Figure taken from Robson *et al.*, Nature Physics (2006) [32].

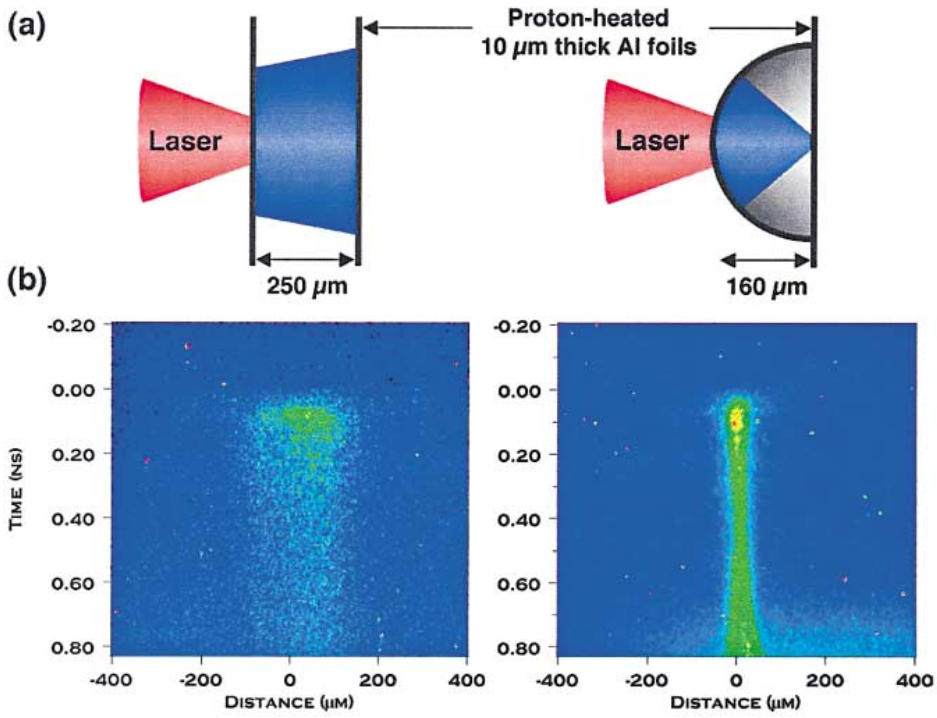

Figure 2.7: (a) Schematic of the experimental set-up. Laser irradiates a flat or hemispherical foil, which generates a proton beam that heats a secondary foil. (b) Space and time resolved images from a streak camera of the thermal emission from the rear side of the secondary foil. Figure taken from Patel *et al.*, Phys. Rev. Lett. (2003) [20].

an increase in emission intensity, was observed with the hemispherical shell. This leads to a 16 times smaller heated area in the hemispherical case compared to the planar foil.

Proton focusing was further explored by Snavely *et al.* [2]. Using 360 μm diameter, 13-16 μm thick Al hemispherical shells, the position of best focus was determined by varying the position of the secondary foil. A 100 μm thick Al slab was placed at various distances from the apex of the hemisphere, scanning the focusing region. The hemispherical shell was irradiated by a 170 J laser pulse in 700 fs; more energetic and longer than the laser used by Patel *et al.* [20], but near the same intensity $\sim 3 \times 10^{18}$ Wcm^{-2}. For a 100 μm Al slab, 3.5 MeV protons dominate the heating of the foil. The Planckian emission from the rear surface of the foil was imaged using a time-integrated extreme-ultraviolet light (XUV) imaging microscope. From the images, the temperature and size of the heated region was deduced. The minimum plasma jet waist was determined to be located at $D/r = 1.8 \pm 0.4$, where D is the distance from the apex of the shell to the rear surface of the foil and r is the radius of the shell, and the highest temperature produced on the rear surface was 81 eV.

Instead of using a hemispherical shell, collimation of the proton beam was demonstrated by Kar *et al.* [57] using a secondary target. The self-charging of a secondary target attached to the laser irradiated target improved the collimation of the proton beam. The laser irradiated a 15 μm thick Au foil, delivering 300 J on target in 500-600 fs resulting in a peak intensity of $\sim 10^{21}$ Wcm^{-2}. The Au foil was attached to two different shaped geometries made out of Al, cylindrical and rectangular, which acted as an electrostatic lens. The inner diameter of the cylindrical lens and the height of the regular lens varied from 0.6 mm to 2 mm, while the width of the rectangular lens was held constant at 0.5 mm. The length and thickness of the lens were also varied from 1 mm to 2 mm and 0.5 mm to 1 mm, respectively.

After the small fraction of the hot electrons escape the target due to the laser interaction, a potential builds up in the target and spreads transversely. The time dependence of the potential is dependent on the self-capacitance of the target.

For the time scales in their experiment, the target potential remains above several MV. The potential of the target is assumed to be constant after the charge wave reaches the end of the target. The time it takes for the charge wave to reach the end of the target, t_{ss}, is estimated by $r_0 + 0.75ct_{ss} = G/2 + L$ where r_0 is the radius of the laser spot size, and G and L are the inner diameter and length of the cylindrical lens. The charge wave creates a strong transverse electric field on the edge of the target which acts to reduce the divergence of the proton beam inside of the lens. A reduction factor of two was observed in the proton beam divergence angle when the proton beam traveled through the electrostatic lens compared to the free-standing foils. Collimation of the proton beam increased when the aspect ratio of the lens height and length is decreased and the thickness of the wall is decreased as seen in Fig. 2.8. However, the overall spectral shape and proton cut-off energy were not affected by the addition of the lens, suggesting that the lens does not affect the accelerating fields.

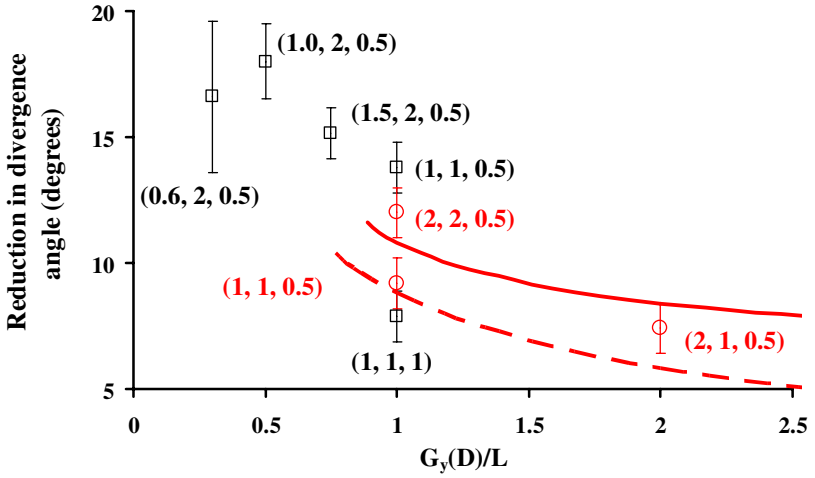

Figure 2.8: (a) Reduction in the proton beam divergence angle using rectangular and cylindrical lens targets represented by the squares and circles, respectively. The x-axis is the ratio of the height (G_y) of the rectangular lens or the diameter of the cylindrical lens (D) over the length of the lens (L). The dimensions of the lens (in mm) is noted next to the data points by (G_y(D), L, T) where T is the wall thickness of the lens. All of the rectangular lens have a width of 0.5 mm. The solid (dotted) lines are simulated values for a cylindrical lens with T = 0.5 μm and D = 2 mm (1 mm). Figure taken from Kar *et al.*, Physical Review Letters (2008) [57].

The work presented in this thesis stems from the results of these experiments. Due to the high laminarity of the proton beam, it is believed that after the protons are accelerated from the rear surface of the target, the protons move in straight line trajectories. Based on this assumption, we aimed to determine the focusing characteristics of the proton beam (i.e. spot diameter and position) by tracing the proton trajectories using straight lines. This would be a more direct approach to determine the focusing characteristics of the proton beam compared to the indirect heating measurements used by Patel *et al.* [20] and Snavely *et al.* [2]. For proton fast ignition described in the previous chapter, the hemispherical shell needs be placed with a surrounding cone. We extended our study to investigate the effect of a surrounding structure on the proton beam focusing characteristics, which should be improved based on the experimental findings by Kar *et al.* [57]. However, the over size scale of our targets for fast ignition is 2 to 3 times smaller than that presented by Kar *et al.* [57]. The experimental findings are presented in Chapter 4.

2.3 Applications

The conversion efficiency and focusing of energetic protons/ions are of interest to several other fields besides proton fast ignition. The ability to generate high intensity well-focused proton beams will potentially open the door to new regimes in high-energy-density science as well as enable a broad range of new applications. For example, an intense multi-MeV proton beam incident on solid density or compressed material can create teraPascal pressures, allowing the study of the properties of warm dense matter found in the interior of giant planets like Jupiter [58]. A proton beam from a point like source can be used in radiography to image small scale features as they change in time [59, 60]. Laser produced proton beams are also making an impact on medical applications such as isotope production [61] for Positron Emission Tomography (PET) and proton oncology [62]. In addition, energetic proton/ion beams are used to produce highly directional neutrons for applications in medicine, material science, and neutron resonance

spectroscopy [63, 64].

Chapter 3

Laser system and diagnostics

3.1 Trident laser system

Experiments were conducted on the 200 TW Trident short pulse CPA (Chirped Pulse Amplification) [65] laser at the Los Alamos National Laboratory [66] [67]. The Trident laser system delivered 70 - 80 J on target in 500 - 600 fs with an amplified spontaneous emission (ASE) contrast ratio (ratio of the intensity in the main pulse to the intensity of the amplified stimulated emission pedestal) better than 10^{-9} [68].

A laser diode pumped, self-mode-locked glass laser constitutes the front end of the laser system [67]. A diagram of the front end of the laser system is seen if Fig. 3.1. The pulse originates from a GLX-200 Nd:Glass (neodymium-glass) laser diode pumped oscillator from Time Bandwidth Products. The oscillator is pumped by 2 J of 800 nm light that excites the Nd:Glass crystal in the cavity which is mode-locked at 1054 nm and 76 MHz. To limit the nonlinear effects in order to obtain high laser intensities, 1) The pulses are temporally stretched by passing four times though a stretcher containing a 1740 lines per mm dielectric grating and a 170 cm focal length lens. A Pockels cell down-selects the frequency from 76 MHz to 150 Hz containing $\sim$ 1 nJ of energy. 2) The pulse is then amplified to 1 mJ in a Positive Light Legend Ti:Sapphire regenerative amplifier by passing through the cavity $\sim$ 20 times within a few ns. During the amplification, the crystal can produce coherent light, which is referred to as amplified stimulated emission (ASE)

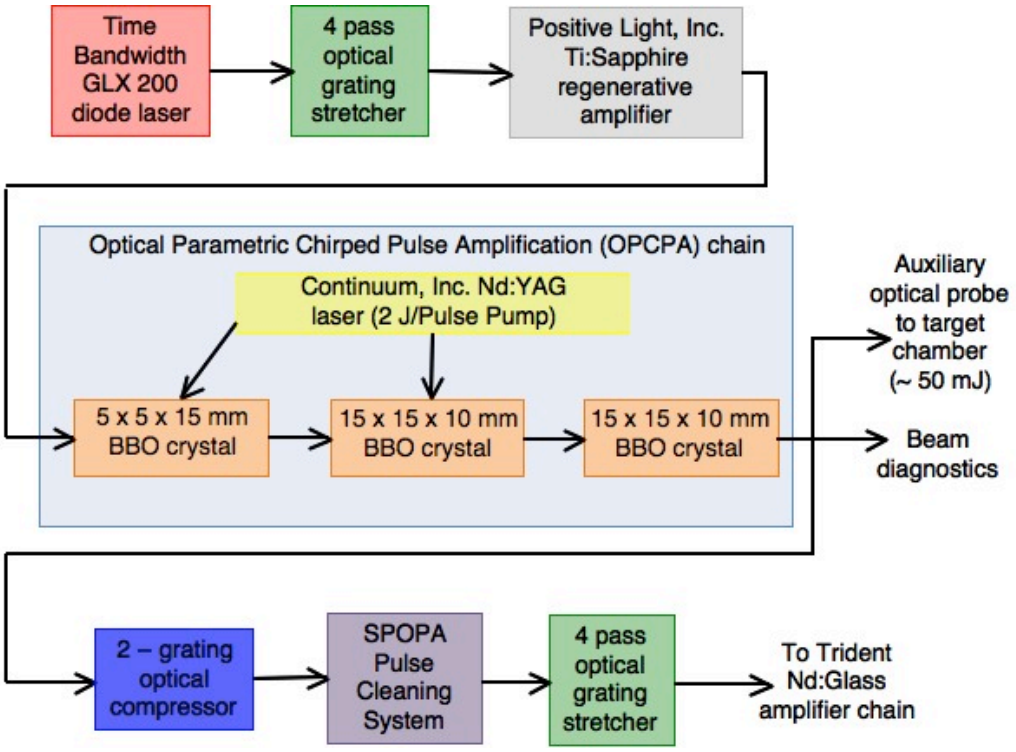

Figure 3.1: Front-end of the Trident laser system. Diagram modified from Fig. 3-17 in [69]. Original diagram constructed by Randall P Johnson.

and can leave the amplifier with the main pulse through a Pockels cell. The ASE is not compressed by the gratings and can reach the target before the main pulse, disturbing the target and creating preplasma. To decrease the ASE produced and increase the intensity contrast of the laser to the prepulse, the pulse is sent through an optical parametric chirped pulse amplification (OPCPA) chain [70, 71]. In the chain, the main pulse is overlapped with a seed pulse from a secondary laser and passes through a series of BBO (BaB_2O_4) crystals. The secondary laser is a 2 J pulse pump Powerlite+ Nd:YAG laser from Continuum, Inc. and the pulse is frequency doubled. Photons in the seed pulse are down-converted to the photons in the main pulse, with the leftover energy being in a third idler pulse and carried out of the crystal so no energy is stored in the crystal to produce ASE.

From the OPCPA chain, the pulse is compressed and is cleaned by a technique called *low-gain* OPA (Optical Parametric Amplification) to further increase the intensity contrast of the laser to the prepulse. Shah *et al.* developed the scheme of *low-gain* OPA (Optical Parametric Amplification), which is explained in detail in Ref. [68]. The technique allows an intensity contrast $<10^{-9}$.

After the pulse is cleaned, it passes four times through an optical grating stretcher before it passes to the amplifier chain. The laser path from the amplifier chain to the target chamber is seen in Fig. 3.2. The amplifier chain consists of 4

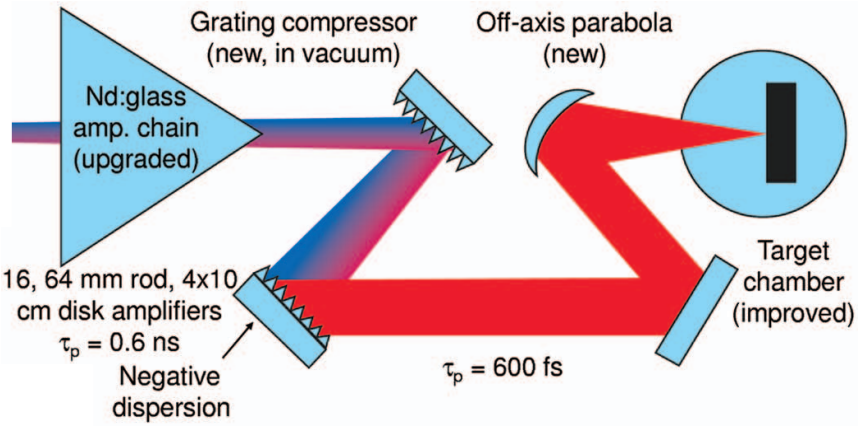

Figure 3.2: Short pulse beam path from the amplifier chain to the target chamber. Figure taken from Batha *et al.*, Rev. Sci. Instru. (2008) [67].

neodymium doped glass rods (Nd:Glass) with diameters of 16, 25, 45, and 64 mm, which amplify the pulse to 5 J. A deformable mirror is placed within the amplifier chain to correct for distortions in the beam caused by thermal emission from the amplifiers and allows the laser to be focused to a relatively small focal spot. To increase the energy of the laser beam to over 150 J, a 10 cm disk amplifier was added near the end of the chain. An optical periscope is used to bring the laser beam to ground level. The beam enters a $5 \times 5 \times 10$ ft^3 vacuum chamber where it is compressed by a set of 40×80 cm^2 dielectric gratings with 1740 lines per mm to less than 600 fs full width half maximum (FWHM). After compression, the beam travels through a vacuum tube into the target chamber where it is redirected by a turning mirror and focused off of an off-axis parabolic $f/3$ ($f/8$) mirror onto the target with a 7 μm FWHM (25 μm FWHM) reaching a peak intensity on target of 10^{20} Wcm^{-2} (10^{19} Wcm^{-2}). On target, the laser delivers between 70 - 80 J in approximately 500 - 600 fs. A picture of the Trident target chamber is shown in Fig. 3.3.

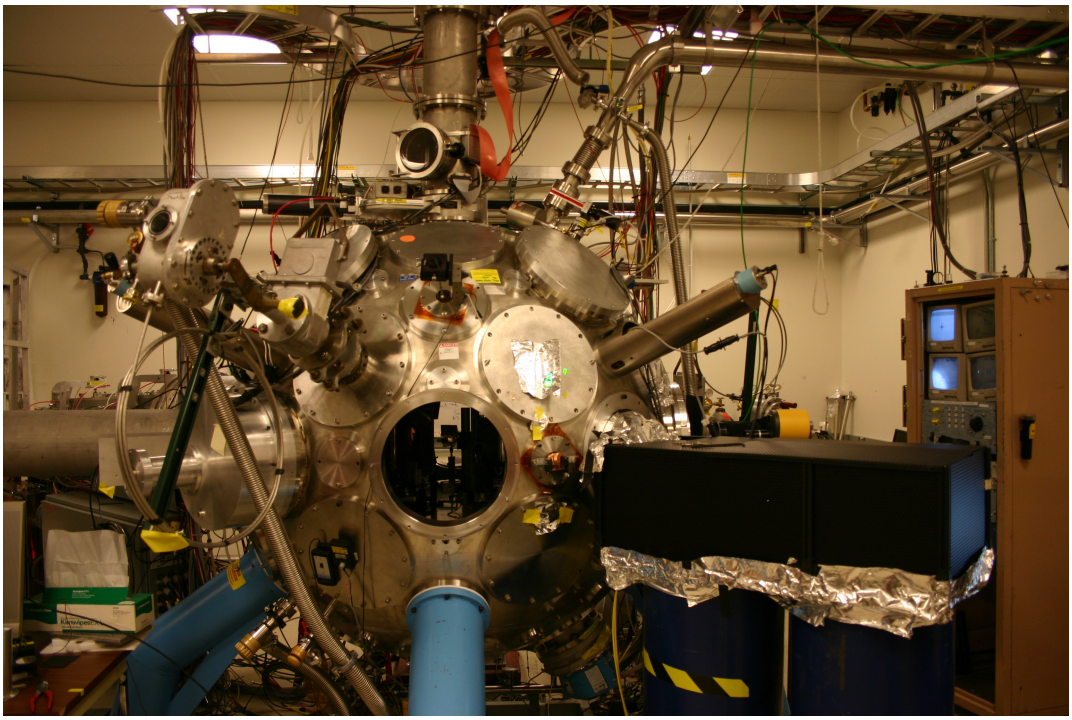

Figure 3.3: Image of the Trident target chamber.

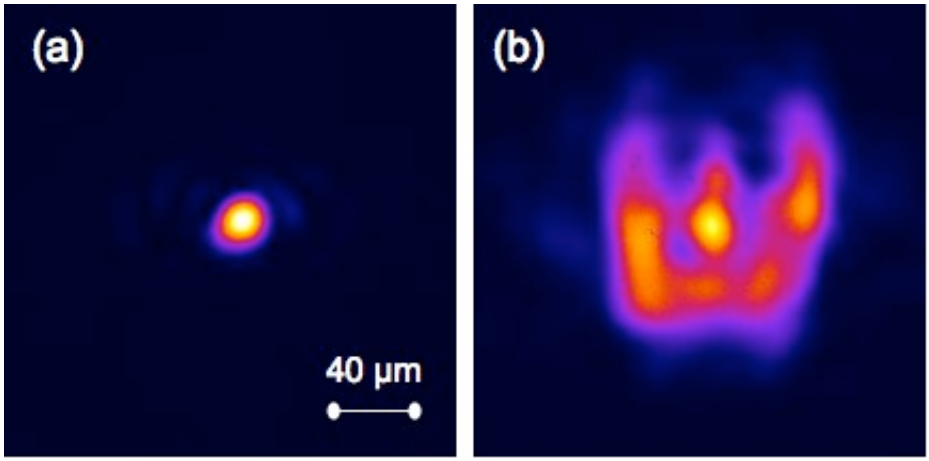

Figure 3.4: Images of the laser focal spot taken with a 12-bit CCD for (a) best focus and (b) the defocused laser spot. The images have the same spatial scale displayed with an arbitrary color scale.

3.2 Trident laser alignment and laser focal spot measurements

The Trident laser spot is aligned and optimized at the start of every day during the experimental campaigns. The target chamber center (TCC) is defined by using two orthogonal viewing cameras and a pointer which is designed to be mounted to any of the chamber ports on the center plane and points to within 100 μm of TCC. Once TCC is defined, the pointer is removed and a wire is placed at TCC. The position of the wire is recorded and the laser focal spot is aligned to this position. The wire is imaged with a microscope magnification lens coupled to a 12-bit CCD (charge coupled device). The CW laser beam is aligned to the wire and the focal spot is optimized by adjusting the parabolic mirror.

To defocus the laser beam on the target, the target was moved up the beam line toward the parabolic mirror. Fig. 3.4 displays the images of the focal spot at best focus and at the defocused position in (a) and (b), respectively. The radius which encompasses 50% of the laser was calculated by first determining the position of the pixel with the maximum signal and then stepping radially outward calculating the ratio of the energy contained within the radius to the overall energy

in the image. In Fig. 3.5, the fraction contained within the encircled area versus radius is presented for laser spot at best focus (a) and at the defocused laser position (b). It is seen in Fig. 3.5 that the radius which encompasses 50% of the laser energy is 12.5 μm for best focus and 45 μm for the defocused laser spot. Assuming 80 J of laser energy and a laser pulse length of 600 fs, the calculated intensity for the afore mentioned radii is 1.36x10^{19} Wcm^{-2} and 1.05x10^{18} Wcm^{-2} for best focus and the defocused laser spot, respectively. Even though the intensity is 1.05x10^{18} Wcm^{-2} for the defocused laser spot, the beam is not uniform and hot spots can be present in the beam, which is seen in Fig. 3.4 (b). These hot spots can lead to localized areas of higher intensity.

3.3 Radiochromic film (RCF)

In the proton experiments, the main diagnostic used to analyze different characteristics of the proton beam was radiochromic film. Radiochromic film (RCF) is a dosimetry film with an active layer that undergoes a chemical reaction when exposed to ionizing radiation [72]. The chemical reaction forms a blue colored polymer that darkens the film in proportion to the radiation dose. The most common types of radiochromic film are GAFCHROMIC® HD-810, MD-v2-55, and EBT [73]. For the majority of our experimental work, we used the HD-810 film because the active layer is the least sensitive compared to MD-v2-55 and EBT and the overall thickness of the film is much less, which is beneficial when stacking the film (discussed later).

HD-810 is composed of three different layers: a gelatin surface layer that is 0.75 μm thick, an active layer containing the organic polymer that is 6.5 μm thick and a clear transparent polyester that is approximately 97 μm thick [73]. A diagram of the film is seen in Fig. 3.6. The film is manufactured in 8×11 inch sheets. The thickness of the active layer varies by 10% from batch-to-batch [73]. A unique characteristic of the film is that it does not need to be developed and it can be worked with in room light. However, it is sensitive to the exposure of sunlight and x-rays. The film can be digitized using a flatbed scanner or a

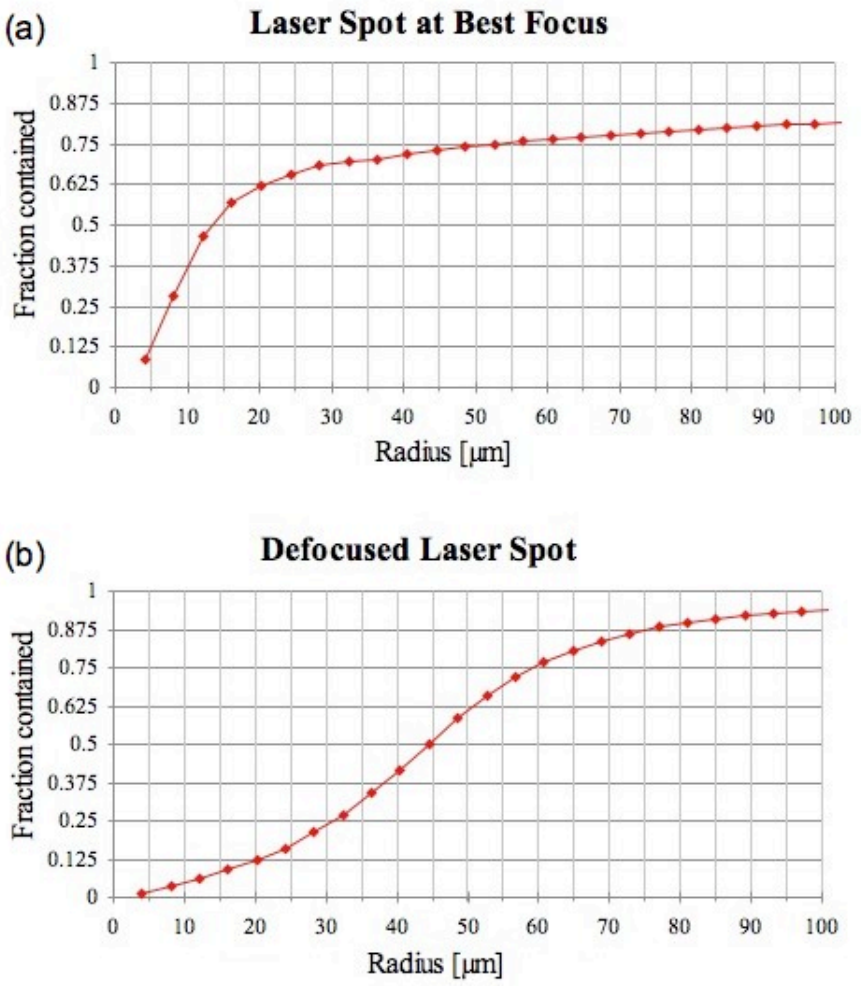

Figure 3.5: Fraction of energy contained within a spot with a specified radius for (a) best focus and (b) the defocused laser spot.

microdensitometer. Therefore, each type of film can be calibrated for a specific scanner using a known source.

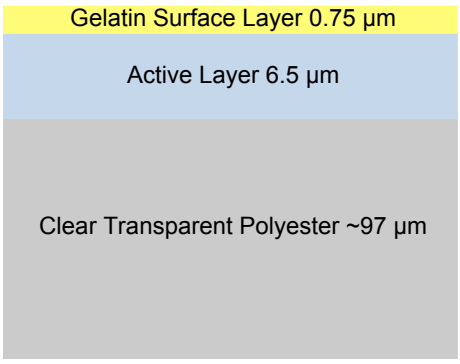

Figure 3.6: Composition of GAFCHROMIC® HD-810 film.

3.3.1 Calibration

The HD-810 film was calibrated using the Isochronous Cyclotron at the Crocker Nuclear Laboratory at the University of California, Davis. The cyclotron can accelerate mono-energetic protons ranging from 1.25-68 MeV with a maximum intensity of 15 μAmps in a 1 cm^2 beam [74]. The main use of the cyclotron is to provide protons for proton therapy to treat cancer of the eye. For the calibration, a single piece of HD-810 film with the gel coating facing the cyclotron was wrapped with 25 μm of Aluminum foil to protect the film from contaminants, which is also done during the experiments.

Using a proton energy of 63.5 MeV, eight different exposures were collected with the film, where the exposure was controlled by fixing the duration of the beam and varying the proton flux on the cyclotron. The total dose absorbed in the active layer of the film is calculated by,

$$Dose = E_{abs} \times \left(\frac{\#\ protons/cm^2}{\rho\tau} \right) \times, \tag{3.1}$$

where E_{abs} is the energy absorbed per proton, ρ is the density of the active layer in the film and τ is the thickness of the active layer. The number of protons

delivered to the film is known from the cyclotron diagnostics. The amount of energy absorbed per proton, E_{abs}, in the active layer is calculated using the stopping powers provided by the program SRIM - The Stopping and Range of Ions in Matter [75], which calculates the stopping range of H ions in different materials. For a 63.5 MeV proton, the energy absorbed in the active layer of the HD-810 is 0.0072769 MeV per proton. For more information on the RCF calibration, refer to references [76] and [77].

The exposed film is used to calibrate an Espon Expression 10000XL flatbed scanner. The scanner can be used for transparencies with the option of saving the images using a 16-bit negative grayscale or a 48-bit RBG color scale. The film was scanned more than 48 hours after the exposure in order for the organic reaction to stabilize. Each of the eight doses on the RCF, seen in Fig. 3.7, is correlated to the pixel reading from the scanner for the calibration. The calibration curve for the

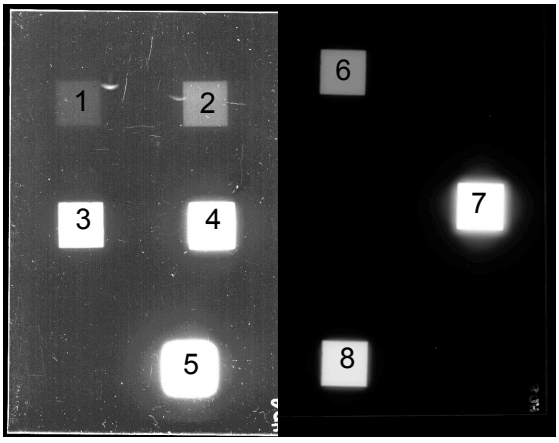

☐	Protons/cm²
1	1.80×10^{09}
2	3.78×10^{09}
3	1.21×10^{10}
4	3.90×10^{10}
5	1.20×10^{11}
6	3.80×10^{11}
7	1.20×10^{12}
8	6.00×10^{12}

Figure 3.7: Two layers of RCF with eight different proton exposures used for the calibration. The chart lists the amount of protons that irradiated the corresponding squares on the film.

HD-810 scanned using the 16-bit grayscale setting is shown in Fig. 3.8, which plots the pixel reading of the scanner with the background subtracted versus the proton dose calculated from the fluence. The functional form of the fit as a function of the pixel value is given by,

$$D_{krads} = a + bx - c\sinh\left(d - ex\right), \tag{3.2}$$

Table 3.1: List of the values for the variables in eq. 3.2.

a	2.285741
b	0.002262
c	0.056811
d	4.323758
e	0.000225

where x is the background subtracted pixel value and D_{krads} is the dose in krads. The fit parameters are listed in Table 3.1. The form of the fit is *a priori* and is found to be the best form to fit the data. Since there is a 10% batch-to-batch

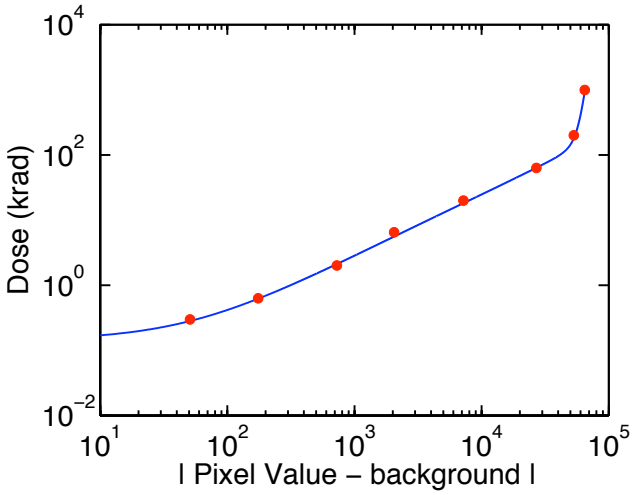

Figure 3.8: Calibration curve for the Espon Expression 10000XL scanner to convert the pixel reading from HD-810 type film into a dose in units of krad. The red dots correspond to the eight dose values from the calibration. The uncertainty in the known dose is 6%, which is smaller than the markers on the graph. The solid blue line is the fit to the data expressed in eq. 3.2

variation in the thickness of the active layer, the derivative of the calibration curve can be used to estimate the error in using the calibration curve with a different batch of film, which is represented by $\frac{\partial D_{krads}}{\partial x}\Delta x$ where Δx is the 10% batch-to-batch variation [76]. The derivative is

$$\frac{\partial D_{krads}}{\partial x} = b + ce\cosh\left(ex - d\right). \tag{3.3}$$

The error is applied to every pixel value converted into dose. For a digitized image, the overall percentage error in the dose is the quadrature sum of each pixel error.

3.3.2 Application

A stack of RCF is used to diagnose different properties of the proton beam. For our experiments, the RCF was used to determine the proton spectrum, laser to proton conversion efficiency, and focusing properties of the generated beam (i.e. focal position and focal spot diameter). Layers of RCF were stacked, alternating with aluminum filters with thickness ranging from 100 μm to 1.5 mm. The composition of a typical RCF pack used in the experiments is displayed in Table 3.2. The whole stack was wrapped with 25 μm of aluminum foil to hold the stack together and to protect the first layer of film from contaminants and direct laser irradiation. A proton beam generated from a thin foil typically has an $f/1$ beam divergence. Therefore, in order to capture the entire beam, the film pack is placed a distance behind the target that is comparable to the size of pack. For example, in the Trident experiments, the film pack contained 4×4 cm^2 pieces of RCF and was placed approximately 4 cm behind the target in the direction normal to its surface..

3.3.3 Proton spectra and conversion efficiency

Since protons deposit the majority of their energy within a particular range (i.e. Bragg Peak), a small range of proton energies will then be responsible for the majority of the dose absorbed in each layer of RCF. Within the pack, each layer of RCF can be associated with a particular band of proton energies, which is used to recreate the proton spectrum. The stopping powers provided by SRIM [75] are used to calculate the energy loss of a range of proton energies through the composition of the RCF pack.

A response matrix is created for the film pack in order to back out the proton spectrum from the layers of RCF. Using a program written in MATLAB®, a response matrix for an energy vector spanning an applicable range of proton

Table 3.2: Composition of a typical RCF pack used in the experiment. The first column lists the layer material with its thickness listed in the second column. The proton energy responsible for the majority of the dose deposited in the layer of RCF is found in the third column.

Material	Thickness (mm)	E (MeV)	Distanct in pack (mm)	Layer
Kapton	0.09			
Al 25	0.025			
HD	0.108	3.2	0.115	A
HD	0.108	4.5	0.223	B
HD	0.108	5.55	0.331	C
HD	0.108	6.45	0.439	D
HD	0.108	7.3	0.547	E
Al 100	0.1			
HD	0.108	9	0.755	F
HD	0.108	9.65	0.863	G
Al 100	0.1			
HD	0.108	11.1	1.071	H
Al 100	0.1			
HD	0.108	12.45	1.279	I
Al 100	0.1			
HD	0.108	13.65	1.487	J
Al 100	0.1			
HD	0.108	14.8	1.695	K
Al 250	0.25			
HD	0.108	16.8	2.053	L
Al 500	0.5			
HD	0.108	20	2.661	M
Al 1500	1.6			
EBT	0.2	27.55	4.369	N
Al 1500	1.6			
EBT	0.2	33.75	6.169	O
Al 1500	1.6			
EBT	0.2	39.2	7.969	P

Table 3.3: Structure of the response matrix created. The first column represents the energy vector. It is the particular proton energy that is incident on the pack. Each column afterward represents each active layer in the stacked pieces of film. The elements in the matrix correspond to how much energy is deposited in that particular layer of film by the incident proton.

Proton Energy (MeV) incident on the RCF pack	Amount of energy (MeV) deposited by the incident proton on the 1st layer of film	Amount of energy (MeV) deposited by the incident proton on the 2nd layer of film	Amount of energy (MeV) deposited by the incident proton on the 3rd layer of film	⋯
6 MeV	0.059512 MeV	0.075292 MeV	0.12627 MeV	…
6.05 MeV	0.058916 MeV	0.074046 MeV	0.12014 MeV	…
6.1 MeV	0.058335 MeV	0.072862 MeV	0.11011 MeV	⋯
⋮	⋮	⋮	⋮	⋱

energies (i.e. 1 MeV - 40 MeV at intervals of 0.05 MeV) is created. The composition of the film pack is broken down into the layers along with the different components that make up a piece of film. For each energy in the energy vector, the amount of energy lost in each active layer of each piece of film is recorded. Table 3.3 describes a typical response matrix for a stack of RCF. The energy absorption curves corresponding to the response matrix are shown in Fig. 3.9 where each line corresponds to a different layer in the stack (i.e. different column in the response matrix). The minimum proton energy that reaches each layer of film, which is responsible for the majority of the dose absorbed within that layer, is determined from the response matrix. The minimum proton energy is seen in the third column of Table 3.2.

To calculate the proton spectrum, each layer of RCF needs to be digitized and converted into dose along with the calculation of the corresponding error. From the calibration curve, each pixel in the digitized image is converted into a dose in units of krads. The following equation is used to convert the dose from krad into deposited energy in MeV

$$Dose_{MeV} = A\rho\tau D_{krad}, \tag{3.4}$$

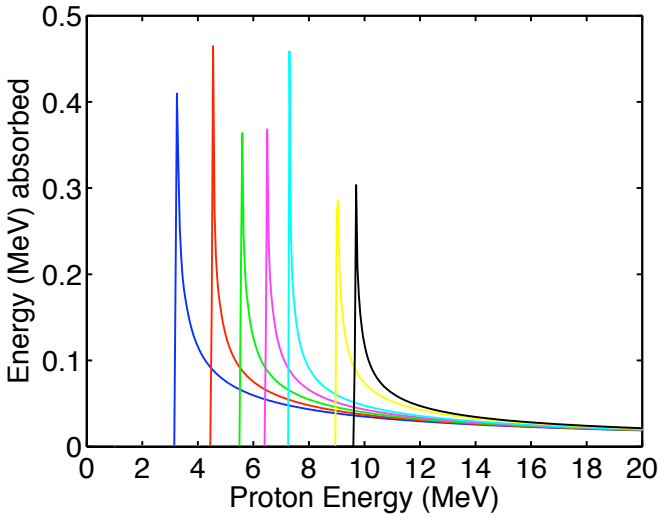

Figure 3.9: Energy absorption curves for the first seven layers of film in the pack listed in Table 3.2. Each line represents a layer of film. The peak of each curve represents the proton energy that is responsible for the majority of dose absorbed in the film.

where A is the area of each pixel and ρ and τ are the density and thickness of the RCF, respectively. The summation over every pixel in the image provides the total dose absorbed in the layer layer.

Fig. 3.10 is an example of the calculated proton dose for a proton beam generated from a hemispherical target. The calculated dose is fitted to a two-temperature distribution function [31]

$$\frac{dN}{dE} = \frac{n_1}{\sqrt{\pi T_1 E}} e^{-E/T_1} + \frac{n_2}{\sqrt{\pi T_2 E}} e^{-E/T_2}, \tag{3.5}$$

which gives the number of protons absorbed per given proton energy, where E is the energy vector used to construct the response matrix and n_1, T_1, n_2, and T_2 are free parameters. The form of the distribution function is taken from eq. 2.97. The dose for each layer, C_i, given by the distribution function is represented by

$$C_i = \sum \frac{dN}{dE} response_i dE, \tag{3.6}$$

where $response_i$ is the column vector from the response matrix corresponding to the i^{th} layer of film and the summation is over all energies in the energy vector.

The dose calculated from the two-temperature distribution is compared to the measured dose.

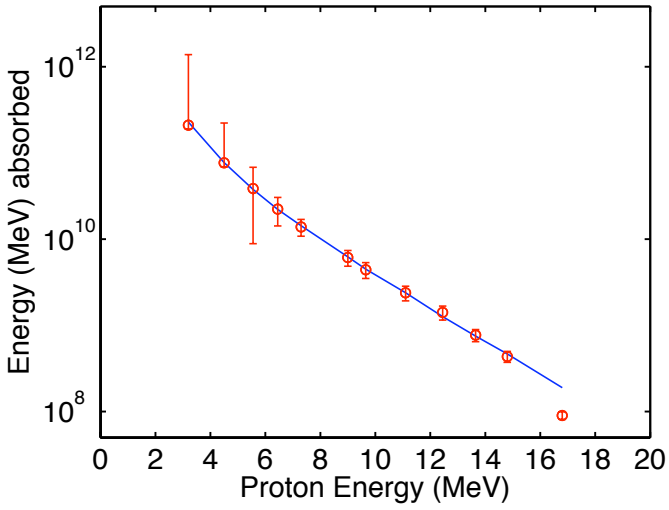

Figure 3.10: Proton spectrum from a hemispherical target. Red dots are the measured dose with the associated error. The blue line is the calculated fit to the data using eq. 3.5.

In some shots there is a mesh placed in the beam path, the shadow which is present in the image on the RCF. The presence of the mesh is taken into account by generating an additional response matrix that includes an extra component for the mesh, which is usually made from Cu and has a thickness of 20 μm. Therefore, the calculated dose is the addition of the two response functions, C_{Mesh_i} and C_{NoMesh_i}, weighted by the area fractions of the beam which interacted with or transmitted through the mesh (determined by the mesh transmission). For a typical shot on the Trident experiment, a 200 line per inch (lpi) mesh was used resulting in a calculated dose of $C_i = 0.5376 C_{Mesh_i} + 0.4624 C_{NoMesh_i}$. To achieve a best fit, the four free parameters in eq. 3.5 are varied to minimize χ^2 represented by

$$\chi^2 = \frac{1}{\#\ layers - \#\ parameters - 1} \sum \left(\frac{C_i - Dose_i}{Dose_i \times error_i} \right)^2 . \qquad (3.7)$$

Once a fit is achieved, the total amount of energy contained in the proton beam is calculated by integrating dN/dE over the range of proton energies of interest. For

the Trident experiments, the spectra are integrated from 4 MeV or 6 MeV to the maximum proton energy seen in the RCF layers. Layers in the film pack relating to energies below 4 MeV are usually saturated or contain contaminants from other ions that are accelerated from the target. The laser to proton conversion efficiency is equal to the total proton energy calculated in the beam divided by the laser energy of the particular shot being analyzed.

The error in the laser to proton conversion efficiency is determined by statistical analysis. When fitting the distribution function, eq. 3.5, to the data, there is a range of values for each free parameter that can achieve a good fit. A matrix is created containing each combination of the four free parameters that provides a good fit, where χ^2 is usually less than 1. For each combination in the matrix, the total energy in the proton beam is calculated. The different fits give a range in the calculated total energy, which is used to determine the error on the conversion efficiency.

3.3.4 Ray-tracing to determine focusing characteristics

Since a generated proton beam is highly laminar, when a proton beam passes through an object placed downstream, the object leaves a shadow imprint in the beam, which is visible on the RCF. In the Trident experiments, a copper mesh (usually 200 lines per inch) was placed a distance, D_{mesh}, from the laser interaction point on the target, which is the front surface of a flat foil or the apex of a hemispherical shell. A stack of RCF is placed a distance, D_{RCF}, further downstream behind the mesh, also measured in relation to the laser interaction point. The stack of RCF contained 4 cm $\times$ 4 cm squares of film alternated with aluminum filters (100 μm - 1.5 mm thick) and was placed $D_{RCF} = 4$ cm $\pm$ 500 μm behind target normal. A schematic of the experimental setup is seen in Fig. 3.11.

Fig. 3.12 shows a typical image of a mesh recorded on a layer of RCF with a proton beam generated from a hemisphere with a diameter of 600 μm. The layer of RCF corresponds to the proton energy of 14.8 MeV. A three-dimensional (3D) ray-tracing technique was developed to determine the minimum focal spot diameter and focal position of the proton beam. In the 3D ray-tracing technique, straight-

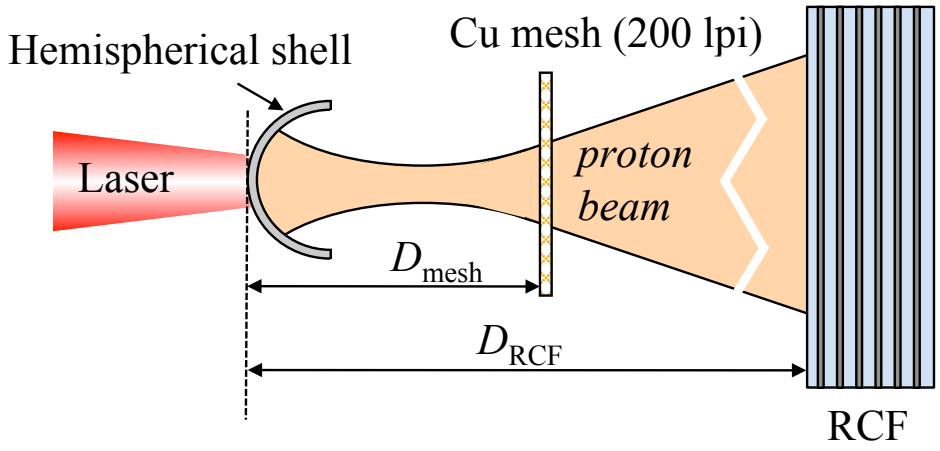

Figure 3.11: Schematic of the experimental setup.

line proton trajectories were reconstructed by connecting the mesh intersection points on the RCF to the intersection points on the original mesh placed in the beam path. For the technique, the following distances need to be accurately known: the distance from the apex of the hemispherical target to the mesh (D_{mesh} in Fig. 3.11) and from the apex to the layer of RCF in the stack being analyzed (D_{RCF} plus the layer depth). Each layer of RCF is analyzed independently because each layer has information pertaining to a different proton energy as previously discussed.

Each mesh intersection point seen on the RCF is identified and related to a mesh intersection point on the original mesh. By adjusting the viewing and color scales on the RCF and by rotating the image, the mesh intersection points are identified within a certain pixel error. This process is done through a MATLAB® graphical user interface. The selection of the mesh intersection points on the RCF is seen in Fig. 3.13, which is a screen shot of the MATLAB® program. With a scanner setting of 500 lines per inch, each pixel on the image is 50.8 μm square. The mesh intersection points were determined within a 25% error of the bar width on the RCF image corresponding to a 10 μm error in the actual mesh. After each point is selected on the RCF, a corresponding point is selected on a representation of the actual mesh. A few points are numbered in Fig. 3.13 to see

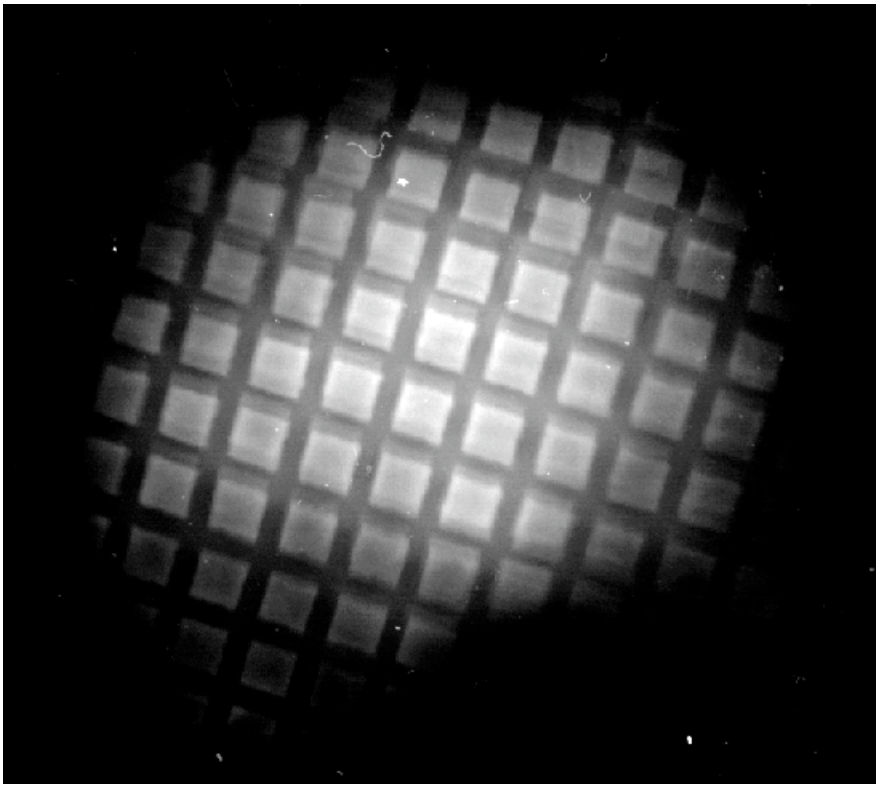

Figure 3.12: Layer of RCF corresponding to the proton energy of 14.8 MeV imaging a mesh placed within the path of the proton beam generated from a 600 μm diameter hemisphere.

the point-to-point relationship.

For the mesh elements, a central optical axis in not defined. Instead each point is defined in relation to the set. The distance between the selected points in the RCF image was converted to microns by knowing the RCF pixel size. A line equation in three dimensions is calculated by using the set of coordinates defined by the point on the RCF, the corresponding point on the original mesh and the distance between the two along the z-axis. A ray (line equation) is calculated for each set of coordinates, reconstructing the generated proton beam. The reconstruction of the proton beam for 14.8 MeV protons is seen in Fig. 3.14a. In the figure, the blue lines represent the calculated rays and the squares represent the RCF layer and the mesh. Fig. 3.14b is a zoomed in view to see the focal region.

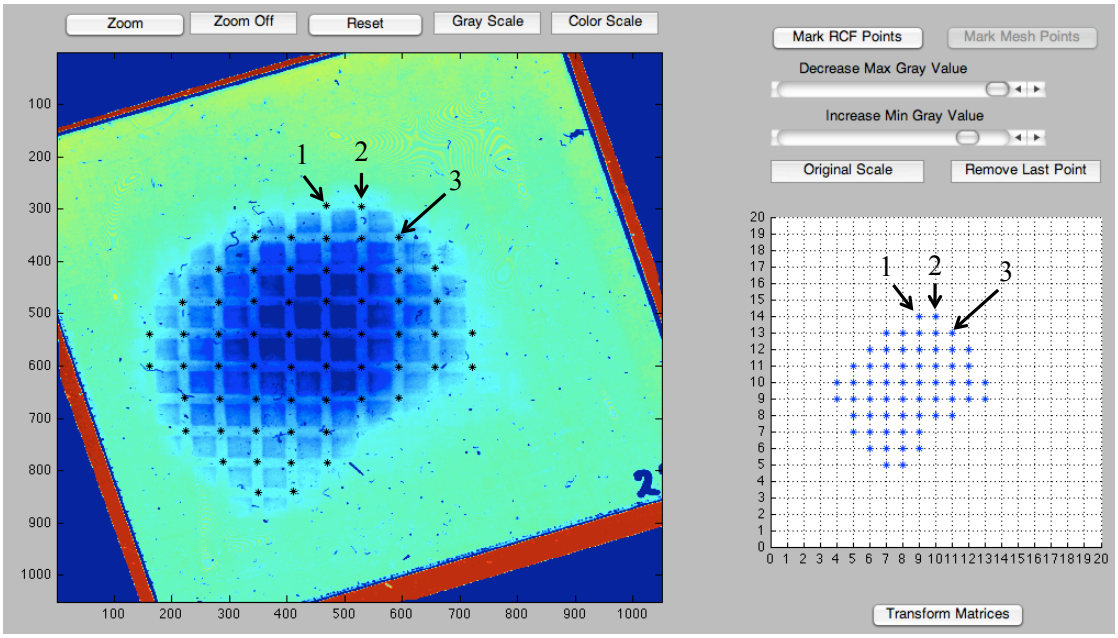

Figure 3.13: A screen shot of the MATLAB® program used to select the mesh intersection points. The RCF layer is the image on the left side of the screen shot. The corresponding mesh intersection points are on the right side.

3.3.4.1 Calculation of focal diameter

The resulting ray bundle is used to determine the minimum focal diameter, D_{80}, and minimum focal position. The calculation of D_{80} is dependent on accurately choosing the mesh intersection points on the RCF and adequately representing the whole proton beam by the selection of the points. The D_{80} diameter, which is the diameter that encompassing 80% of the rays, is determined with a bootstrap method. At a given plane along the longitudinal direction (z-axis), the 3D ray-tracing technique provides the position of N rays (where N is the number of chosen mesh intersections on the RCF film) along with their uncertainties when selecting the points. After assuming that each experimental data point is a realization from a Gaussian probability density function (PDF), an overall empirical probability density function is constructed for each position along the z-axis and the weighted centroid for the PDF is calculated. Fig. 3.15 displays the PDF and weighted centroid for the plane of best focus for a proton beam generated from

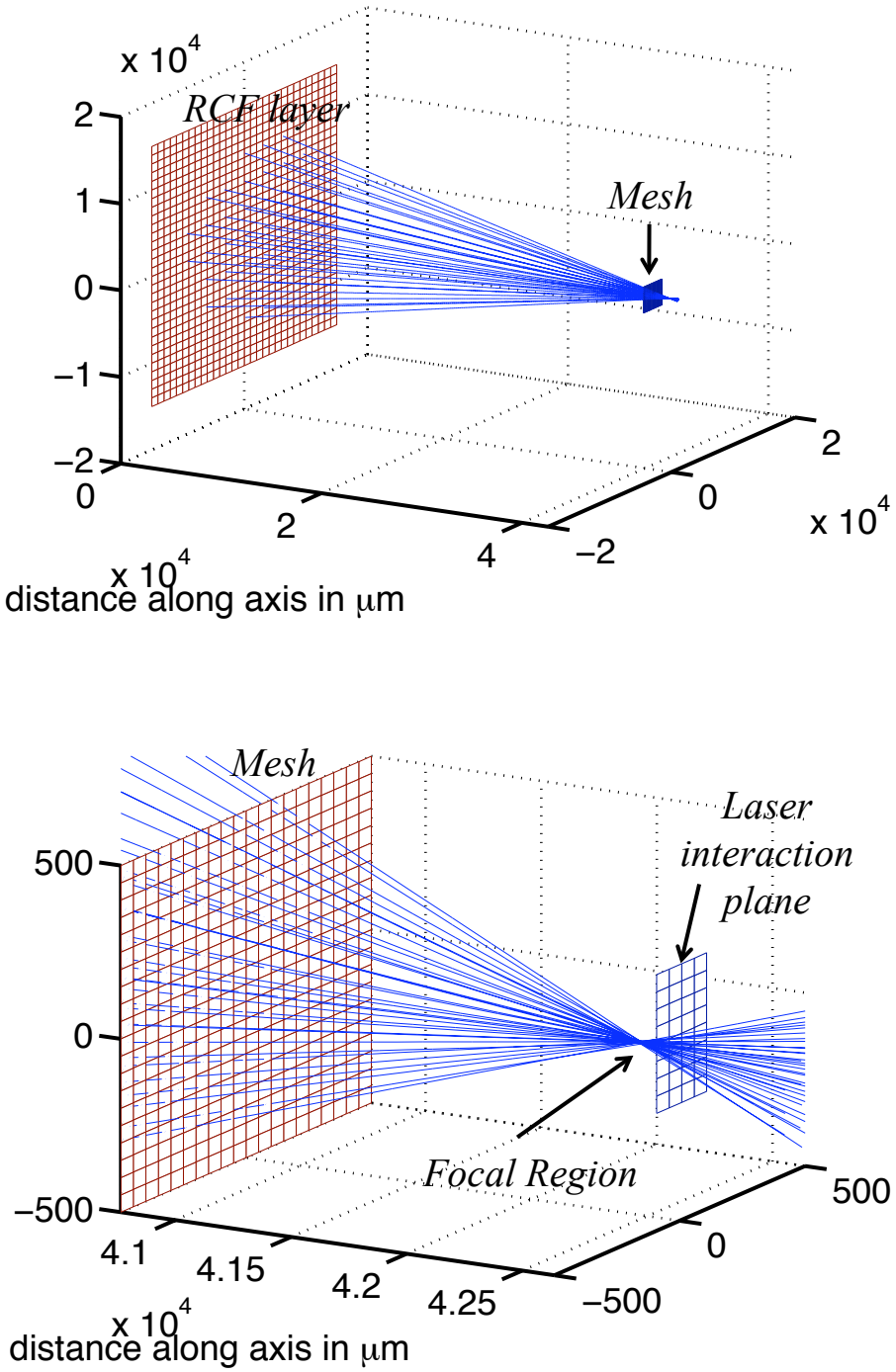

Figure 3.14: (a) Reconstruction of the proton beam using the 3D ray-tracing technique. The z-axis is the distance from the RCF layer. (b) Zoomed in view to see the focal region and the laser interaction plane.

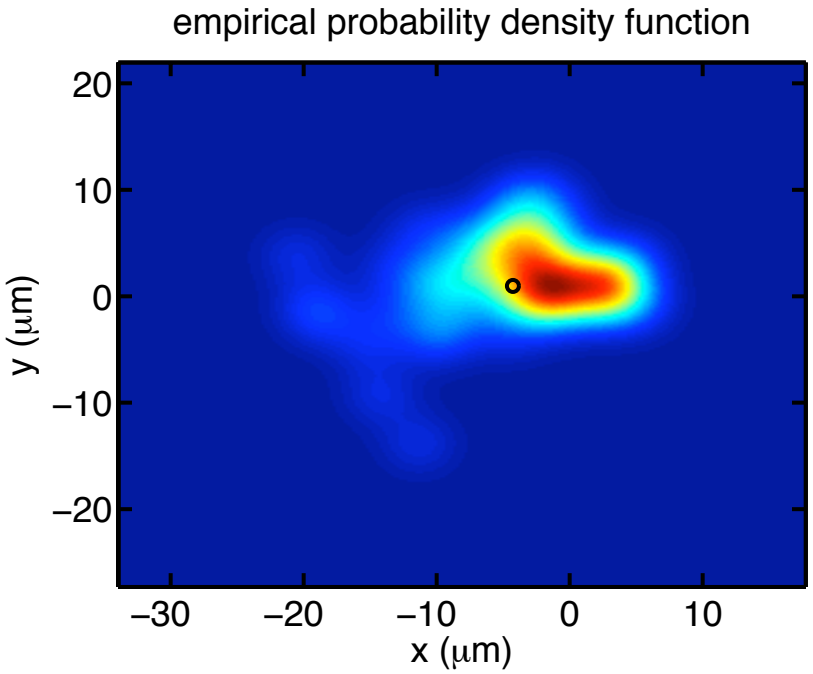

Figure 3.15: Probably distribution function (PDF) for all rays in the plane of best focus. The black circle is the weighted centroid of the PDF.

a 600 μm diameter hemisphere. The cumulative distribution function (CDF) for each data point is then calculated with respect to the weighted centroid. The CDFs for each data point is shown in Fig. 3.16. A Monte Carlo sampling without replacement is then applied: N samples are randomly chosen from the CDF, making sure that exactly one data point is chosen in the uncertainty region that surrounds each experimental data point. This sampling is then repeated over k realizations, where $k > 10^4$. A histogram displaying the sampling of R_{80} ($=D_{80}/2$) is seen in Fig. 3.17. A distribution function for D_{80} is obtained with a determination at the 95% confidence level. Fig. 3.18 shows the calculated D_{80} as a function of position for 14.8 MeV protons generated from a 600 μm hemisphere. The line in Fig. 3.18 is drawn through the D_{80} data points calculated along the z-axis at intervals of 5 μm. A distribution can be constructed for each layer of film in the film pack where the entire beam on the RCF layer can be represented by the selection of mesh intersection points.

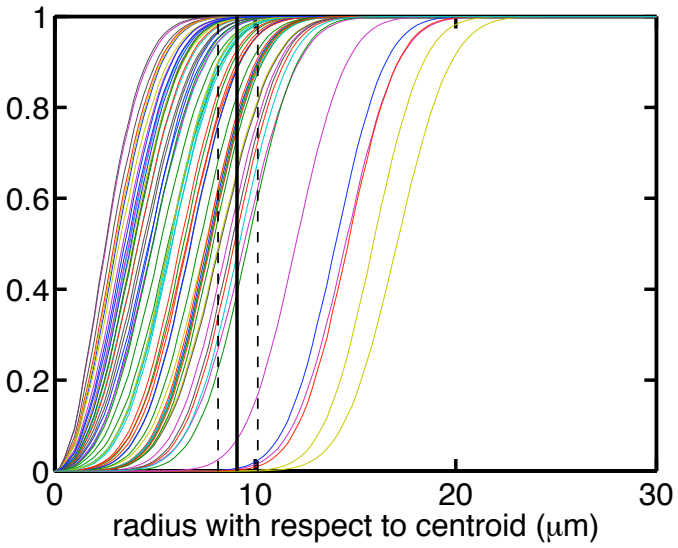

Figure 3.16: Cumulative distribution function (CDF) for each data point represented by the colored lines. D_{80} was determined by random sampling and using the inverse of the CDFs . The black line represents the R_{80} at the plane of best focus with the dotted lines illustrating the 95% confidence level.

3.3.4.2 Calculation of focal position

The focal position was calculated using the measured mesh magnification on the RCF and geometrical considerations. To calculate the mesh magnification for the i^{th} layer of film, M_i, the distance between the mesh intersection points on the RCF were measured and divided by the actual mesh size and the average was taken. The error in the magnification is the standard deviation of the measurement and represented by ΔM_i. The number of mesh intersection points selected varies from shot to shot and the RCF layer of interest, ranging from 10 to 80. The focal position is calculated for each layer of RCF by

$$X_{focal\ position_i} = \frac{M_i \times D_{Mesh_i} - D_{RCF_i}}{M_i - 1} \tag{3.8}$$

where D_{RCF_i} is D_{RCF} plus the depth of the layer in the film pack. The overall error in the focal position takes into account the error in the measured distances in the target set-up, seen in Fig. 3.11, along with the standard deviation in determining the mesh magnification. The overall error is determined by the propagation of

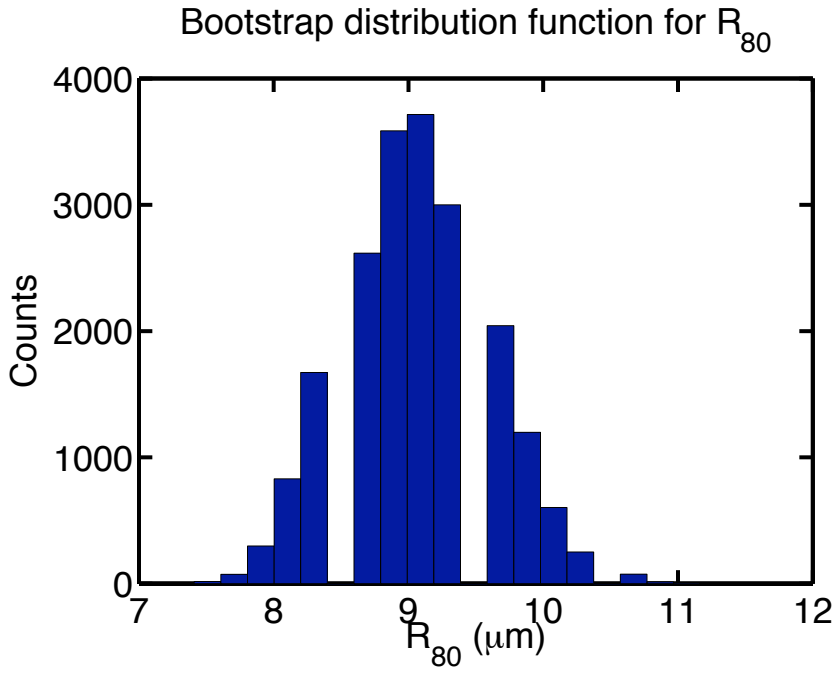

Figure 3.17: Histogram of the random sampling of R_{80} for the CDFs. A distribution function will be fitted to the histogram.

errors, which is expressed by

$$\Delta X_{focal\ position} = \frac{1}{M-1}\sqrt{(M \times \Delta D_{Mesh})^2 + \Delta D_{RCF}^2 + \left(\frac{D_{RCF} - D_{Mesh}}{M-1}\right)^2 \times (\Delta M)^2}. \tag{3.9}$$

Using the mesh magnification and geometrical considerations, the focal position of lower energy protons can be calculated even when mesh elements in sections of the image may not be easily distinguished due to distortions (i.e. blurring of mesh elements and double patterns), which will be discussed in the following chapters. The calculated focal position using either ray-tracing or geometrical considerations agree with one another within the calculated error.

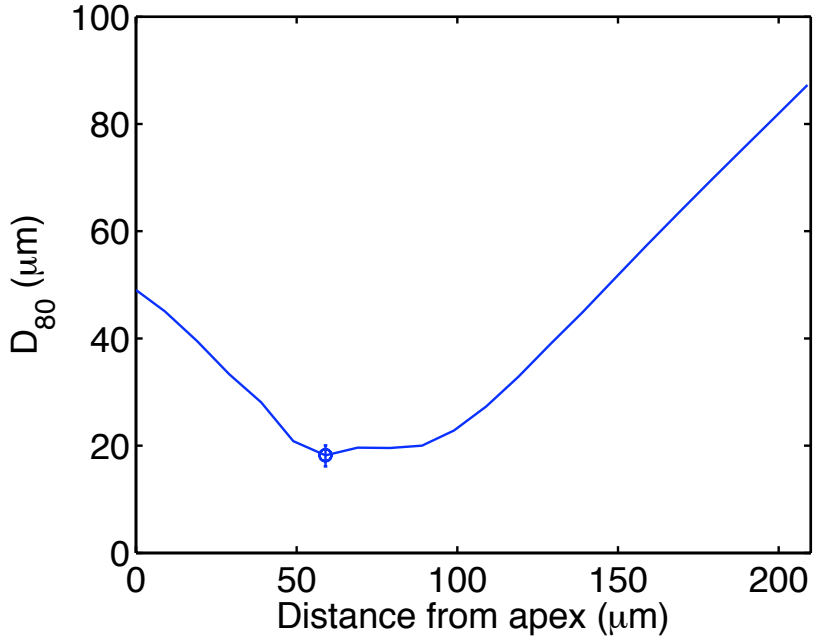

Figure 3.18: D_{80} vs. position for 14.8 MeV protons generated from a 600 μm diameter hemisphere. The blue marker indicates the diameter of best focus with the error representing the 95% confidence level.

3.4 Description of large-scale-plasma (LSP) simulations

To better understand the experimental results presented in Chapter 4, particle-in-cell (PIC) large-scale-plasma (LSP) simulations were performed. The simulations were performed to further investigate the expansion of the proton beam generated from flat foils and the focusing properties using the hemispherical shells. The simulations also allowed us to investigate the trajectories of the proton beam using probe (test) particles and to study the evolution of the generated proton beam as it propagates through the surrounding structure. A description of the LSP code is presented in this chapter along with the simulation results.

The generated proton beam from flat foils and hemispherical shells was simulated using the hybrid particle-in-cell code LSP (large-scale-plasma) [78]. LSP is a hybrid particle-in-cell (PIC) code used to simulate the generation and focusing

of the proton beam in the various experimental geometries. The code uses a hybrid implicit algorithm to incorporate the high plasma densities seen in the experiments. In the direct implicit algorithm that is used, the time limitations placed on the simulations are greatly relaxed because the cyclotron and plasma frequencies do not need to be resolved at every time step as in the explicit approach. The particle momentum advances in the simulation by using half of the electric field at the old position and time and half at the new position and time, which is calculated by correction terms determined by perturbation analysis (detailed information can be found in Ref. [78]).

LSP also adds an inertial fluid description allowing particles to be treated as fluid particles or kinetic particles. The addition of the inertial fluid description eliminates numerical cooling in the simulation, which is present in a purely kinetic case [79]. This allows for the high-density background (for example a solid target) to be treated as a fluid and the accelerated hot electrons and protons to be treated kinetically. A particle that is initially a fluid particle can become kinetic when the directed energy of the particle, $\frac{1}{2}m_e v_e^2$, is much greater than the particle's internal energy, $\frac{3}{2}kT_e$. Summing the particle currents conserves the charge of the particles in the simulation.

2D cylindrical symmetry was assumed for the flat foil and hemispherical shell simulations presented in this chapter. The laser interaction package was not implemented in the version of the code that was used to perform these simulations. Therefore, relativistic electrons are converted from cold background electrons in the target (excitation), simulating the generation of hot electrons from an intense laser interaction with a solid. The electron source has a spatial Gaussian width consistent with the laser spot diameter (~ 90 μm for the hemispherical targets and ~ 25 μm for the flat foils) and its duration matches the laser pulse length of 0.5 ps. The electrons are directed into the target with a relativistic Jüttner distribution with an electron temperature, T_e and a forward drift of $\gamma\beta_z$. The forward drift gives the electrons a transverse momentum allowing the electrons to spread out in a forward half angle when propagating through the target. T_e and $\gamma\beta_z$ are varied in order to make the resultant proton spectrum in the simulation to be

consistent with the proton spectrum and maximum proton energy observed in the experiment. The particular values used for the two parameters will be discussed in the results section for each type of target.

Chapter 4

Proton Focusing and Conversion Efficiency with Flat Foil Targets

Experiments were conducted on the Trident laser at Los Alamos National Laboratory to investigate the two fundamental issues for proton fast ignition (FI): proton jet focusing [20] and laser to proton conversion efficiency [19]. It has been demonstrated that protons have a virtual focus with flat foil targets [1], which has been the conventional understanding. We first performed an experiment using flat foils to investigate the generated proton beam and to determine the position of the virtual source of the proton beam [1]. These results would aid in the understanding of the focusing characteristics of a proton beam generated from a hemispherical shell target, which is presented in the next chapter.

4.1 Experimental Setup

To study the proton expansion, flat foils made from high-density carbon by the process of chemical vapor deposition (CVD), were irradiated by the Trident laser. The flat foils were 21 μm thick, 1.5 mm wide and 3 mm in height. The laser pulse was focused onto the target by an f/8 parabolic mirror. At best focus, the laser focal spot size on target was 25 μm FWHM (full-width-half-maximum) containing 50% of the laser energy. The calculation of the energy contained in the FWHM was discussed in Chapter 3. A 200 lpi Cu mesh was placed downstream of

the foil in the path of the proton beam. The image of the mesh was imprinted into the proton beam and collected using a stack of RCF to study the beam expansion. During the experiment, the flat foils were mounted two different ways, which are displayed in Fig. 4.1. In Fig. 4.1(a), a 21 μm CVD foil is mounted on a Boron

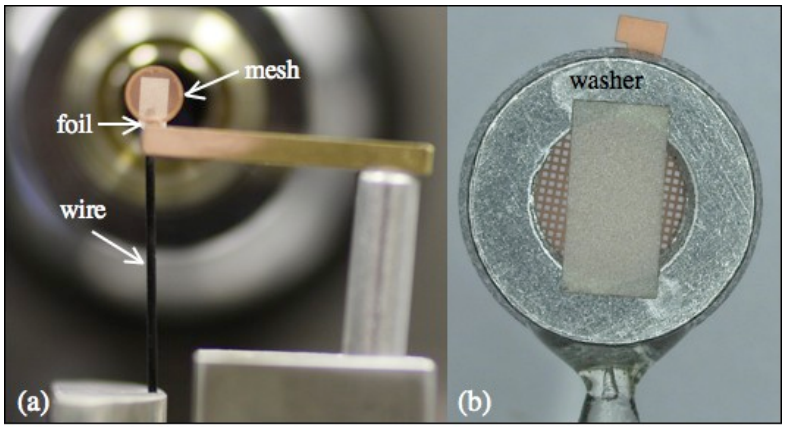

Figure 4.1: Two different mounting techniques for the flat foils: (a) 21 μm CVD foil attached to a Boron wire with the Cu mesh mounted on a second target holder, and (b) 21 μm CVD foil mounted on an Al washer with the mesh mounted on the opposite side in order for the foil and the mesh to be parallel to one another.

wire with the mesh mounted with a separate target holder. Therefore, the foil and the mesh are completely separated from each other. In order for the mesh and the foil to be parallel, the CVD foil was mounted on an Al washer with the mesh directly attached to the reserve side as seen in Fig. 4.1(b). The washer had an inner diameter of 2 mm, an outer diameter of 3 mm and a length of 1.5 mm. The two different mounting techniques were used to determine if the mounting technique could affect the propagation of the proton beam. For each type of mounting technique, the focal position and focal spot size of the generated proton beam from the flat foils were determined using the 3D ray-tracing technique described in Chapter 3. To help understand the results, the shot number, laser parameters, and target characteristics are listed in Table 4.1.

Table 4.1: Flat foil shot parameters.

Shot #	70	24	59
Laser Energy (J)	82	64.5	62.4
Laser Pulselength (fs)	596	553	648
Mounting Type	A	B	B

4.2 Focusing results

The calculated focal position for each of the four targets is displayed in Fig. 4.2. Using the ray-tracing technique, it was calculated that the flat foils do not have a virtual source located on the laser interaction side of the foil (focal position < 0, where 0 is the front surface of the foil). Our results do not agree with previous observations, which were made using a shorter laser pulse of 100 fs even though the peak intensity was $> 10^{20}$ Wcm^{-2} [1] compared to 500 fs and 10^{19} Wcm^{-2} in our experiments. The 21 μm foil mounted separately from the

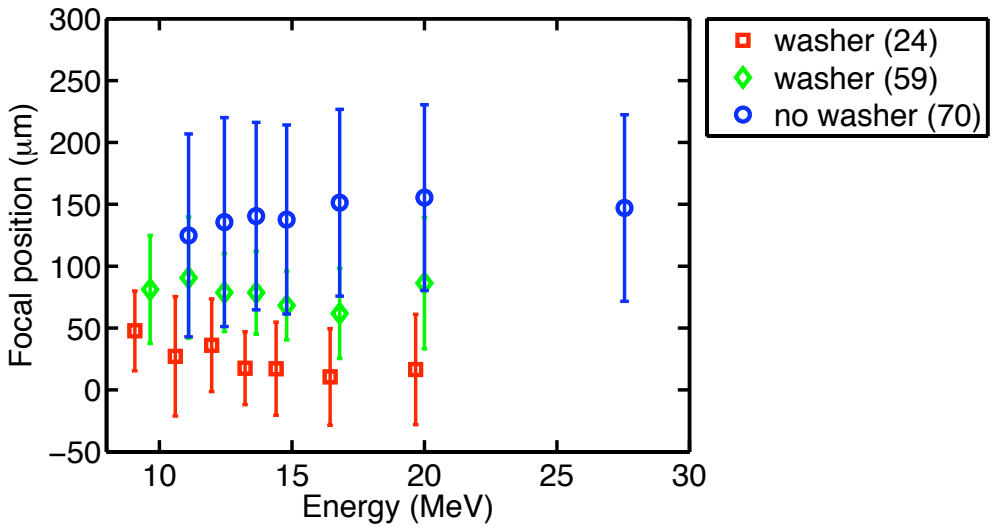

Figure 4.2: Calculated focal position from the ray-tracing technique for each type of target. Regarding the focal position, 0 represents the front surface of the foil and values < 0 are on the laser interaction side of the foil (virtual focus).

mesh exhibits a focal position located the furthest distance away from the rear surface of the foil. The two foils, which were attached to the washer as shown

in Fig. 4.1(b), have a calculated focal position closer to the rear surface of foil than the foil which was mounted on a separate stalk. However, none of the flat foils have a virtual focus. These results from the ray-tracing technique can be explained by investigating the proton expansion and taking into consideration the results from previously published experiments. The understanding of these results and why they differ from previous results are important to future proton beam applications.

In the initial stage of the proton acceleration from the flat foils, the protons are accelerated normal to the surface (Target Normal Sheath Acceleration - TNSA) due to the Debye sheath field set up by the escaping hot electrons from a region on the rear side of the target. A cartoon displaying the development of the bell-like Debye sheath and proton expansion is shown in Fig. 4.3. The remaining hot electrons will recirculate through the target, spreading out transversely. The density of the hot electrons is greatest near the central axis since it is the center of the laser beam where most of the energy is located. As the protons are accelerated by the sheath field away from the rear surface of the target, the Debye sheath moves with the protons, defining the leading edge of the proton expansion. Since a higher density of electrons with higher temperatures which could escape the target reside near the central axis, the rate of expansion near the central axis is greater than the outer regions, causing the Debye sheath to develop a circular bell-like shape. Initially, the protons are stated to be accelerated normal to the surface because the sheath field is located on the surface of the foil. As time progresses and the sheath expands, creating a bell-like shape, the protons are accelerated normal to the leading edge of the sheath as seen in Fig. 4.3. The initially accelerated protons, which are the more energetic protons since they are accelerated for the longest time and hence gain the most energy, will have a small radial velocity component because they originate closer to the central axis and experience a more evenly distributed sheath field. Protons accelerated later in time originate from a larger region on the rear surface of the target due to the transverse spreading of the electrons and experience transverse gradients in the sheath field away from the center axis causing these protons to have a larger radial velocity component.

The expansion of the sheath and the transverse gradient of the sheath field from the central axis are dependent on the energy of the hot electrons accelerating the protons and the duration of the acceleration. Therefore, a proton accelerated later in time will have a larger radial velocity component and a larger divergence angle. When the ray-tracing technique is used to determine the focal position, the larger divergence angle will cause the traced ray to focus at a point further along the central axis in the z-direction as seen in Fig. 4.4 than a proton which has a small radial velocity component.

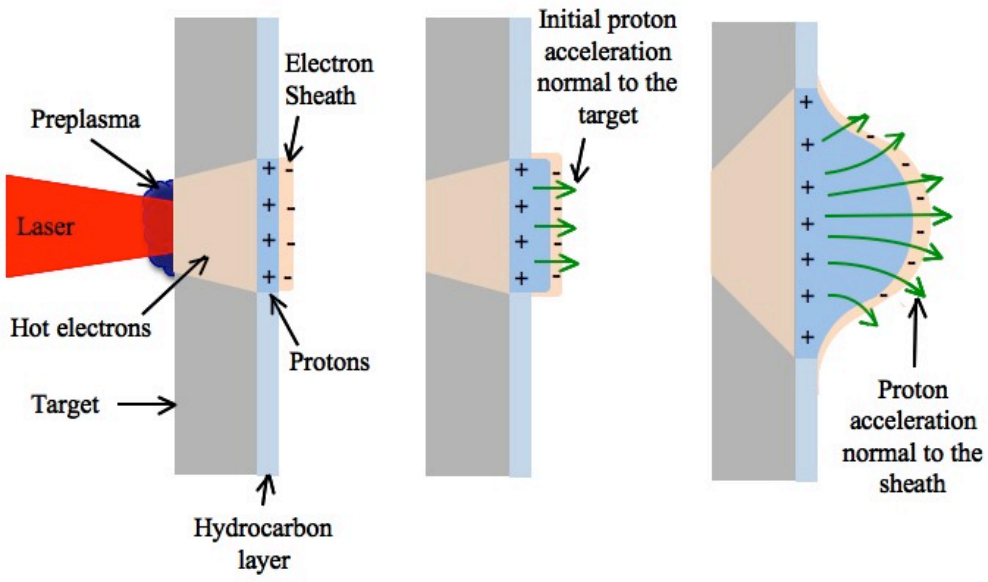

Figure 4.3: Description of the proton expansion from a flat foil.

The increasing divergence of the proton beam, due to a larger gradient, is further explored by looking at how the maximum half angle of the beam changes with time in simulations presented in the next section. This phenomenon would explain the calculation of the real source position from the experimental results.

From the observations made from the experimental results, Bellei *et al.* [80] developed a theoretical explanation for the proton expansion in two dimensions. Previous analytical solutions for plasma expansion into vacuum are one dimensional [49, 81]. Bellei *et al.* considers a two dimensional expansion in r and z, that is cylindrically symmetric [80] . Assuming the speed of sound is the same in all

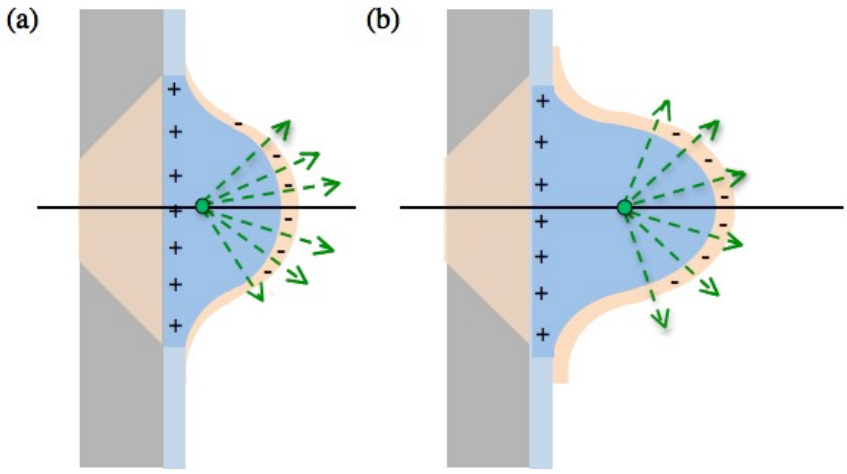

Figure 4.4: Progression of the proton expansion from a flat foil. (a) Proton expansion from a foil target early in the expansion time. (b) Proton expansion from a foil target later in time where the expansion is more bell-like with steeper gradients on the sides compared to (a).

directions, iso-density/pressure/pressure gradient contours can be expressed by

$$K^2 = \frac{r^2(t)}{l_r^2} + \frac{z^2(t)}{l_z^2} \tag{4.1}$$

which is the condition for constant energy where K is a constant related to energy, and l_r and l_z are the characteristic scale-length of the plasma density in the r and z directions, respectively. Along the contours, the angle of emission of a particle can be expressed by

$$tan\alpha = \left(\frac{v_r}{v_z}\right) = \frac{\eta}{\sqrt{1-\eta^2}} \, (0 < \eta < 1) \tag{4.2}$$

where η is the asymptotic kinetic energy in the radial direction gained by an ion and is equal to r_0/Kl_r. When $\eta < 0.5$, there is a linear relationship between the initial radial position of the ion and the asymptotic angle of emission. On the other hand, when $\eta > 0.5$ non-linearities begin to play a role and the angle of emission is increased. For ions where r_0 is further away from the central axis, the angle of emission can be greater than for the ions emitted closer to the central axis. The angle of emission is also larger for lower values of K, which is related to energy. The increased angle of emission is observed in the layers of RCF by the

magnification of the mesh elements increasing radially outward from the center of the film causing a 'pin-cushion' effect. This phenomenon is observed in Fig. 4.5(a). The protons that are emitted at a larger distance from the center are accelerated at a later time and thus gain less energy than the protons emitted closer to the central axis near the beginning of the expansion. The mesh magnification does not vary across the RCF for high energy protons as seen in Fig. 4.5(a). Further analytical solutions, simulations and detials can be found in Ref. [80].

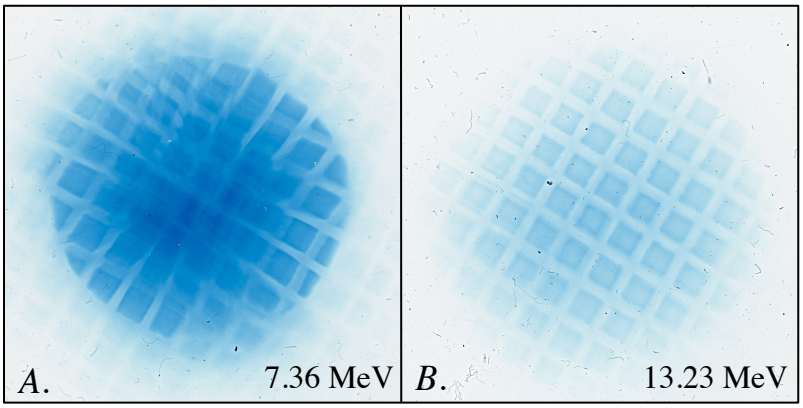

Figure 4.5: Two layers of RCF showing a proton beam from a flat foil mounting on an Al washer with a Cu mesh corresponding to the proton energies of (a) 7.36 MeV and (b) 13.23 MeV.

The decrease in the distance between the foil and the focal position for the two foils mounted with the washers can be described by the physics presented in Ref. [57], which was discussed in section 2.2.2 of Chapter 2. The washer is acting like an electrostatic lens that is collimating the generated proton beam as it passes through the washer. Energetic electrons travel from the target into the washer creating an electric field on the inner walls of the washer that is directed radially inward, collimating the beam. This result was discovered in our following experiment with hemispherical shells, which will be discussed in more detail later in this thesis. Since the proton beam is being collimated by the electric field on the walls of the washer, the natural divergence of the generated proton beam is suppressed. The proton beam begins to radially expand once the beam is no longer affected by the field (i.e., outside of the washer or when the electric field diminishes

along the wall). Therefore, since the overall divergence of the beam is reduced, when a line is traced from the RCF, it would cross the center axis closer to the foil than a line from a naturally diverging proton beam. A slight reduction in the angle of the line with respect to the central axis results in a noticeable difference in position. The effect of the electric field on the proton beam can also add to the 'pin-cushion effect' seen on the RCF in Fig. 4.5(a) for the lower energy protons. The lower energy protons are generated at a larger radial distance from the central axis and are more affected than the more energetic protons since they are closer to the washer and have less longitudinal velocity. The uniformity of the mesh magnification in Fig. 4.5(b) supports the fact that the higher energy protons are less susceptible to the fields on the walls. The effect of a surrounding structure on the propagation of the proton beam is further explained in Chapter 5 when a hemispherical shell target is placed in a surrounding structure.

Even though there is a difference in the focal position for each target as seen in Fig. 4.2, the focal spot size of the proton beam, calculated using the ray-tracing technique, is comparable in each case, which is shown in Fig. 4.6. The technique projects back the shadow of the mesh on the RCF via the original mesh, forming a bundle of converging rays, which is used to determine the minimum D_{80} diameter, defined as the diameter encompassing 80% of the rays. The calculation of D_{80} is dependent on accurately choosing the mesh intersection points on the RCF and adequately representing the whole proton beam by the selection of the points. For the RCF layers corresponding to the lower energy protons, the focal spot size could not be calculated due to the distortions of the mesh image, as seen in Fig. 4.5, which prevented the entire beam to be accurately represented. The presented focal spot size for the flat foils is the source diameter of the proton beam. The source diameter determines the resolution of the object the proton beam is imaging. For all cases the focal spot size of the proton beam increases with decreasing proton energy. This result is caused by the lower energy protons originating from a larger radial distance from the central axis and being accelerated near the wings of the bell shaped curvature of the sheath.

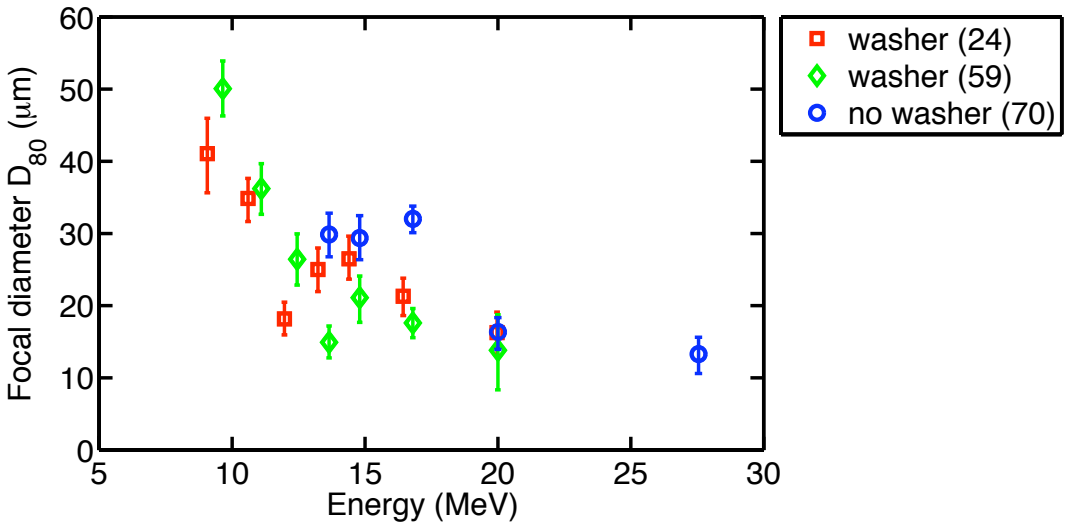

Figure 4.6: Calculated proton focal spot size from the ray-tracing technique.

4.3 Simulations for flat foils

Simulations were performed using the LSP code in Chapter 3 with flat foils to study the expansion physics of the generated proton beam. The pulse length and spatial Gaussian width of the electron source were consistent with the experimental values of 0.5 ps and 25 μm, respectively. The foil in the simulation was 10 μm Au instead of CVD, which was used in the experiment, due to the availability of the simulations. The Au foil had a 300 μm diameter with a 100 nm thick H layer on the rear surface to represent the hydrocarbon layer. A hot electron temperature of T_e= 1 MeV and a foward drift of $\gamma\beta_z$= 1 MeV were used in the simulations. Fig. 4.7 shows the proton distribution for all proton energies at 2 ps in the simulations. The protons that have expanded furthest from the foil (orange) are the highest energy protons. As the proton beam expands, the simulation shows the curving of the proton trajectories and the increased angle of emission represented by the black arrows in Fig. 4.7.

To further investigate the propagation of the beam, Fig. 4.8 displays the proton distribution for energies greater than 10 MeV at a time of 1.5 ps into the simulation. At the 1.5 ps time step, the velocity vectors of the protons in the

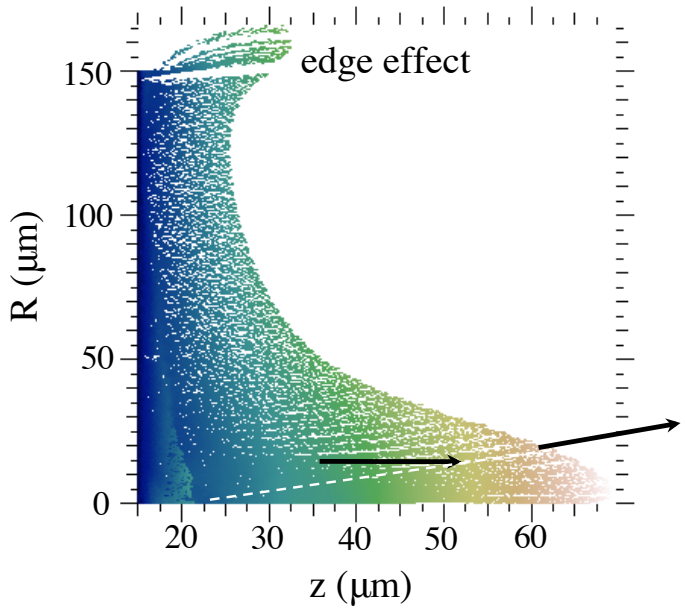

Figure 4.7: Simulated proton distribution for all proton energies at 2 ps. The color gradient represents the gradient of the proton energy in the expansion with the higher energy protons near the leading edge of the expansion (orange) and the lower energy protons near the target surface (blue).

simulation are projected backward, similar to the ray-tracing technique. The focal position is determined by calculating the radius containing 80% of the particles at different positions along the z axis and finding the smallest radius. At 1.5 ps, the projected focal position from the simulation was calculated to be -190 μm (0 is the front surface of the foil), which indicates a virtual source. Fig. 4.8

The focal position of the generated proton beam was also calculated at 2 ps. Fig. 4.9 displays the proton distribution at 2 ps for proton energies greater than 10 MeV. As seen in Fig. 4.9, the proton beam expands further away from the rear surface of the foil compared to Fig. 4.8. The projected focal position was projected to be at -60 μm. As time progresses, the proton beam expands further away from the rear surface of the foil and the projected focal position moves closer to the front surface of the foil.

The difference in the focal position is related to the divergence angle of the proton beam. As the proton beam expands, the transverse gradient on the sides of

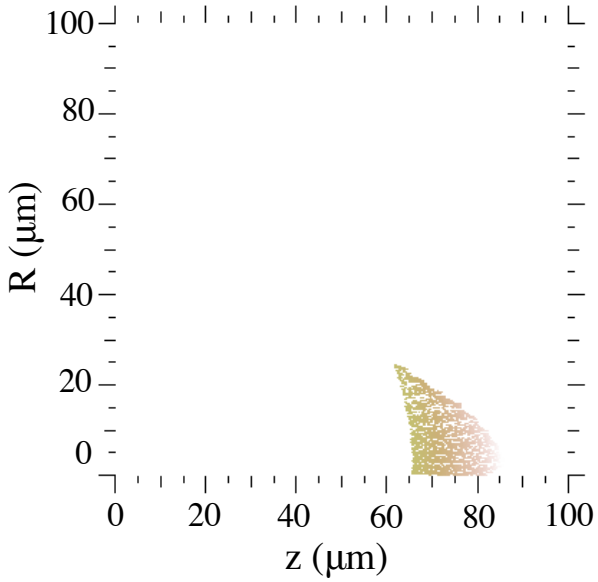

Figure 4.8: Simulated proton distribution for proton energies > 10 MeV at 1.5 ps.

the bell-shaped expansion becomes larger. Since the protons are accelerated normal to the sheath, the divergence angle of the proton increases in time. Fig. 4.10 shows the calculated maximum half angle of the proton beam in the simulation as a function of time. As time progresses, the maximum half angle increases. At 2 ps, the maximum half angle is still increasing meaning that the protons are not yet free-streaming and do not have ballistic trajectories. The calculated focal position will continue to move closer to the foil until the protons become free-streaming. Therefore, it is possible that the calculated focal position may become real (on the rear side of the foil) as observed in the experiment instead of a virtual focus. However, simulation data is not available for times greater than 2 ps to see this effect. Depending on the complexity and resolution of the simulation, running the simulations for a longer amount of time is a challenge. A virtual focus was observed in past experiments [1], which has been the convention, where the laser only irradiated the target for 100 fs. The target was irradiated for 5x longer in our experiments (500 fs) creating a longer and more bell-shaped expansion of the target, which will cause the half angle to increase for a longer amount of time and

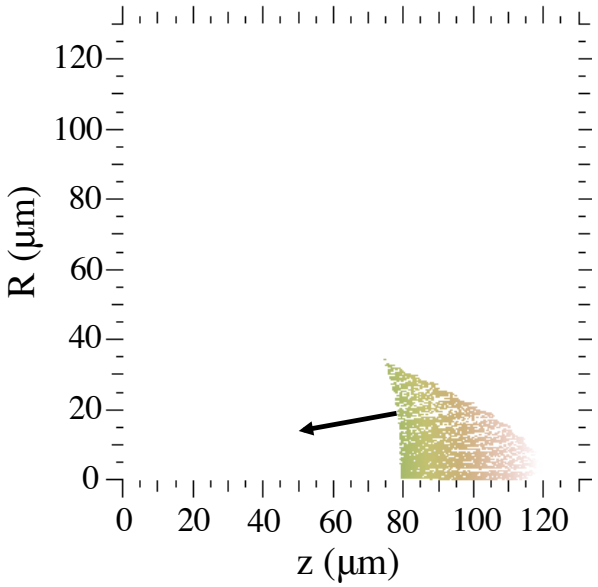

Figure 4.9: Simulated proton distribution for proton energies > 10 MeV at 2 ps.

change the focal position of the beam when ray-tracing is applied.

4.4 Conversion Efficiency

Washers were used in order to mount the foil and the mesh parallel to each other to reduce the error in the measurement between the components for the ray-tracing technique. It was determined from the ray-tracing that the washer affected the propagation of the proton beam, which was apparent with determining the focal position. When mounting the foil with a washer, as seen in Fig. 4.1(b), the washer also decreases the laser to proton conversion efficiency. Fig. 4.11 shows the laser to proton conversion efficiency calculated from proton energies greater than 6 MeV for the 21 μm foils mounted with a washer (Fig. 4.1b) and without (Fig. 4.1a). The conversion efficiency is calculated from 6 MeV instead of the usual 4 MeV because for one shot with the washer (21524 from Table 4.1) the first layer of RCF corresponded to the proton energy of 5 MeV and was saturated. Fig. 4.12 displays the measured experimental dose from the layers of RCF in the film pack for each shot. Each data point represents a layer of RCF. The fits to the

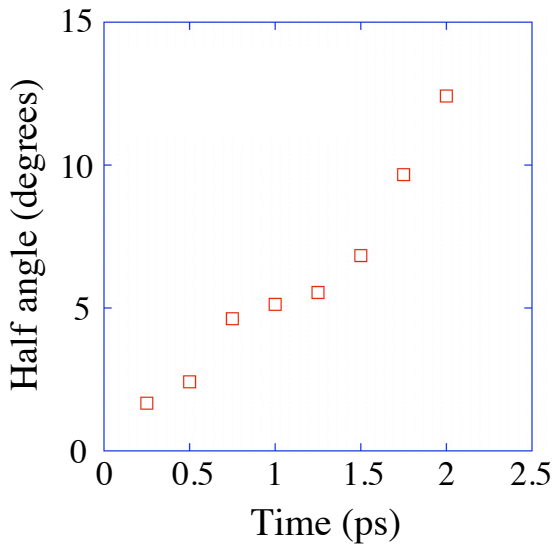

Figure 4.10: Maximum half angle in degrees of the generated proton beam from a flat foil in the simulation as a function of simulation time.

experimental data, $\frac{dN}{dE}$ as described in Chapter 3, are shown in Fig. 4.13 with the error bars representing the range of fits.

The decrease in the laser to proton conversion supports the fact that hot electrons are traversing the flat foil and spreading into the washer. The hot electrons generated from the laser-plasma interaction on the front side of the target lose their energy due to three competing mechanisms: collisional losses to the target and plasma, ohmic heating, and electron cooling through adiabatic expansion of the target (proton and ion acceleration and field generation). The hot electrons transverse the target and spread into the washer. Therefore these electrons are no longer present in the flat foil to accelerate the protons. The hot electrons travel along the inner surface of the washer losing energy through collisions and partitioning their energy to the creation of an electric field on the walls of the washer. This electric field affects the trajectories of the lower energy protons which are accelerated from the foil at a larger radial distance from the center axis. Therefore, the natural divergence of the proton beam is suppressed until the proton beam extends outside of the washer or no longer feels the effect of the electric field. Since the divergence is suppressed, the calculated focal position using the ray technique will

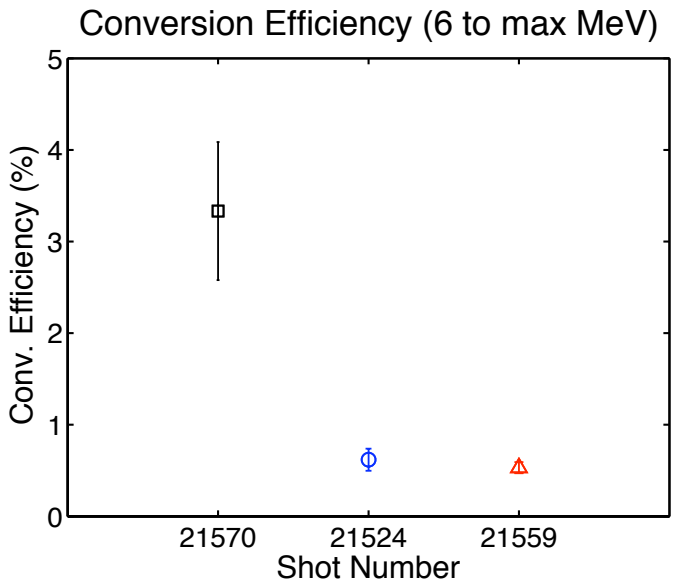

Figure 4.11: Calculated laser to proton conversion efficiency for proton energies greater than 6 MeV. Table 4.1 provides the parameters for the shots listed. Shots 21524 and 21559 are mounted with a washer and shot 21570 is mounted without a washer.

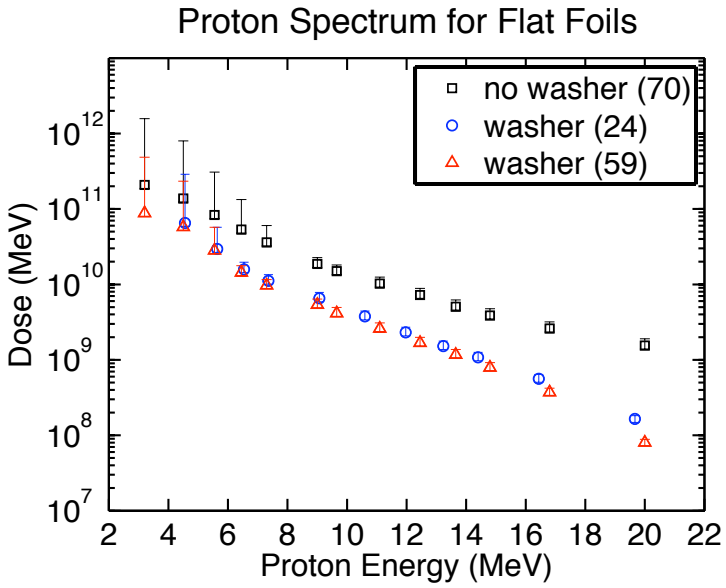

Figure 4.12: Experimentally determined dose in MeV for each layer of RCF for the flat foil targets. For the higher proton energies, the error bars are similar in size to the size of the markers.

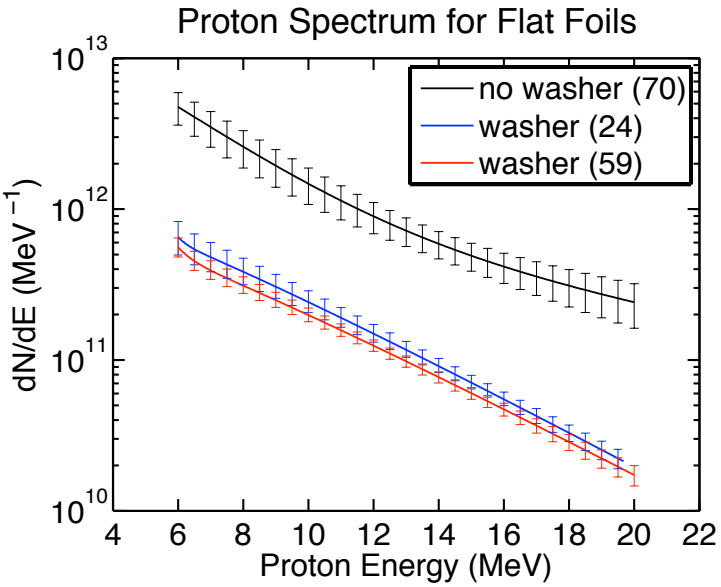

Figure 4.13: Calculated fit spectrum $\frac{dN}{dE}$ for the dose displayed in Fig. 4.12.

be closer to the foil, which is observed in Fig. 4.2. With the washer present, the electron energy being partitioned into the acceleration of the protons is decreased because a portion of the electrons are traveling into the washer and giving their energy to the fields formed on the walls of the washer. The decrease in the proton conversion efficiency supports this statement. The effect is also observed in the experimental proton energy spectrum seen in Fig. 4.12 where the measured dose on corresponding layers of RCF is less for the shots with the washer compared to the shot without the washer. The details of the effect of the washer is further explained in the following chapter when a hemispherical shell target is placed within a surrounding structure. Comparison to simulations was not available due to the fact that the simulations did not run beyond 2 ps. At 2 ps, the proton beam is still expanding as seen by the continuous increase in the maximum half angle in Fig. 4.10 and therefore the protons are still being accelerated from the foil.

4.5 Summary

It has been conventional wisdom that a flat foil target has a virtual focus and protons have ballistic trajectories. However, with longer pulselengths and thus a longer source of electron acceleration, we determined that the proton trajectories may not be truly ballistic until the proton acceleration has ceased. The trajectories of the protons are dependent on the shape of the proton expansion. With a longer source of hot electrons, the expansion of the sheath becomes more bell-shaped creating a large transverse gradient in the Debye sheath measured from the central axis. After the initial expansion of the target, where the acceleration of the protons are normal to the target, the sheath becomes bell-shaped and the protons are accelerated normal to the sheath. Therefore, as the sides of the sheath become steeper with the expansion due to a longer period of hot electron acceleration, the half angle of the proton beam continues to increase as seen in Fig. 4.10. This non-linearity is present on the layers of RCF corresponding to the lower energy protons shown by the radial change in the mesh magnification.

The proton trajectories are also affected by the mounting scheme of the foil. When a foil is mounted to a washer for stability, the washer affects the proton trajectories and the conversion efficiency. The electrons in the foil escape to the washer setting up fields on the inner surface of the washer. These fields affect the trajectories of the protons. The electrons that escape the target decrease the number of electrons available to accelerate the protons, thus decreasing the laser to proton conversion efficiency. The expansion physics of a proton beam from a flat foil and the observation of the mounting scheme affecting the proton conversion efficiency lays a framework for the understanding of a proton beam generated from hemispherical shell targets presented in the following chapter.

Chapter 5

Proton Focusing and Conversion Efficiency with Hemispherical Shell Targets

An understanding of the proton expansion from a flat foil in the previous chapter helps us to study the proton focusing from a hemispherical shell target. Hemispherical shells are envisioned to be used to focus a proton beam, which will deliver energy to a pre-compressed core in cone-guided Fast Ignition targets. As previously mentioned, investigations of proton focusing from curved surfaces are relatively scarce. Proton jet focusing was first demonstrated using hemispherical shells by Patel *et al.* [20] and was further explored to determine the optimal position of the focus at a distance of $1.7R$ from the apex of the hemispherical shell, where R is the radius of curvature [2]. We performed an experiment to determine the focal spot diameter and focal position of the generated proton beam from a hemispherical shell target. We demonstrated that focusing of the proton beam is highly dependent on the evolution of the electrostatic sheath contrary to earlier assumptions that protons have ballistic trajectories. In addition, we performed the first investigation of the generation and focusing of a proton beam in a FI geometry, where the beam propagates and focuses through an enclosed cone structure, similar to that envisioned for FI targets. Along with the focal characteristics, we investigated the effect of the surrounding structure on the laser to proton conver-

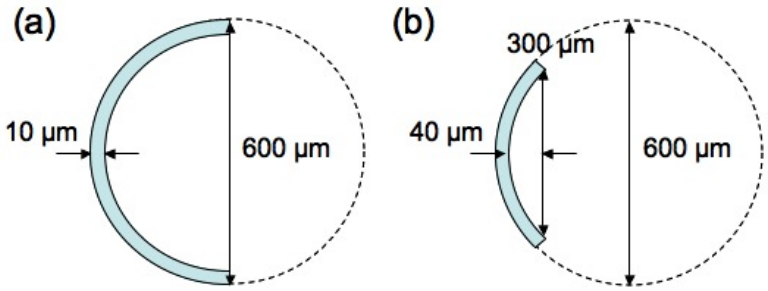

Figure 5.1: (a) A full 600 μm diameter, 10 μm thick hemispherical shell. (b) A partial shell having a chord length of 300 μm and a height of 40 μm with a 600 μm diameter.

sion efficiency.

5.1 Experimental Setup

An experiment was conducted to investigate proton focusing by irradiating a hemispherical shell made from high-density carbon by the process of chemical vapor deposition (CVD). The 1053 nm Trident laser pulse was focused by an $f/8$ parabolic mirror. The laser focal spot was defocused to irradiate a larger surface of the hemispherical shell by moving the hemispherical shell up the beam line toward the parabolic mirror. In theory, irradiating a larger section of the hemispherical shell will produce a more even sheath on the rear surface of the shell. The defocused laser spot contained 50% of the energy in a diameter of 90 μm and was normally incident onto the shells. Full and partial hemispherical shells with a diameter of 600 μm and 10 μm thick were irradiated, with the partial shells having a chord length of 300 μm and a height of 40 μm. The dimensions of the partial and full hemispheres are displayed in Fig. 5.1. Partial hemispherical shells were used because in the envisioned cone-guided Fast Ignition targets, a full hemispherical shell is too large to place within a cone. The hemispherical shells were considered freestanding since they were isolated from surrounding materials. The freestanding shells had tabs shown in Fig. 5.2(a) that allowed the shells to be mounted to a piece of Alumina. The tabs allowed the shells to be mounted for the experiment

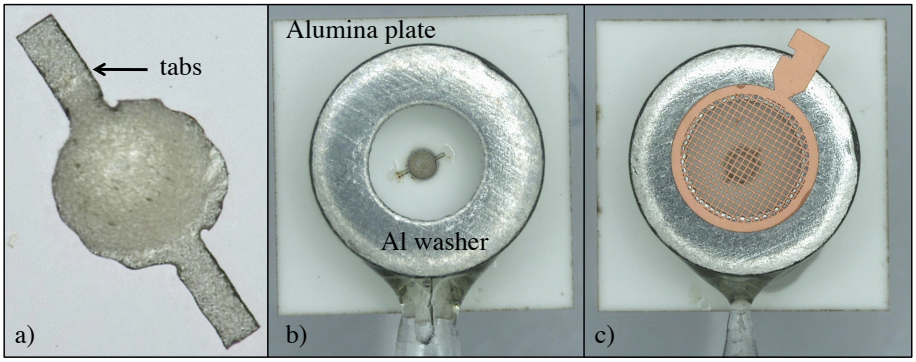

Figure 5.2: (a) A full 600 μm diameter hemispherical shell with tabs. (b) Rear view of a freestanding full hemispherical shell target without a mesh. The tabs of the shells are used to secure the hemisphere to an Alumina front plate. The shell is positioned in a hole 100 μm larger in diameter than the shell. (c) Rear view with a 200 lines per inch Cu mesh glued to the rear side of the Al washer.

but with minimal contact to the supporting structure to reduce the path the hot electrons could travel to leave the target. An image of a freestanding hemispherical target is seen in Fig. 5.2(b) and with a mesh placed downstream of the hemisphere as seen in Fig. 5.2(c). The washer is used to accurately align the mesh parallel to the shell and to accurately measure the distance to the mesh. Similar to the flat foil targets, the Al washer had a 2.24 mm inner diameter, 4.75 mm outer diameter and a thickness of 1.5 mm.

The partial shells were then attached to a 60^o cone or cylinder Al structure in order to mimic envisioned FI targets. A 60^o cone was based on previous experiments and the dimensions of the cone were calculated from envisioned proton and electron FI targets [14, 16, 82]. The opening angle of the cone in conjunction with optimal distance from the apex of the shell to the envision pre-compressed fuel capsule determined the cord length of 300 μm for the partial hemisphere and the length of the cone [22, 83]. A schematic of the target and experimental set-up is seen in Fig. 5.3 with an image of the structure target seen in Fig. 5.4. Instead of having tabs to connect the shell to the structure, the partial shells had a continuous "hat-brim", which allowed maximum contact between the shell and the surrounding structure in order to study the effect of the structure on the focusing characteristics of the generated proton beam.

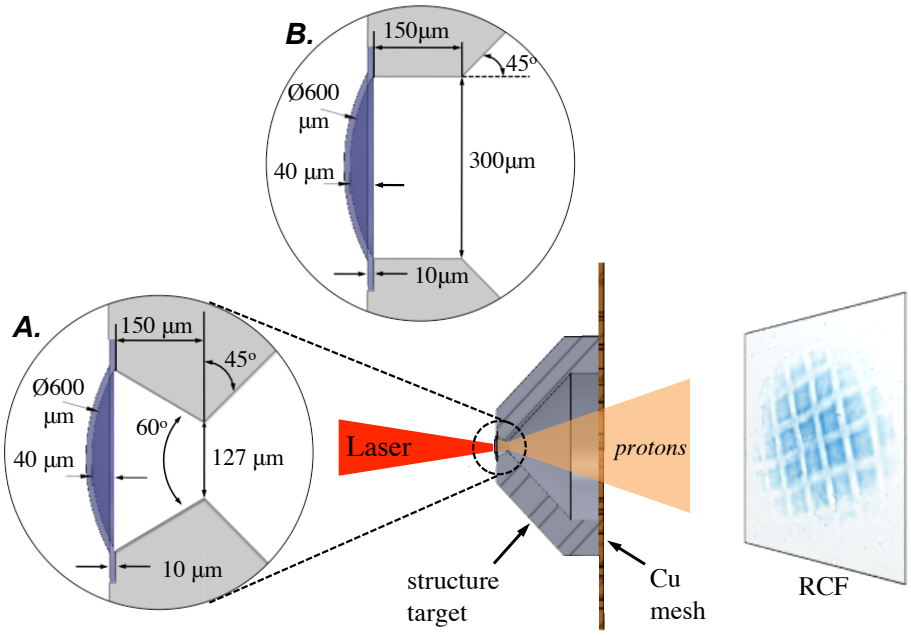

Figure 5.3: Experimental set-up and targets. The cone target (a) consists of a 10 μm thick spherical foil, attached to the Al cone structure. A Cu mesh (200 lpi) is positioned 1.5 mm from the apex of the hemisphere and the RCF stack is at 4 cm. Representative RCF data from a cone structure target is shown. The cylindrical target (b) replaces the 60^o cone with a 150 μm length cylindrical section that is 300 μm in diameter.

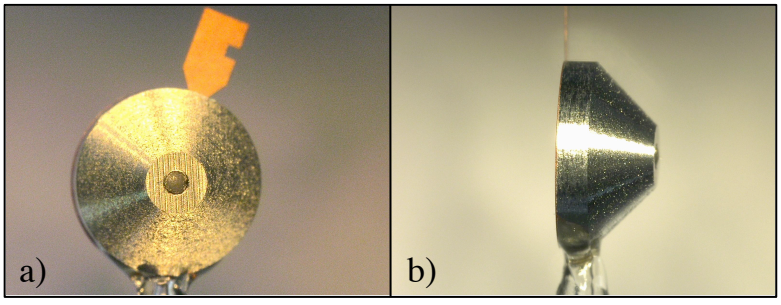

Figure 5.4: Images a of cone structure target with a mesh: (a) laser view and (b) side view.

The focusing characteristics of the generated proton beam were determined by imaging the protons through a Cu mesh, of 200 lines per inch (LPI), and recording the mesh pattern on a stack of radiochromic film (RCF). The mesh was either glued on the rear side of the structure target or positioned downstream of the freestanding shells with its position measured within $\pm$ 20 μm (seen in Fig. 5.2c and Fig. 5.4). In the experiment, a stack of RCF containing 4×4 cm squares of film alternated with aluminum filters (100 μm-1.5 mm thick) was placed 4 cm $\pm$ 500 μm behind target normal. The film was scanned using a flat bed scanner to digitized the image of the proton beam captured on the RCF.

5.2 Focusing results

The 3D ray-tracing technique described in Chapter 3 is used to investigate the focusing properties of the generated proton beam: focal spot diameter D_{80}, focal position, and laser to proton conversion efficiency. Once again, the calculation of D_{80} is dependent on accurately choosing the mesh intersection points on the RCF and adequately representing the whole proton beam by the selection of the points. In the RCF layers corresponding to the lower energy protons (E ¡ 10 MeV), distortions of the mesh were observed, as seen in Fig. 5.5(a), which prevented the use of the entire beam. Therefore, the focal spot size for the lower energy protons (below 10 MeV) could not be calculated for some target geometries as seen is Fig. 5.6. The source of the beam distortions is unclear. It is more evident at lower proton energies. One possibility is that the blurring is caused from lower energy protons that are emitted at later times from a range of radii along surface of the target. The trajectories of the lower energy protons are affected by the plasma jet set up by the higher energetic protons, which are accelerated from the target first. This is supported by separate simulations that are discussed later in the chapter, which indicate that lower energy protons from larger radii can reach different asymptotic trajectory angles. Lower energy protons are also more susceptible to mesh charging or beam interactions, which may also be a factor. The minimum diameter D_{80} is calculated for each type of target (see Fig. 5.6).

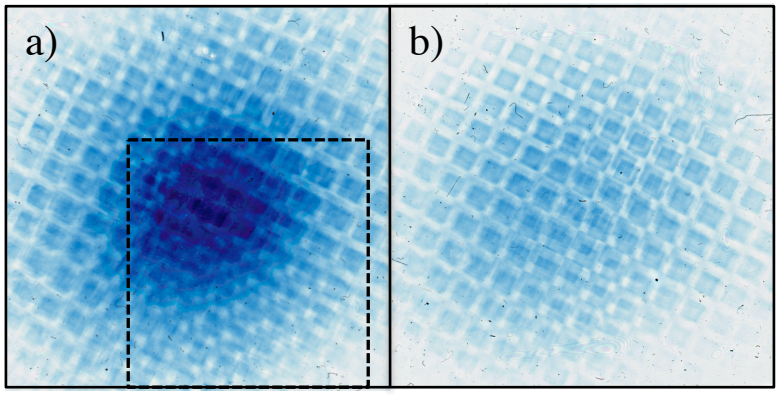

Figure 5.5: A proton beam passing through a mesh (200 lpi) placed 1.5 mm from the apex of the 600 μm diameter hemispherical shell captured on layers of RCF corresponding to the energies of (a) 7.3 MeV and (b) 11.1 MeV. The dotted line in (a) surrounds the area where the mesh image is distorted. The distortion is minimized in the higher energy layers of film.

A common feature is that D_{80} decreases with increased proton energy. Of note, the D_{80} is $\approx$ 50% smaller for the cone and cylinder targets, compared to the freestanding partial and full hemispheres.

The focal position was calculated using the measured mesh magnification on the RCF and geometrical considerations. For the cone target this position is located furthest from the source foil near z = 300 μm (z = 0 is the apex of the hemisphere) while for the other geometries, it lies within the spherical radius of curvature near z = 100 μm (see Fig. 5.7). It is also interesting to note, that while the cylinder target aides in decreasing the value of D_{80}, the calculated focal position is similar to the freestanding shells and does not seem to extend the focal position further away from the apex of the hemisphere as in the cone case. A further discussion is presented in the simulation section of this chapter.

Our calculated focal position is less than R (300 μm radius), which is much less than the previous experimental result of the position of best focus being at $1.7R$ [2]. Our results are inconsistent with protons moving in straight-line trajectories and crossing the axis beyond the equatorial plane of the hemisphere. The calculated result of focusing inside of the geometric radius would require a converging proton beam being accelerated from the surface instead of the proton

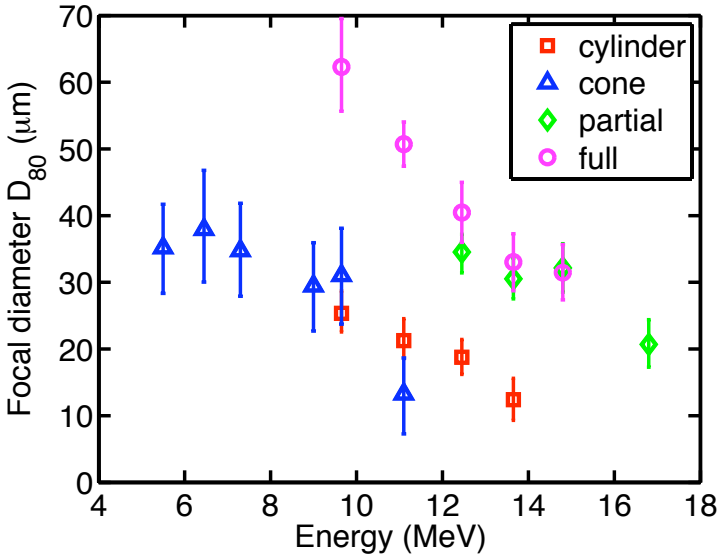

Figure 5.6: D_{80} diameter for each represented energy (RCF layer) and target geometry determined from 3D ray-tracing. Cone (blue triangles) and cylinder (red squares) enclosed geometries show significantly smaller D_{80} values at most proton energies compared to the full and partial freestanding hemispheres.

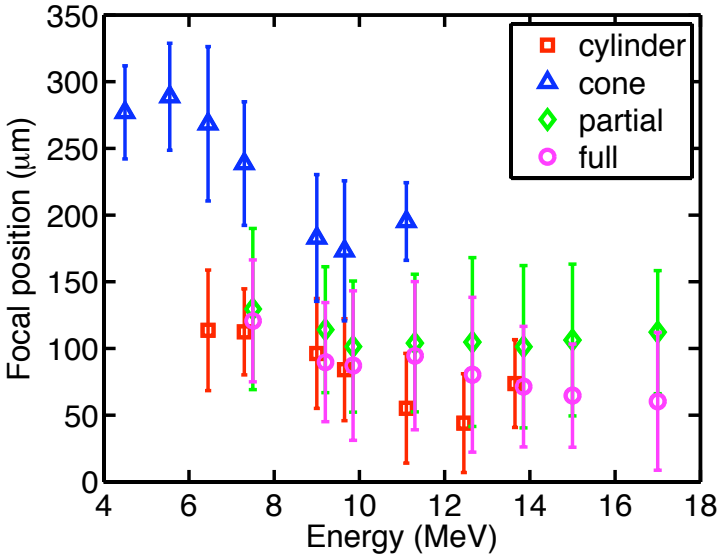

Figure 5.7: Focal position of the proton beam at different proton energies determined from the mesh magnification. For reference, the inside surface (apex) of the foil is z = 0. The cone targets (blue triangles) have an apparent focal position that is significantly further from the apex.

acceleration being perpendicular to the surface or naturally diverging as seen in flat foils, which is likely unphysical. Therefore, the proton trajectories may not move in straight line trajectories once accelerated from the surface and actually bend.

Bending of the proton trajectories was further justified when a mesh with a distinctive M in the center along with the traditional grid mesh were placed at the equatorial plane of a 600 μm diameter, 5 μm thick, full hemisphere. The orientation of the M seen in the images on the RCF in Fig. 5.8(a) and (b), is in the same orientation as in the experiment, as seen in Fig.5.8(c). These results are therefore inconsistent with the protons moving in straight-line trajectories and crossing the axis beyond the equatorial plane of the hemisphere, which would have resulted in a flipped M image on the RCF as in Fig. 5.8(d). An unflipped image consistent with the data is possible if the protons had crossed the axis inside the hemisphere ($< R$); however, this is unlikely as stated above and inconsistent with the simulation results presented in below. The focal position of the proton beam for this target is calculated using the traditional grid mesh and is shown in Fig. 5.9. The calculated focal position using the mesh magnification is near the apex of the hemispherical shell. Therefore, the protons do not move in straight line trajectories and cross the central axis inside of the hemisphere before passing through the mesh at the equatorial plane.

The calculated focal position seen in Fig. 5.7 can be explained if the proton trajectories bend near the focal region and become ballistic after that. If the trajectories bend and then become ballistic, the ray-tracing technique would project back the trajectory along the final angle of divergence of the proton trajectory, crossing the central axis closer to the surface of the hemisphere than the true focal position. The higher energy protons, which have a smaller angle of divergence, would focus to a position closer to the hemisphere as seen in Fig. 5.7. The focusing of the generated proton beam is further investigated using particle-in-cell LSP simulations.

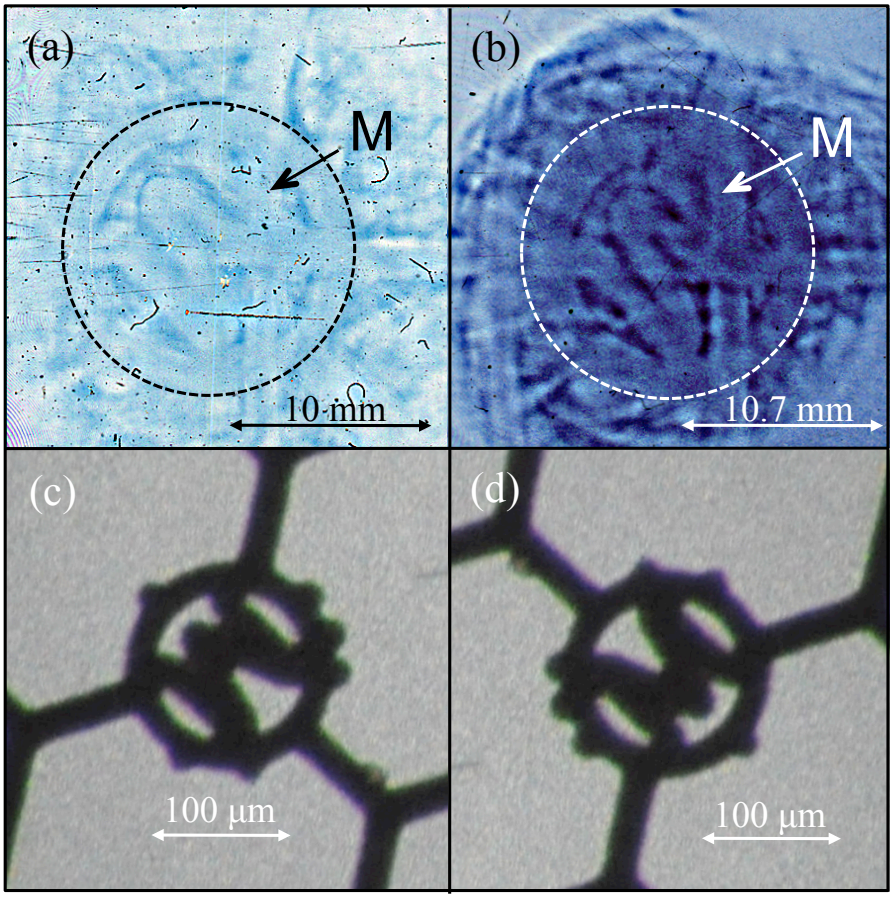

Figure 5.8: RCF layers corresponding to the energies of (a) 20 MeV and (b) 27.5 MeV, are images of a proton beam passing through a mesh, with a M in the center, placed at the equatorial plane. The dotted lines are used as a guide. (c) Orientation of the M seen down the laser axis in the experimental set-up. (d) Orientation of the M flipped horizontally and vertically if the proton trajectories were ballistic and passed through focus.

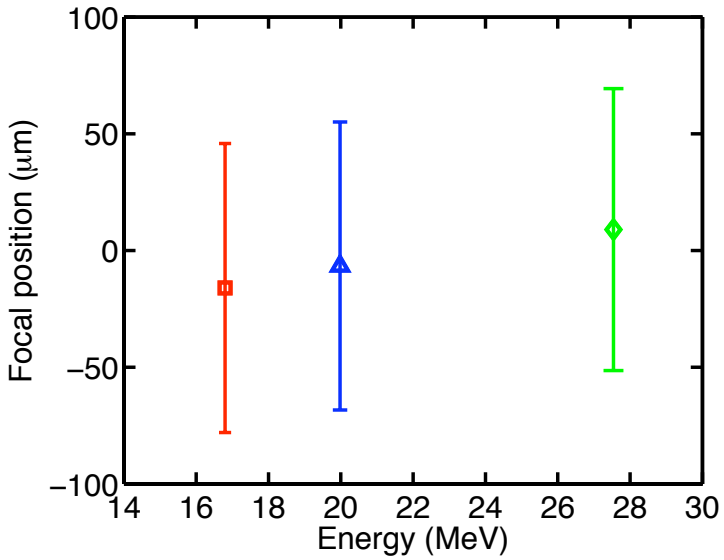

Figure 5.9: Focal position of the proton beam at three different proton energies determined from the mesh magnification with the mesh placed at the equatorial plane of a 600 μm diameter hemispherical shell. For reference, the inside surface (apex) of the foil is at 0.

5.3 Simulations

As seen in Fig. 5.7, the calculated focal position for the experimental results did not extend past the equatorial plane of the hemisphere, which is different than the results found by Snavely *et al.* [2]. To understand these results, particl-in-cell LSP simulations, described in Chapter 3, were performed to track the particle trajectories and the evolution of the beam from the target through the surrounding structure. In the simulations, the electrons are directed into the target with a relativistic Jüttner distribution with an electron temperature of $T_e = 600$ keV and a forward drift of $\gamma\beta_z = 0.6$, which results in a 45^o (30^o) forward half angle containing 50% of the energy of all electrons (those with E > 5 MeV), respectively. This distribution was chosen to be consistent with the maximum proton energies observed for the cone and partial hemispherical targets, found to be 11 MeV and 17 MeV, respectively. The simulations ran for approximately 18 ps, which was required for the protons to reach their asymptotic velocities.

Test particles were placed along the inside surface of the hemisphere in the different targets to understand the evolution of the protons and their trajectories after the protons were accelerated from the surface. The trajectories for a group of test particles that originate along the target surface at different radial positions for the freestanding partial hemisphere and cone cases are shown in Fig. 5.10 (a) and (b), respectively. In both geometries, the majority of test protons initially accelerate normal to the surface towards the geometric center at $z = 300$ μm. This is consistent with the target-normal-sheath-acceleration (TNSA) model [24, 25], where the hot electrons generated from the intense laser-matter interaction create an accelerating sheath electric field normal to the surface, which was explained in further detail in Chapter 2. After the initial acceleration, the proton trajectories do not continue in a straight line, as previously thought [1], but tend to bend away from the axis.

Further analysis of the proton simulation particles ($N_{protons} \approx 8{\times}10^6$) allows a detailed comparison with the data. The protons reach their final asymptotic velocities (i.e. become ballistic) at late times ($\sim$ 18 ps). Those trajectories are then geometrically projected back to construct a D_{80} diameter, analogous to the ray-tracing technique applied to the RCF data. Results comparing the simulation data with the experiments for the freestanding target are illustrated in Fig. 5.11, showing similar minimum values and $D_{80}(z)$ profiles. Results for the cone case also give similar agreement with the corresponding experimental data as seen in Fig. 5.12, providing confidence that the LSP code is accurately modeling the proton trajectories and the expansion physics in both open and enclosed (cone) geometries. These analyses show that the D_{80} size and minimum positions do not reflect the actual focus diameters and positions of the generated proton beam. Analyzing the curvature of the trajectories in the simulation would better predict the focal diameter and position.

The curved proton trajectories are qualitatively explained by considering a simple model for the radial electric field generated in the proton beam. Following the initial acceleration phase near the surface [24,25], the hot electrons are confined by the ambipolar field of the positively charged proton beam. The hot electron

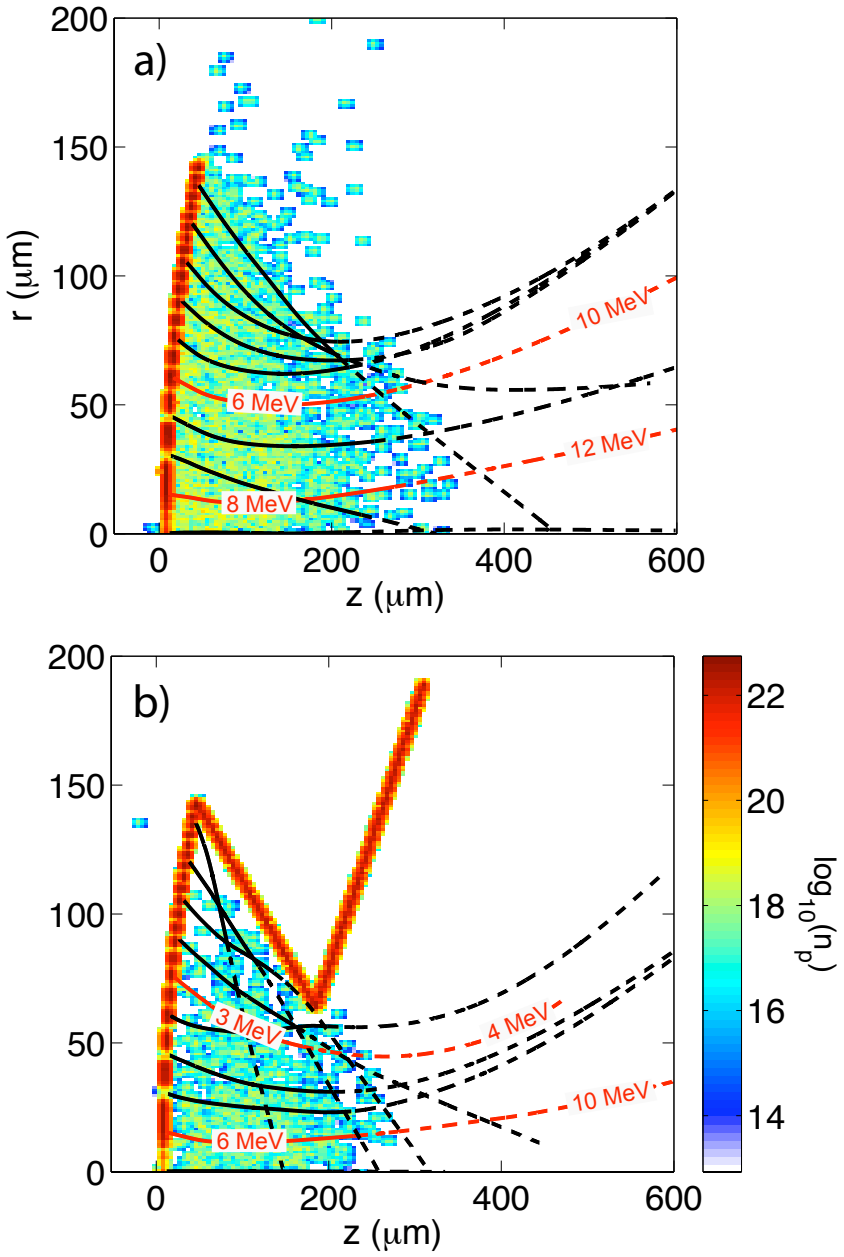

Figure 5.10: Simulation of probe particles. Proton density maps at $t = 7.3$ ps for the case of a partial hemisphere (a) without a surrounding structure and (b) with a surrounding cone structure. Note that the radial scale is expanded. For both cases, the trajectories of test proton particles are also shown, with solid lines to $t < 7.3$ ps and broken lines from 7.3 ps $< t <$ 19.2 ps. For comparison, in each plot the kinetic energy gained by two sample particles is also shown (in red), where more energetic protons are emitted closer to the axis.

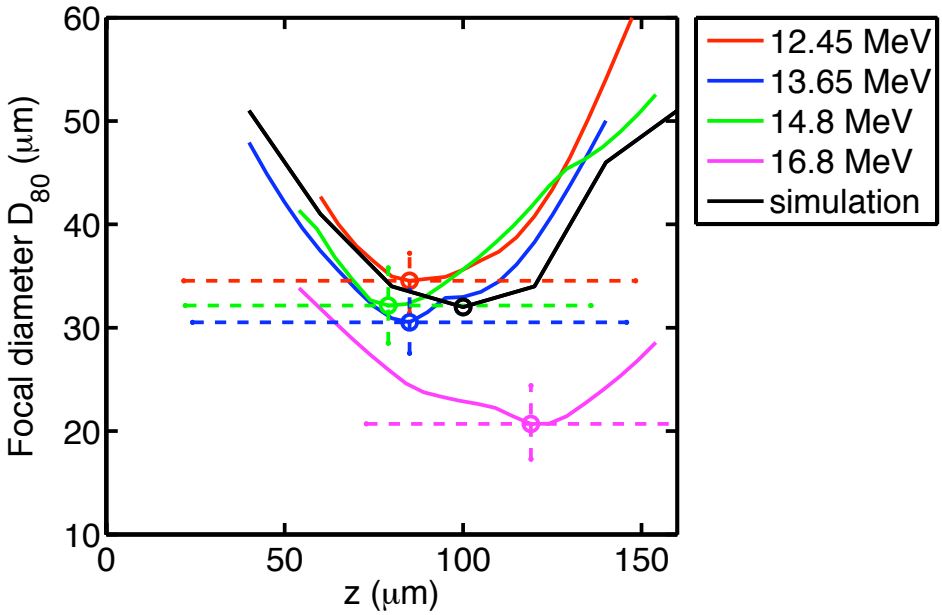

Figure 5.11: Comparison of experimental and simulation results for a freestanding partial hemisphere target. The profile of $D_{80}(z)$ is plotted. The circles along with the appropriate error bars represent the minimum D_{80}. The simulation includes all protons with E $>$ 9 MeV.

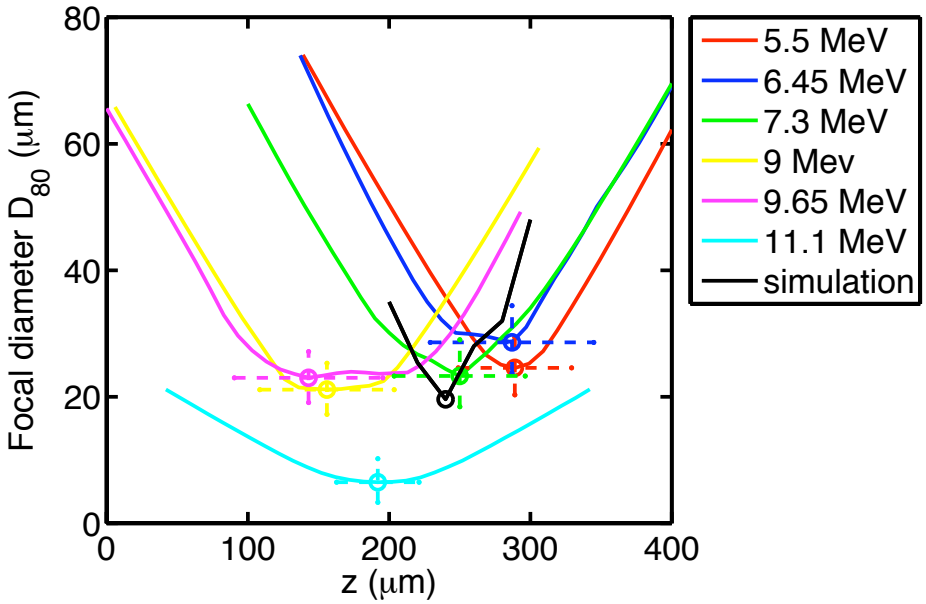

Figure 5.12: Comparison of experimental and simulation results for a cone structure target. The profile of the experimentally calculated $D_{80}(z)$ is plotted for several different proton energies. The circles along with the appropriate error bars represent the minimum D_{80}. The simulation includes all protons with E $>$ 9 MeV.

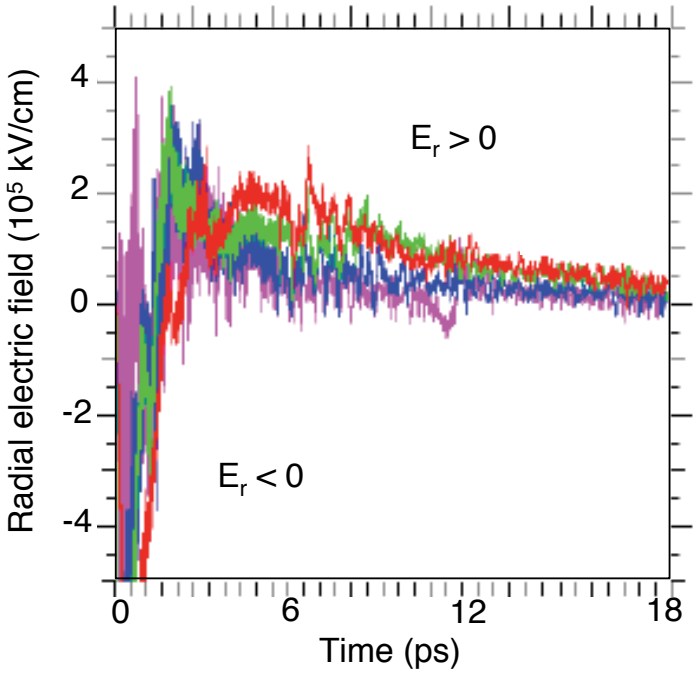

Figure 5.13: Radial electric fields in the frame of four proton test particles. The test particles are initially distributed along the surface from $r = 15$ μm (purple) to $r = 105$ μm (red).

pressure gradient sets up a radial electric field, $E_r \approx -\nabla (P_e)/n_e \approx kT_{ehot}/R$, where R is the radial scale length of the beam, kT_{ehot} is the hot electron temperature, P_e is the hot electron pressure and n_e is the hot electron density. From monitoring the time history of the electric field in the frame of selected protons, the radial field switches from being directed inward to directed outward (switched from negative to postive), as the radial field from the hot electrons surpasses the radial acceleration force that dominates near the surface. The electric field is plotted for four test particles in Fig. 5.13. We note that the weak scaling with density suggests that the focusing should not be substantially degraded for high current density beams, such as required for proton FI. Higher laser intensities, which will generate higher energy electrons, will increase the radial pressure to some extent, although this scales weakly with laser intensity, ($T_{ehot} \sim I_L^{0.5}$). Simulations indicate that the radial field in the beam is of the order of a few MV/100 μm, which is sufficient to deflect a multi-MeV proton over the spatial scale of the target. It

is also interesting to note that this heuristic model predicts that higher energy protons should penetrate to smaller radius before bending, which is the trend in the data seen in Fig. 5.6.

The inferred focal position near z = 100 μm, as shown in Fig. 5.7, is understood by considering the diagnostic method. Both the ray-tracing and magnification methods inherently assume straight-line proton trajectories. Depending on the curvature of the trajectories, the inferred focal position determined from extrapolating the trajectories to the axis may fall much inside the actual focal position of the proton beam. Therefore, the time-dependent proton distributions from the simulations are used to calculate the fluence profiles $\Delta_{80}(z)$, defined as the time integrated flux diameter that encompasses 80% of the protons through a plane at position z, which would more correctly represent the focal position and diameter of the beam. The fluence profiles $\Delta_{80}(z)$ for protons with energy > 3 MeV are plotted in Fig. 5.14, corresponding to the approximate energy required for FI deposition. [22]. For the freestanding targets, the fluence diameter is $\Delta_{80}(z) \approx 90$ μm, which is much larger than the more peaked Δ_{80} profiles seen in Fig. 5.6. As for the cone target, the fluence diameter is significantly reduced to $\Delta_{80}(z) \approx 60$ μm. The reduced Δ_{80} diameter is the result of a sheath electric field that develops along the inside surface of the cone wall, generated from the hot electron sheath that extends upward from the laser spot radius as seen in Fig. 5.15. Fig. 5.16 shows the propagation of the electric field on the cone structure wall as time progresses in the simulation. This field bends the protons that propagate near the wall surface as see in Fig. 5.10b. The sheath field is strongest during the initial phase of focusing, as the proton beam begins to propagate through the cone. At later times, the field is reduced as the hydrocarbon layer from the surface begins to expand. The sheath field effectively channels the protons through the tip of the cone, extending the focal position. A qualitative explanation for the larger focal position for the cone geometry is that the beam continues to focus as it propagates through the converging cone geometry, reaching best focus just outside the cone tip. As shown in Fig. 5.7, this effect is not observed for the other geometries, where the wall focusing is not present (or less effective for the cylinder case) and the radial hot

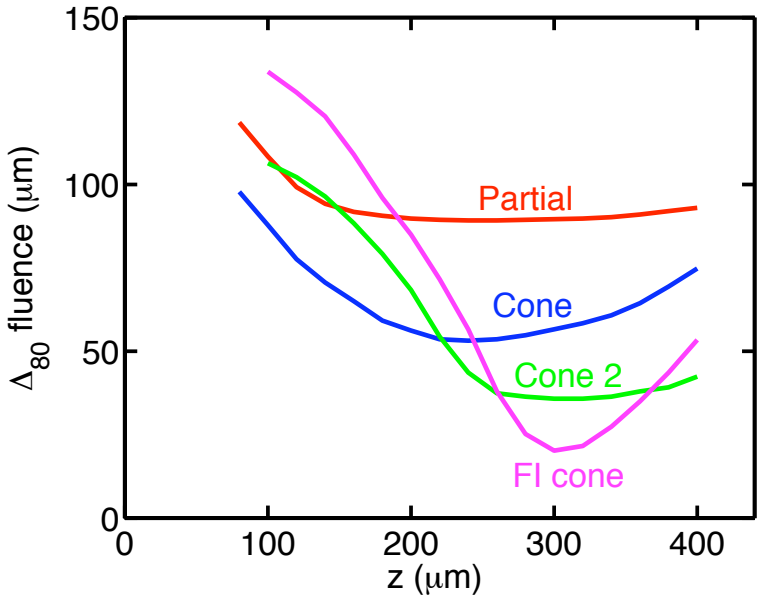

Figure 5.14: Fluence curves $\Delta_{80}(z)$ for proton energies > 3 MeV for the partial hemisphere and the cone target. Also shown are simulation results with a uniformly illuminated cone target (Cone 2), and with a uniformly illuminated thin-walled cone Au target (FI cone), as described in the text.

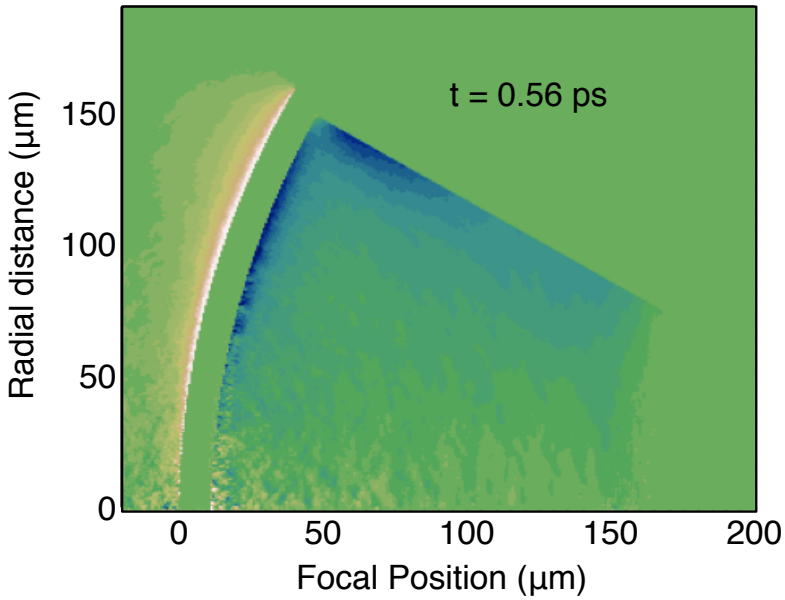

Figure 5.15: Spatial distribution of the radial electric field component for the cone target. Dark blue scale is negative (radially inward), light yellow/white is positive (radially outward). The radial field extends along the inside surface of the cone.

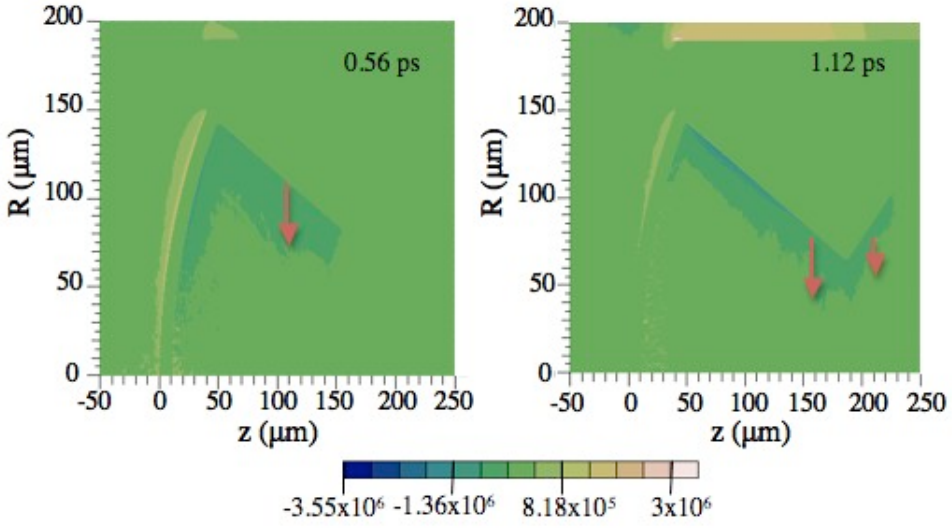

Figure 5.16: Simulated radial electric field (kV/cm) for the cone structure at two different time steps. Shows that the electric field formed on the cone wall is pointing radially inward to the center of the cone.

electron pressure in the beam starts to expand the beam at a closer distance to the apex. For both enclosed geometry cases, D_{80} is smaller than for the targets with no surrounding structure, as might be expected due to focusing effects.

The beam focusing also depends on the spatial uniformity of the hot electron source. Hot electrons generated in the intense laser spot region (laser spot diameter ≈ 90 μm) propagate transversely along the surface, creating a hot electron radial pressure gradient. Expanding the hot electron source width from 90 μm to 360 μm reduced the initial radial gradient of the hot electron sheath and resulted in a more convergent beam with Δ_{80} reduced from 60 μm to 35 μm (Fig. 5.14, Cone 2). Further simulations with a uniform source but with no hydrocarbon layer on the cone wall (which is relevant to high current FI conditions, where the hydrocarbon layer is insignificant) generated a focused beam with $\Delta_{80} \approx 20$ μm (Fig. 5.14, FI cone), well within the 40 μm FI focusing requirements. Focusing is enhanced due to the lack of the thin hydrocarbon layer, which reduces the sheath field as it expands. Based on these results, improvements in the laser uniformity and optimizing the curvature and surrounding focusing structure may allow even higher focused beam intensities to be achieved.

5.4 Conversion Efficiency

Using the method described in the Chapter 3, the laser to proton conversion efficiency is calculated for each type of target. Fig. 5.17 displays the conversion efficiency calculated from 4 MeV to the maximum proton for the corresponding target. The freestanding partial hemispherical shell gives the highest laser to proton conversion efficiency, while the cone structure target results in the lowest conversion efficiency. The large error bars for the shots with higher laser to proton conversion is a result of the first layers of RCF in the film pack being saturated. Therefore, the upper limit to the error of the dose measured in those layers is taken to be 100%. Fig. 5.18 displays the proton spectrum measured from the dose on each layer of RCF for each target with the respected error. The calculated spectrum, $\frac{dN}{dE}$, is fit to the data points within the error as explained in Chap. 3.

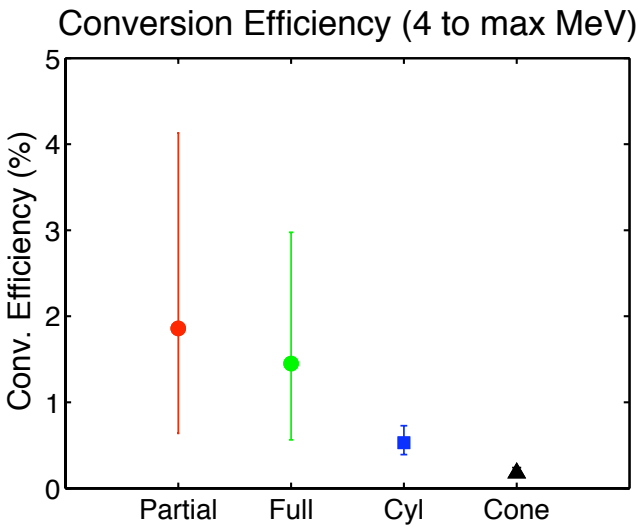

Figure 5.17: Calculated laser to proton conversion efficiency for the four different target types calculated from 4 MeV to the maximum proton energy observed in the experiment for the corresponding shot.

If there is a large error in the measured dose for the layers corresponding to the lower energy protons, a large spread of fits can represent the data. Since the majority of the total energy comes from lower energy protons, this leads to a large error in the conversion efficiency, which is the integral of $\frac{dN}{dE}$ from 4 MeV to the maximum proton energy. Fig. 5.19 shows the calculated spectrum, $\frac{dN}{dE}$, for each target corresponding to the measured spectrum in Fig. 5.18. The lines in Fig. 5.19 represent the mean fit with the error bars displaying the range of fits that can represent the measured dose. To better compare the proton conversion efficiency, the proton conversion efficiency calculated from 6 MeV to the maximum proton energy, instead of 4 MeV, is shown in Fig. 5.20. Calculating the proton conversion efficiency from 6 MeV minimizes the uncertainty in the measurement because the layers of RCF corresponding to proton energies of 6 MeV and above are not saturated. The proton spectrum also shows the maximum proton energy seen in each shot. In addition to the conversion efficiency, the maximum proton energy observed in the structure targets is less than the maximum energy seen in the freestanding shells.

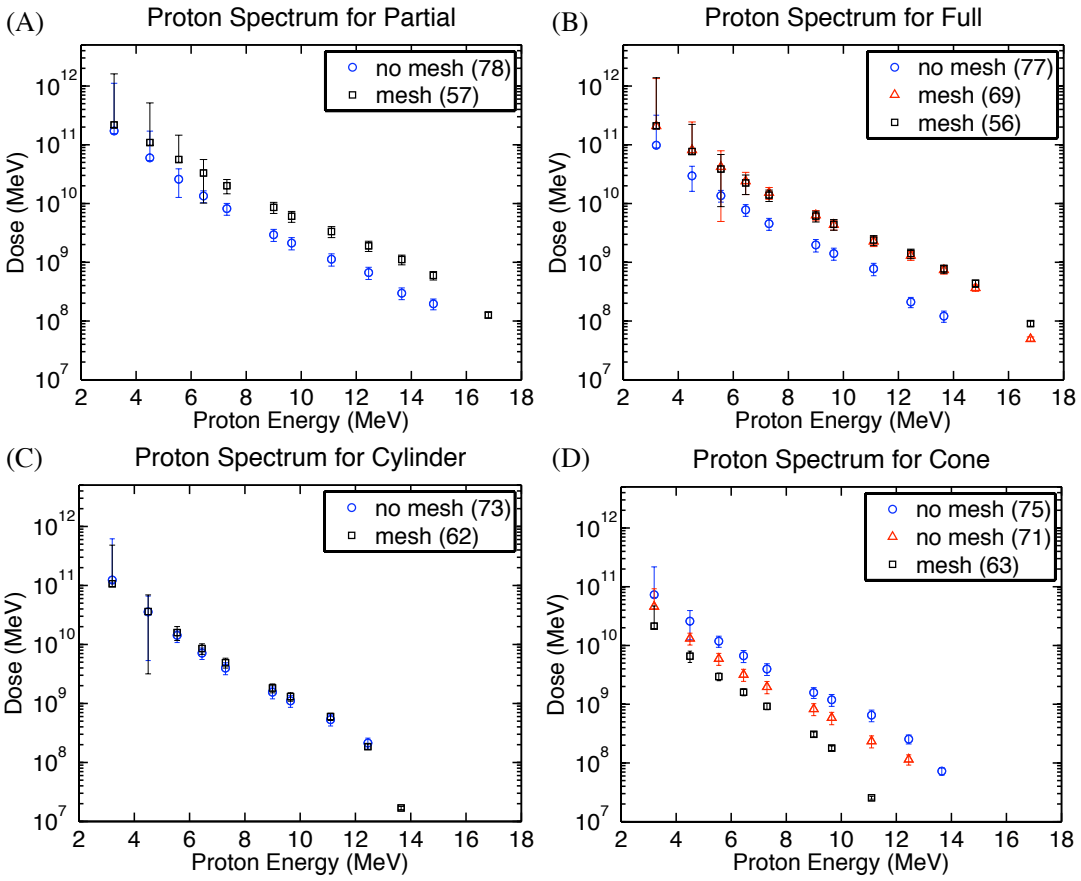

Figure 5.18: Experimentally determined proton spectrum measured from the dose on the RCF in MeV for each of the four different target types. Each marker in the spectrum represents the measured dose for a layer of RCF corresponding to the proton energies on the x-axis.

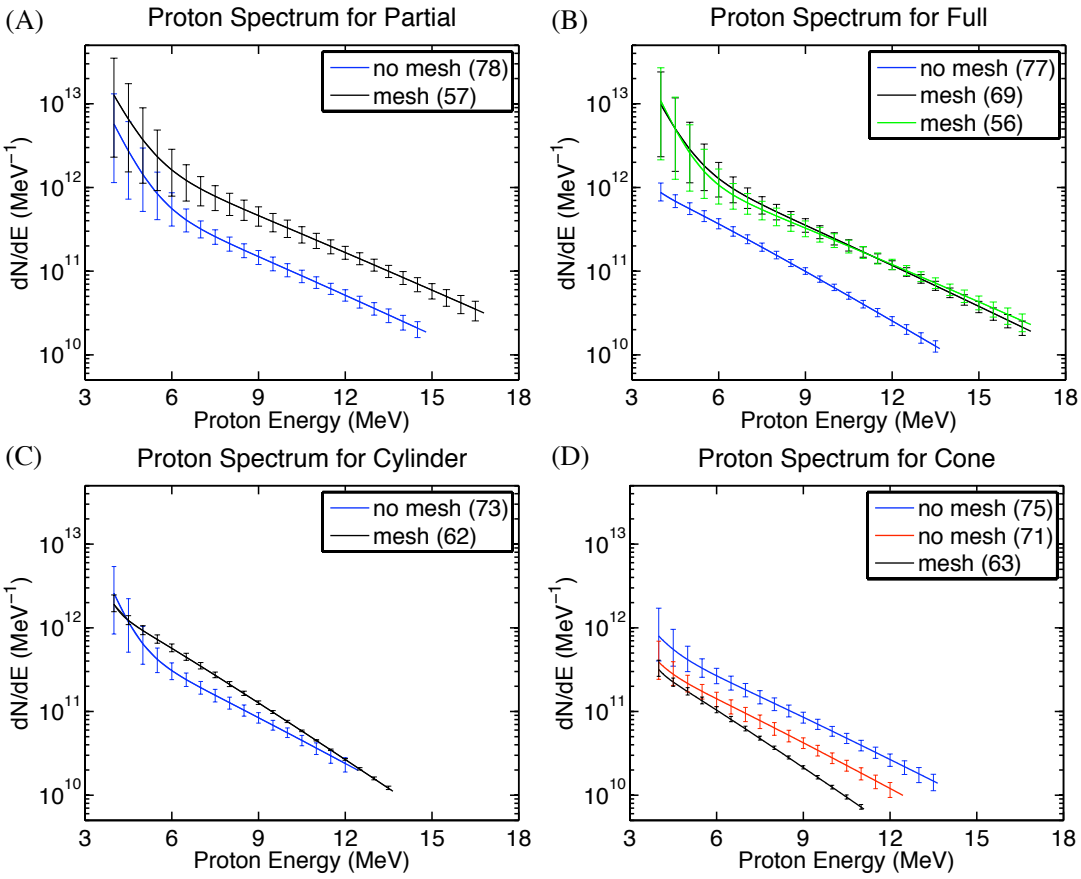

Figure 5.19: Calculated spectrum, $\frac{dN}{dE}$, for the experimentally calculated proton spectra displayed in Fig. 5.18. The calculation is explained in Chap. 3.

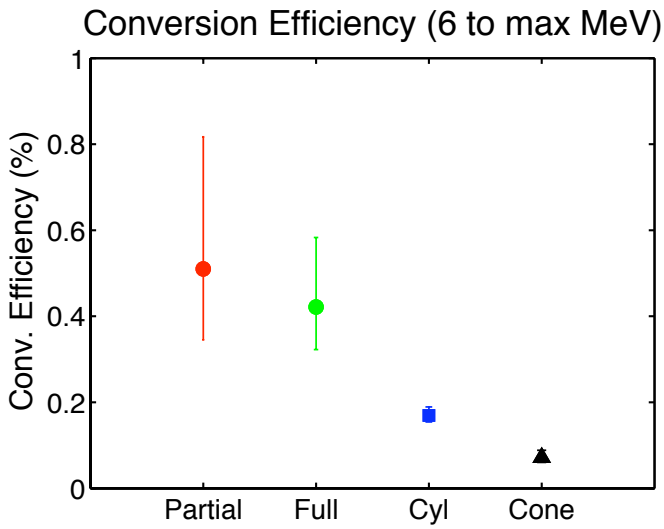

Figure 5.20: Calculated laser to proton conversion efficiency for the four different target types calculated from 6 MeV to the maximum proton energy observed in the experiment for the corresponding shot.

The decrease in conversion efficiency is related to the amount of material the hot electrons can escape to, which decreases the number of electrons that accelerate the protons. With the partial hemisphere having less material than the full hemisphere, the hot electrons travel away from the laser interaction point within the target, reach the edge of the partial hemisphere and reflux through the target. The energy from the refluxing hot electrons is used to further accelerate more protons. In the full hemisphere case, there is more material in the target for the electrons to transverse, losing more of their energy to collisions than to accelerating the protons. The effect of the electrons traversing the target and leaving the hemisphere is clearly seen in the cylinder and cone structure cases compared to the partial hemisphere. Fig. 5.21 displays the hot electron distribution for the partial hemisphere and cone structure. Early in time, the hot electron distribution is similar for both targets. As time progresses in the simulation, the hot electrons are confined and reflux within the partial hemisphere (left side of Fig. 5.21)where the hot electrons are able to accelerate more protons. With the cone structure, the partial hemisphere has direct contact with the surrounding structure. There-

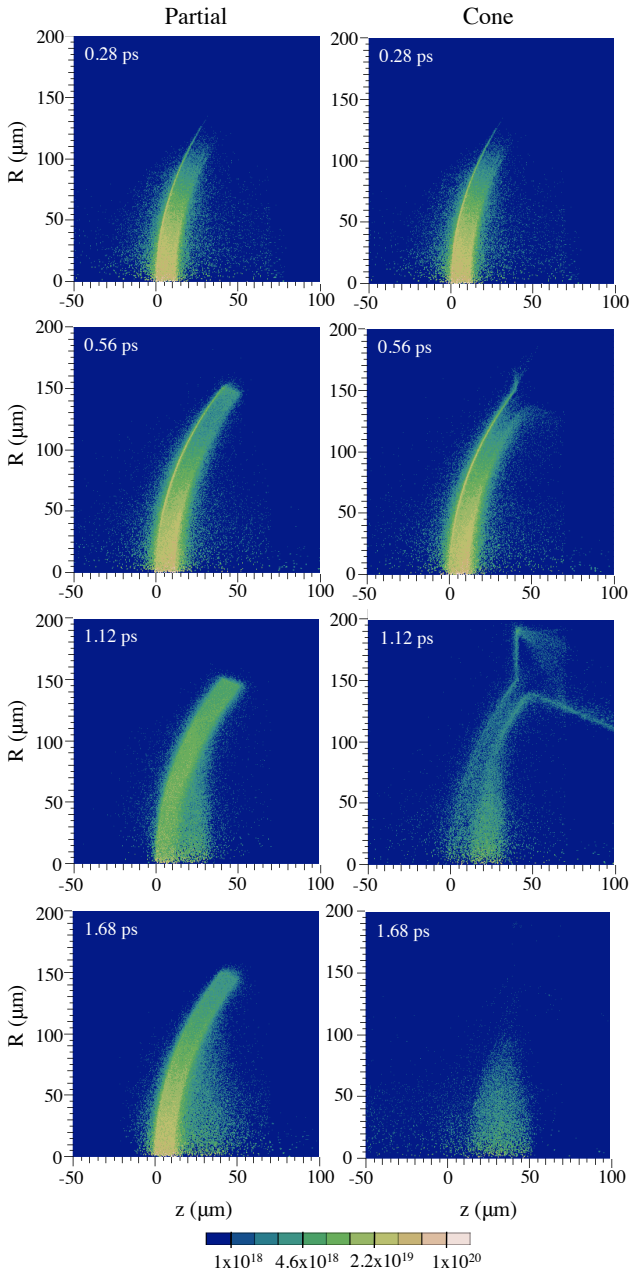

Figure 5.21: Simulated hot electron distribution (number per cm^3) for the partial hemisphere (left) and the cone structure (right) at four different time steps. Initially, the distribution for both cases are similar. Later in time, the hot electrons reach the cone structure traveling away from the hemisphere. Whereas, the electrons are confined to the partial hemisphere when a structure is not present.

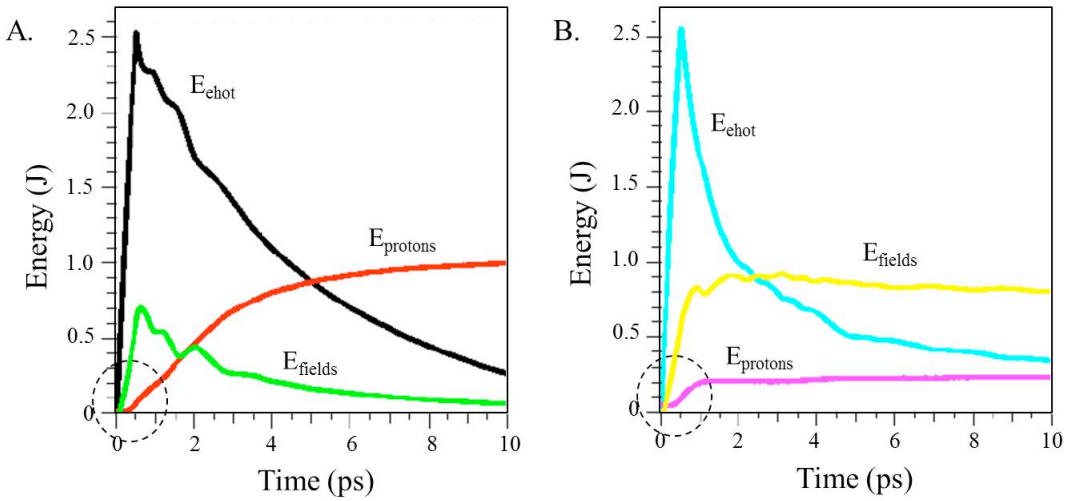

Figure 5.22: Simulated energy distribution for the (a) partial hemisphere and (b) cone structure. The distribution shows the partition of energy in the simulation to the hot electrons, protons, and fields. More energy is distributed to the fields for the cone structure instead of to the protons; whereas, for the partial hemisphere, more energy is distributed to the protons.

fore, the hot electrons escape the shell and travel into the surrounding structure (right side of Fig. 5.21) draining the amount of hot electrons available to accelerate the protons. A decrease in the number of electrons confined in the hemisphere decreases the number of protons that are accelerated.

The escape of the hot electrons from the hemisphere changes the partition of energy between the hot electrons, protons, and fields. In the structure target case, the energy partitioned into the development of the fields on the walls of the structure further decreases the amount of energy that could be given to the acceleration of the protons, which is seen in Fig. 5.22. Fig. 5.22(a) shows the partition of energy for the partial hemisphere in the simulation between the hot electrons, protons, and the fields and Fig. 5.22(b) shows the partition for the cone target. During the first picosecond of the simulation, the partition of energy for both targets are similar, which is indicated by the circled region on the plots. Fig. 5.21 and Fig. 5.23 further emphasizes the similarity showing that in the early stages of the simulation the hot electron distribution and the magnitude of the

electric field, respectively, are similar for both targets. As time progresses in the simulation, more energy is partitioned to the fields on the cone structure target compared to the partial hemisphere seen in Fig. 5.22. The energy given to the fields also decreases the amount of energy partitioned to the protons. For the partial hemisphere, the field on the hemisphere to accelerate the proton is maintained for $>$ 1.68 ps, whereas the accelerating field on the hemisphere in the cone case diminishes by 1.1 ps. The decrease in the amount of energy given to the protons in the simulations for the cone structure targets directly relates to the decrease in the proton conversion efficiency and maximum proton energy seen in the experimental results for the cone structure compared to the partial hemisphere.

For the targets presented in this chapter, there is competition between the proton focusing and the laser to proton conversion efficiency. Placing a hemispherical shell within a cone aids in focusing the proton beam, but in return, the proton conversion efficiency decreases. Ideas to improve the laser to proton conversion efficiency while placing the hemispherical shell inside of a cone is presented in the next chapter.

Chapter 5 contains material that is partially a reprint of the material as it appears in **T. Bartal**, K. A. Flippo, S. A. Gaillard, D. T. Offermann, M. E. Foord, C. Bellei, P. K. Patel, M. H. Key, R. B. Stephens, H. S. McLean, L. C. Jarrott and F. N. Beg, "Proton focusing characteristics relevant to Fast Ignition," *IEEE Transactions on Plasma Science*, Vol. 39, Issue 11, part 1, p. 2818-2819, 2011 and **T. Bartal**, M. E. Foord, C. Bellei, M. H. Key, K. A. Flippo, S. A. Gaillard, D. T. Offermann, P. K. Patel, L. C. Jarrott, D. P. Higginson, M. Roth, A. Otten, D. Kraus, R. B. Stephens, H. S. McLean, E. M. Giraldez, M. S. Wei, D. C. Gautier, and F. N. Beg, "Focusing of short pulse high intensity laser accelerated proton beams," *Nature Physics*, Vol. 8, p. 139-142, February 2012. The dissertation author was the primary investigator and author of these papers.

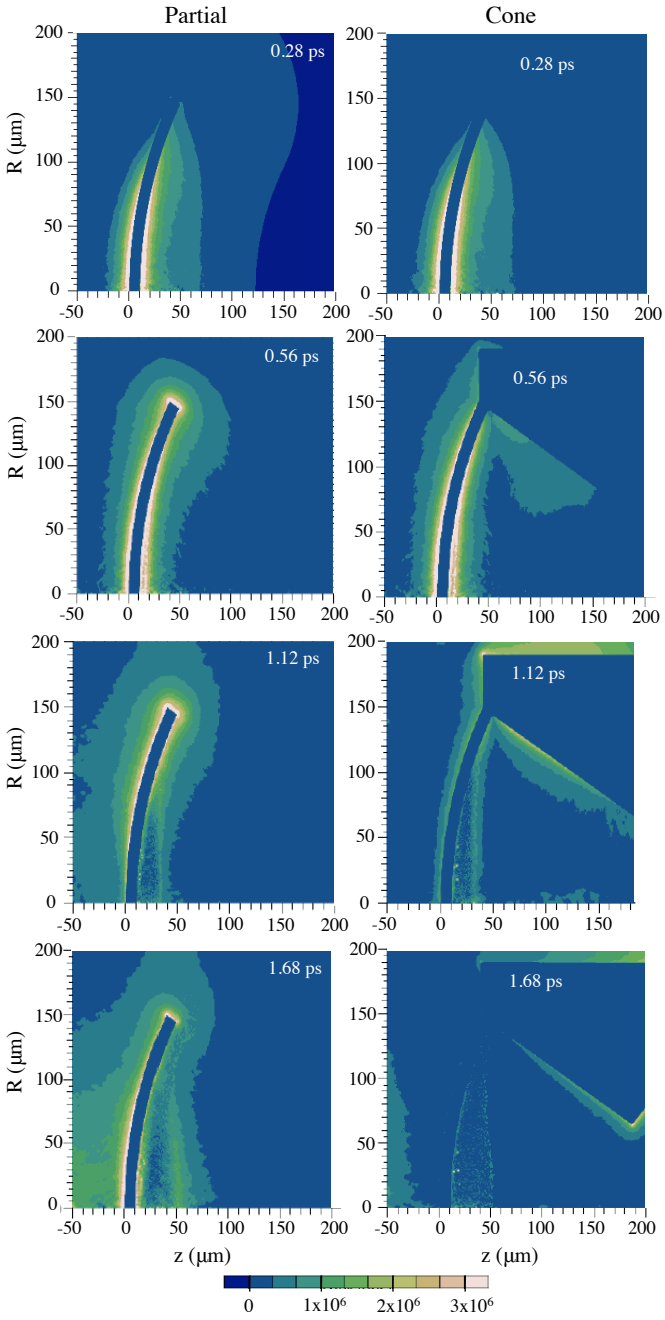

Figure 5.23: Magnitude of the simulated electric field (kV/cm) for the partial hemisphere (left) and the cone structure (right) at four different time steps. As time progresses, an electric field is formed along the wall of the structure.

Chapter 6

Summary and Future work

6.1 Summary

The ability to generate high intensity well-focused proton beams will potentially open the door to new regimes in high-energy-density science as well as enabling a broad range of new applications. For example, an intense multi-MeV proton beam incident on solid density or compressed material can create teraPascal pressures, allowing the study of the properties of warm dense matter found in the interior of giant planets like Jupiter [58]. Laser produced proton beams are also making an impact on medical applications such as isotope production [61] for Positron Emission Tomography (PET) and proton oncology [62]. In addition, energetic proton/ion beams are used to produce highly directional neutrons for applications in medicine, material science, and neutron resonance spectroscopy [63, 64]. In the inertial fusion fast ignition (FI) concept [9], an intense laser pulse generates a beam of charged particles that ignites DT fuel compressed to 300 g/cc.

For proton FI, a thin hemispherical shell is placed near the end of a hollow cone, which is embedded in the side of a DT fuel capsule. The hollow cone acts as a guide for the ignitor beam, decreases the transport distance of the protons from the hemispherical shell to the imploded fuel and helps shield the source foil from the radiation generated during the implosion of the fuel. The properties of the proton beam in this particular geometry require careful examination, especially as the viability of proton fast ignition requires both 40 μm focusing at the compressed

fuel and a conversion efficiency of 15% from petawatt laser pulse energy to proton beam energy [22, 83]. This thesis addresses both of these issues using flat foils and hemispherical shell targets.

The expansion of the proton beam was first investigated using flat foils. A 200 lpi Cu mesh was located downstream of a 21 μm thick CVD (carbon vapor deposition) flat foil. The image of the mesh was imprinted into the proton beam as it passed through the mesh. The beam was collected with a pack of radiochromic film, which was located 4 cm downstream of the flat foil and was used to determine the virtual focus position of the proton beam and the laser to proton conversion efficiency. Two different schemes were used to mount the flat foils to determine if the mounting technique affected the afore mentioned characteristics. First, the foil and the mesh were completely separated by mounting each one on a different stalk. Second, the foil was mounted on a washer where the mesh was mounted on the opposite side in order for the foil and the mesh to be parallel.

It has been conventional wisdom that the proton beam generated from a flat foil has a virtual focus [1]. However, using the ray-tracing technique described in Chapter 3, we observed a real focus for proton beams generated from flat foils. From our experimental observations, the target properties and the duration of the hot electron source (i.e. laser pulse length) affect the shape of the expansion sheath on the rear side of the foil and thus changes the trajectories of the protons from being truly ballistic. In the experiments presented, the length of the laser pulse was five times longer than in Ref. [1].

The physics of a non-virtual focus can be explained as follows. Initially, the protons are accelerated normal to the rear surface of the foil by an electrostatic sheath field set up by the escaping hot electrons, since the sheath is located near the foil surface. As time progresses, electrons are still being accelerated in the system by the laser irradiation, and the sheath field, which is the leading edge of the expansion, extends further away for the rear surface of the foil. Since more energetic electrons are accelerated near the central axis, which in the axis of the laser interaction, the expansion is greater near the center than in the wings causing a bell-shaped sheath expansion. The protons are expanding with the sheath and

are now accelerated normal to the sheath field. Therefore, there are large gradients between the central axis and the wings of the expansion causing the protons that are accelerated in this region to have a larger radial velocity component than the protons accelerated near the central axis. The extent of the gradients in the sheath field increases in time as more hot electrons are accelerated into the target. Higher energy protons that escape the target earlier in time and are accelerated the longest, have less radial velocity than protons escaping later in time, which can see the gradients in the sheath field. Protons that are emitted further away from the center axis will a larger radial velocity than protons emitted near the central axis for the same reason. This effect is observed in the RCF image where the magnification of the mesh elements increases radially outward from the center. Therefore, when the trajectories of the protons with larger radial velocity are traced from the image on the RCF back through the mesh to determine the focal position, the trajectories will converge at a spot on the rear side of the foil appearing to be a real focus.

The mounting scheme also affects the trajectories of the protons. When the foil is mounted on the Al washer, the hot electrons accelerated in the target by the laser transverse the foil and travel into the washer. The electrons that escape into the washer set up an electric field on the walls of the washer. This electric field affects the trajectories of the lower energy protons that are emitted from the foil at a larger radial distance from the center. The drain of electrons into the washer also decreases the amount of electrons available to accelerate the protons. This is observed in the decrease in the laser to proton conversion efficiency. The flat foils mounted on a washer have a lower to conversion efficiency than the separately mounted foil and mesh. The knowledge that was gained from the flat foil experiments provides the foundation for understanding a proton beam generated from a hemispherical shell target.

The focal position and the laser to proton conversion efficiency was experimentally calculated using hemispherical shell targets. Full and partial hemispherical shells, 600 μm in diameter, were mounted with small tabs to minimize the contact between the shell and an Alumina plate for mounting purposes in or-

der for these shells to be as freestanding as possible. Analyzing the proton beam generated from the freestanding targets using the ray-tracing technique, the calculated focal position did not extend beyond the equatorial plane of the hemisphere. This observation in focal position is much less than the focal position of $1.7R$ (where R is the radius of curvature of the shell) determined from proton heating experiments [2]. With further exploration using simulations with the hybrid particle-in-cell code LSP (large scale plasma), it was determined that protons do not move in straight-line trajectories but actually bend near the focal region. The curved proton trajectories are explained by a radial electric field generated in the proton beam set up by the hot electron pressure gradient, where the hot electrons are confined in the beam by the ambipolar field of the positively charged proton beam. The radial electric field scales at $E_r \approx kT_{ehot}/R$, where R is the radial scale length of the beam and kT_{ehot} is the hot electron temperature. Looking at the time history of the simulations, the radial electric field in the proton beam switches from being directed inward to directed outward (switched from negative to postive), as the radial field from the hot electrons surpasses the radial acceleration force that dominates near the surface of the source foil. Higher energy protons are less affected by the field due to having a higher velocity and are able to focus to a smaller spot size before bending, which is observed in the experiments. Due to the bending of the proton trajectories, the focal position determined from extrapolating the trajectories to the axis may fall much inside the actual focal position of the proton beam.

The first demonstration of the generation and focusing of a proton beam in a FI geometry was also presented. A proton beam was generated from a curved focusing surface (i.e. hemispherical shell) which propagated and was channeled by surface fields through an enclosed cone structure, similar to the envisioned FI targets [14]. Instead of tabs in the freestanding case, the hemispherical shell had direct contact with the surrounding structure. Therefore, hot electrons accelerated in the shell by the laser irradiation, transverse the shell and escape into the surrounding structure, which was also observed when flat foils were mounted with a washer. The escaping hot electrons set up an electric field on the inner walls of the

surrounding structure, which affects the trajectories of the proton beam passing through the structure. This effect is more prevalent with the structure targets than the flat foils mounted on a washer due to the reduced size of the attached structure and the distance the electrons have to travel to escape into the surrounding structure. The sheath field on the walls of the structure is the greatest during the initial phase of the focusing, when the proton beam begins to propagate through the structure and reduces as the field begins to expand the hydrocarbon layer present on the walls. The field on the walls effectively channels the proton beam through the structure allowing the beam only to expand once the proton beam is outside of the structure, which pushes the focal position of the beam further away from the rear surface of the source foil. The structure decreases the focal spot size of the generated proton beam compared to the freestanding hemispherical shells and also increases the focal distance from the source foil. Since electrons are escaping the hemispherical shell into the surrounding structure, the laser to proton conversion efficiency is decreased when more mass is added around the hemisphere, which was also observed when the flat foils were mounted on a washer.

6.2 Future Work

The experiments that were conducted made great strides in the understanding of the focusing characteristics of generated proton beams. Additional experiments can be conducted to further explore the proton beam characteristics. First, side-on proton radiography can be done to study the expansion physics using the freestanding hemispherical targets. Since the partial hemispherical shell has a height of only 40 μm a majority of the expansion can be observed from the side view. The deflection of the proton beam generated from a secondary foil that transverses the proton beam generated from the hemispherical shell can be used to analyze the strength of the fields inside of the proton beam from the shell and the rate of expansion. The proton beam from the secondary foil is captured with a radiochromic film pack, where the layers will provide coarse time resolution of the expansion. The beam collected on the RCF could also allow for the focal po-

sition and spot size of the proton beam to be calculated. Proton radiography has been previously been used to investigate electrostatic and magnetic fields in laser produce plasmas [84] and from wire-attached cone targets [85] .

We observed that when a hemispherical shell is placed within a surrounding structure, the surrounding structure aids in focusing the proton beam; however, the structure decreases the laser to proton conversion efficiency. To help increase the laser to proton conversion, different techniques to mount the hemispherical shell inside of the structure can be investigated. Instead of the shells having direct contact with the surrounding structure, the shells can be mounted to the structure with tabs, similar to the freestanding shells. In addition, using thin wall cones would decrease the amount of material the hot electrons in the shell could escape into and increase the laser to proton conversion compared to the conversion efficiency for the current structured targets. The trade-off between the proton beam focusing and the conversion efficiency is one aspect that needs further investigation.

Using the structure targets discussed in this thesis and the redesigned targets suggested in the proceeding paragraph, proton heating of a secondary foil could also be used to characterize the generated proton beam and be compared to the observations from past experiments [2, 20]. A secondary Copper foil can be placed at the opening of the structured target, which would be heated by the generated proton beam. The temperature of the heated foil can be measured using extreme ultra-voilet (XUV) imaging [86] and the size of the heated area could also be calculated from the images. XUV imaging could also be done on thin walled Copper cones. The heating of the cone would give an indication of how much electron energy is being partitioned into the cone and taken away from accelerating the protons.

The research presented in this thesis pushed against the conventional wisdom that protons generated from flat foils and hemispherical shells have ballistic trajectories and introduced a new understanding. Even though advances have been made in this area, several unknowns are still present which require further investigation.

Bibliography

[1] M. Borghesi, A. Mackinnon, D. Campbell, D. Hicks, S. Kar, P. Patel, D. Price, L. Romagnani, A. Schiavi, and O. Willi, "Multi-mev proton source investigations in ultraintense laser-foil interactions," *Phys. Rev. Lett.*, vol. 92, no. 5, p. 55003, 2004.

[2] R. Snavely, B. Zhang, K. Akli, Z. Chen, R. Freeman, P. Gu, S. Hatchett, D. Hey, J. Hill, and M. Key, "Laser generated proton beam focusing and high temperature isochoric heating of solid matter," *Phys. Plasmas*, vol. 14, p. 092703, 2007.

[3] R. F. Post, "Controlled fusion research—an application of the physics of high temperature plasmas," *Rev. Mod. Phys.*, vol. 28, pp. 338–362, Jul 1956.

[4] J. D. Lindl, *Inertial Confinement Fusion*. New York, NY: Springer, 1998.

[5] J. R. M. Jr., K. E. Rothe, and R. D. Sharp, "Fusion reactivity graphs and tables for charge and particle reactions, ornl/tm-6914," *Technical report, Oak Ridge National Laboratory*, 1979.

[6] S. Atzeni and J. M. ter Vehn, *The physics of inertial fusion*. New York: Oxford University Press Inc., 2004.

[7] M. Key, "Status of and prospects for the fast ignition inertial fusion concept," *Phys. Plasmas*, vol. 14, p. 055502, 2007.

[8] M. Rosen, "The physics issues that determine inertial confinement fusion target gain and driver requirements: A tutorial," *Phys. Plasmas*, vol. 6, p. 1690, 1999.

[9] M. Tabak, J. Hammer, M. Glinsky, W. Kruer, S. Wilks, J. Woodworth, E. Campbell, M. Perry, and R. Mason, "Ignition and high gain with ultrapowerful lasers," *Phys. Plasmas*, vol. 1, no. 5, p. 1626, 1994.

[10] A. J. Mackinnon, "Fast ignition using energetic electrons or protons," 2007.

[11] M. Tabak, D. Hinkel, S. Atzeni, E. M. Campbell, and K. Tanaka, "Fast ignition: Overview and background," *Fusion Sci. Technol.*, vol. 26, pp. 254–276, 2006.

[12] S. Atzeni, "Inertial fusion fast ignitor: Igniting pulse parameter window vs the penetration depth of the heating particles and the density of the precompressed fuel," *Phys. Plasmas*, vol. 6, p. 3316, 1999.

[13] Y. Sentoku, W. Kruer, M. Matsuoka, and A. Pukhov, "Laser hole boring and hot electron generation in the fast ignition scheme," *Fusion Sci. Technol.*, vol. 26, pp. 278–296, 2006.

[14] R. Kodama, P. Norreys, K. Mima, A. Dangor, R. Evans, H. Fujita, Y. Kitagawa, K. Krushelnick, T. Miyakoshi, and N. Miyanaga, "Fast heating of ultrahigh-density plasma as a step towards laser fusion ignition," *nature*, vol. 412, no. 6849, pp. 798–802, 2001.

[15] M. Key, K. Akli, F. Beg, M. Chen, H. Chung, R. Freeman, M. Foord, J. Green, P. Gu, and G. Gregori, "Study of electron and proton isochoric heating for fast ignition," *J. Phys. IV France*, vol. 133, pp. 371–378, 2006.

[16] W. Theobald, A. Solodov, C. Stoeckl, K. Anderson, R. Betti, T. Boehly, R. Craxton, J. Delettrez, C. Dorrer, and J. Frenje, "Initial cone-in-shell fast-ignition experiments on omega," *Phys. Plasmas*, vol. 18, p. 056305, 2011.

[17] R. Snavely, M. Key, S. Hatchett, T. Cowan, M. Roth, T. Phillips, M. Stoyer, E. Henry, T. Sangster, and M. Singh, "Intense high-energy proton beams from petawatt-laser irradiation of solids," *Phys. Rev. Lett.*, vol. 85, no. 14, pp. 2945–2948, 2000.

[18] E. Clark, K. Krushelnick, M. Zepf, F. Beg, M. Tatarakis, A. Machacek, M. Santala, I. Watts, P. Norreys, and A. Dangor, "Energetic heavy-ion and proton generation from ultraintense laser-plasma interactions with solids," *Phys. Rev. Lett.*, vol. 85, no. 8, pp. 1654–1657, 2000.

[19] M. Roth, T. Cowan, M. Key, S. Hatchett, C. Brown, W. Fountain, J. Johnson, D. Pennington, R. Snavely, and S. Wilks, "Fast ignition by intense laser-accelerated proton beams," *Phys. Rev. Lett.*, vol. 86, no. 3, pp. 436–439, 2001.

[20] P. Patel, A. Mackinnon, M. Key, T. Cowan, M. Foord, M. Allen, D. Price, H. Ruhl, P. Springer, and R. Stephens, "Isochoric heating of solid-density matter with an ultrafast proton beam," *Phys. Rev. Lett.*, vol. 91, no. 12, p. 125004, 2003.

[21] A. Caruso and V. Pais, "The ignition of dense dt fuel by injected triggers," *Nuclear Fusion*, vol. 36, no. 6, p. 745, 1996.

[22] S. Atzeni, M. Temporal, and J. Honrubia, "A first analysis of fast ignition of precompressed icf fuel by laser-accelerated protons," *Nuclear Fusion*, vol. 42, p. L1, 2002.

[23] A. Fews, P. Norreys, F. Beg, A. Bell, A. Dangor, C. Danson, P. Lee, and S. Rose, "Plasma ion emission from high intensity picosecond laser pulse interactions with solid targets," *Phys. Rev. Lett.*, vol. 73, no. 13, pp. 1801–1804, 1994.

[24] S. Hatchett, C. Brown, T. Cowan, E. Henry, J. Johnson, M. Key, J. Koch, A. Langdon, B. Lasinski, and R. Lee, "Electron, photon, and ion beams from the relativistic interaction of petawatt laser pulses with solid targets," *Phys. Plasmas*, vol. 7, p. 2076, 2000.

[25] S. Wilks, A. Langdon, T. Cowan, M. Roth, M. Singh, S. Hatchett, M. Key, D. Pennington, A. Mackinnon, and R. Snavely, "Energetic proton generation in ultra-intense laser–solid interactions," *Phys. Plasmas*, vol. 8, p. 542, 2001.

[26] M. Allen, P. Patel, A. Mackinnon, D. Price, S. Wilks, and E. Morse, "Direct experimental evidence of back-surface ion acceleration from laser-irradiated gold foils," *Phys. Rev. Lett.*, vol. 93, p. 265004, Dec 2004.

[27] M. Allen, Y. Sentoku, P. Audebert, A. Blazevic, T. Cowan, J. Fuchs, J. Gauthier, M. Geissel, M. Hegelich, and S. Karsch, "Proton spectra from ultraintense laser–plasma interaction with thin foils: Experiments, theory, and simulation," *Physics of Plasmas*, vol. 10, p. 3283, 2003.

[28] A. Mackinnon, Y. Sentoku, P. Patel, D. Price, S. Hatchett, M. Key, C. Andersen, R. Snavely, and R. Freeman, "Enhancement of proton acceleration by hot-electron recirculation in thin foils irradiated by ultraintense laser pulses," *Phys. Rev. Lett.*, vol. 88, no. 21, p. 215006, 2002.

[29] T. Cowan, J. Fuchs, H. Ruhl, A. Kemp, P. Audebert, M. Roth, R. Stephens, I. Barton, A. Blazevic, and E. Brambrink, "Ultralow emittance, multi-mev proton beams from a laser virtual-cathode plasma accelerator," *Phys. Rev. Lett.*, vol. 92, no. 20, p. 204801, 2004.

[30] J. Fuchs and P. Antici, "Laser-driven proton scaling laws and new paths towards energy increase," *Nature Physics*, vol. 2, no. 1, pp. 48–54, 2005.

[31] D. Hey, M. Foord, M. Key, S. LePape, A. MacKinnon, P. Patel, Y. Ping, K. Akli, R. Stephens, and T. Bartal, "Laser-accelerated proton conversion efficiency thickness scaling," *Physics of Plasmas*, vol. 16, p. 123108, 2009.

[32] L. Robson, P. Simpson, R. Clarke, K. Ledingham, F. Lindau, O. Lundh, T. Mccanny, P. Mora, D. Neely, and C. Wahlström, "Scaling of proton acceleration driven by petawatt-laser–plasma interactions," *Nature Physics*, vol. 3, no. 1, pp. 58–62, 2006.

[33] F. F. Chen, *Introduction to Plasma Physics and Controlled Fusion*. New York, NY: Springer, 2006.

[34] W. L. Kruer, *The Physics of Laser Plasma Interactions*. Boulder, CO: Westview Press, 2003.

[35] P. Gibbon, *Short Pulse Laser Interactions with Matter*. London, UK: Imperial College Press, 2005.

[36] S. Wilks and W. Kruer, "Absorption of ultrashort, ultra-intense laser light by solids and overdense plasmas," *Quantum Electronics, IEEE Journal of*, vol. 33, no. 11, pp. 1954–1968, 1997.

[37] C. D. Chen, *Spectrum and Conversion Efficiency Measurements of Superthermal Electrons from Relativistic Laser Plasma Interactions*. PhD thesis, Massachusetts Institute of Technology, Boston, MA, 2009.

[38] G. Malka and J. L. Miquel, "Experimental confirmation of ponderomotive-force electrons produced by an ultrarelativistic laser pulse on a solid target," *Phys. Rev. Lett.*, vol. 77, p. 75, 1996.

[39] C. E. Max, *Physics of Laser Fusion*. Springfield, VA: U.S. Department of Commerce, 1982.

[40] T. W. Johnston and J. Dawson, "Correct values for high frequency power absorption by inverse bremsstrahlung in plasmas," *Phys. Fluids*, vol. 16, p. 722, 1973.

[41] V. L. Ginsburg, *Propagation of Electromagnetic Waves in Plasmas*. New York: Gordon and Breach, 1960.

[42] V. P. Silin, "Nonlinear high frequency plasma conductivity," *Sov. Phys. - JETP*, vol. 20, pp. 1510–1516, 1965.

[43] H. Brysk, "Multiphoton inverse bremsstrahlung," *Journal of Physics A: Mathematical and General*, vol. 8, no. 8, p. 1260, 1975.

[44] L. Schlessinger and J. Wright, "Inverse-bremsstrahlung absorption rate in an intense laser field," *Phys. Rev. A*, vol. 20, pp. 1934–1945, Nov 1979.

[45] A. Langdon, "Nonlinear inverse bremsstrahlung and heated-electron distributions," *Phys. Rev. Lett.*, vol. 44, no. 9, pp. 575–579, 1980.

[46] D. W. Forslund, J. M. Kindel, and K. Lee, "Theory of hot-electron spectra at high laser intensity," *Phys. Rev. Lett.*, vol. 39, pp. 284–288, Aug 1977.

[47] F. Brunel, "Not-so-resonant, resonant absorption," *Phys. Rev. Lett.*, vol. 59, no. 1, pp. 52–55, 1987.

[48] S. Kato, B. Bhattacharyya, A. Nishiguchi, and K. Mima, "Wave breaking and absorption efficiency for short pulse p-polarized laser light in a very steep density gradient," *Physics of Fluids B: Plasma Physics*, vol. 5, no. 2, pp. 564–570, 1993.

[49] P. Mora, "Plasma expansion into a vacuum," *Phys. Rev. Lett.*, vol. 90, no. 18, p. 185002, 2003.

[50] P. Mora, "Collisionless expansion of a gaussian plasma into a vacuum," *Physics of Plasmas*, vol. 12, p. 112102, 2005.

[51] A. Baitin and K. Kuzanyan, "A self-similar solution for expansion into a vacuum of a collisionless plasma bunch," *Journal of plasma physics*, vol. 59, no. 01, pp. 83–90, 1998.

[52] S. Gitomer, R. Jones, F. Begay, A. Ehler, J. Kephart, and R. Kristal, "Fast ions and hot electrons in the laser–plasma interaction," *Physics of Fluids*, vol. 29, p. 2679, 1986.

[53] D. S. Hey, *Laser-Accelerated Proton Beams: Isochoric Heating and Conversion Efficiency*. PhD thesis, University of California, Davis, Davis, CA, 2007.

[54] W. I. Linor, "Ion energies produced by laser giant pulse," *Appl. Phys. Lett.*, vol. 3, pp. 210–211, 1963.

[55] M. Borghesi, D. Campbell, A. Schiavi, M. Haines, O. Willi, A. MacKinnon, P. Patel, L. Gizzi, M. Galimberti, and R. Clarke, "Electric field detection in laser-plasma interaction experiments via the proton imaging technique," *Phys. Plasmas*, vol. 9, p. 2214, 2002.

[56] J. Fuchs, T. Cowan, P. Audebert, H. Ruhl, L. Gremillet, A. Kemp, M. Allen, A. Blazevic, J. Gauthier, and M. Geissel, "Spatial uniformity of laser-accelerated ultrahigh-current mev electron propagation in metals and insulators," *Phys. Rev. Lett.*, vol. 91, no. 25, p. 255002, 2003.

[57] S. Kar, K. Markey, P. Simpson, C. Bellei, J. Green, S. Nagel, S. Kneip, D. Carroll, B. Dromey, and L. Willingale, "Dynamic control of laser-produced proton beams," *Phys. Rev. Lett.*, vol. 100, no. 10, p. 105004, 2008.

[58] I. Baraffe, "Structure and evolution of giant planets," *The Outer Planets and their Moons*, pp. 67–76, 2005.

[59] A. Mackinnon, P. Patel, R. Town, M. Edwards, T. Phillips, S. Lerner, D. Price, D. Hicks, M. Key, and S. Hatchett, "Proton radiography as an electromagnetic field and density perturbation diagnostic (invited)," *Rev. Sci. Instrum.*, vol. 75, p. 3531, 2004.

[60] A. Mackinnon, P. Patel, M. Borghesi, R. Clarke, R. Freeman, H. Habara, S. Hatchett, D. Hey, D. Hicks, and S. Kar, "Proton radiography of a laser-driven implosion," *Phys. Rev. Lett.*, vol. 97, no. 4, p. 45001, 2006.

[61] S. Fritzler, V. Malka, G. Grillon, J. Rousseau, F. Burgy, E. Lefebvre, P. Mckenna, and K. Ledingham, "Proton beams generated with high-intensity lasers: Applications to medical isotope production," *Applied physics letters*, vol. 83, p. 3039, 2003.

[62] S. Bulanov and V. Khoroshkov, "Feasibility of using laser ion accelerators in proton therapy," *Plasma Physics Reports*, vol. 28, no. 5, pp. 453–456, 2002.

[63] T. Mason, "Pulsed neutron scattering for the 21st century," *Physics today*, vol. 59, p. 44, 2006.

[64] D. P. Higginson, J. M. Mcnaney, D. C. Swift, T. Bartal, D. S. Hey, R. Kodama, S. L. Pape, A. Mackinnon, D. Mariscal, H. Nakamura, N. Nakanii, K. A. Tanaka, and F. N. Beg, "Laser generated neutron source for neutron resonance spectroscopy," *Phys. Plasmas*, vol. 17, p. 100701, Jan 2010.

[65] D. Strickland and G. Mourou, "Compression of amplified chirped optical pulses," *Optics Communications*, vol. 56, no. 3, pp. 219 – 221, 1985.

[66] N. K. Moncur, R. P. Johnson, R. G. Watt, and R. B. Gibson, "Trident: a versatile high-power nd:glass laser facility for inertial confinement fusion experiments," *Appl. Opt.*, vol. 34, pp. 4274–4283, Jul 1995.

[67] S. Batha, R. Aragonez, and F. Archuleta, "Trident high-energy-density facility experimental capabilities and diagnostics," *Review of Scientific . . .*, Jan 2008.

[68] R. Shah, R. Johnson, T. Shimada, K. Flippo, J. Fernandez, and B. Hegelich, "High-temporal contrast using low-gain optical parametric amplification," *Optics Letters*, vol. 34, no. 14, pp. 2273–2275, 2009.

[69] S. A. Gaillard, *Increased Proton Energies - Above the $\sim$ 60 MeV Empirical Barrier, From High-Contrast High-Intensity Short-Pulse Laser-Interactions with Micro-Cone Targets.* PhD thesis, University of Nevada, Reno, Reno, NV, 2008.

[70] R. Baumgartner and R. Byer, "Optical parametric amplification," *Quantum Electronics, IEEE Journal of*, vol. 15, pp. 432 – 444, jun 1979.

[71] C. Dorrer, I. Begishev, A. Okishev, and J. Zuegel, "High-contrast optical-parametric amplifier as a front end of high-power laser systems," *Optics Letters*, vol. 32, no. 15, pp. 2143–2145, 2007.

[72] F. Nürnberg, M. Schollmeier, E. Brambrink, A. Blažević, D. Carroll, K. Flippo, D. Gautier, M. Geißel, K. Harres, and B. Hegelich, "Radiochromic film imaging spectroscopy of laser-accelerated proton beams," *Rev. Sci. Instrum.*, vol. 80, p. 033301, 2009.

[73] "GAFCHROMIC website: http://www.gafchromic.com," 2011.

[74] "Crocker Nuclear Laboratory website: http://www.crocker.ucdavis.edu," 2011.

[75] "XFEL website: http://www.srim.org/," 2011.

[76] D. Hey, M. Key, A. MacKinnon, A. MacPhee, P. Patel, R. Freeman, L. V. Woerkom, and C. Castaneda, "Use of gafchromic film to diagnose laser generated proton beams," *Rev. Sci. Instrum.*, vol. 79, p. 053501, 2008.

[77] D. T. Offermann, *The Effect of Erbium Hydride on the Conversion Efficiency to Accelerated Protons from Ultra-short Pulse Laser Irradiated Foils.* PhD thesis, The Ohio State University, Columbus, OH, 2008.

[78] D. Welch, D. Rose, B. Oliver, and R. Clark, "Simulation techniques for heavy ion fusion chamber transport* 1," *Nuclear Instruments and Methods in Physics Research Section A: Accelerators, Spectrometers, Detectors and Associated Equipment*, vol. 464, no. 1-3, pp. 134–139, 2001.

[79] B. I. Cohen, A. B. Langdon, D. W. Hewett, and R. J. Procassini, "Performance and optimization of direct implicit particle simulation," *Journal of Computational Physics*, vol. 81, no. 1, pp. 151 – 168, 1989.

[80] C. Bellei, M. Foord, T. Bartal, M. Key, H. McLean, P. Patel, R. Stephens, and F. Beg, "Electron and ion dynamics during the expansion of a laser-heated plasma under vacuum," *Submitted for Publication*, 2012.

[81] P. Mora, "Thin-foil expansion into a vacuum," *Phys. Rev. E*, vol. 72, no. 5, p. 56401, 2005.

[82] J. King, K. Akli, R. Freeman, J. Green, S. Hatchett, D. Hey, P. Jamangi, M. Key, J. Koch, and K. Lancaster, "Studies on the transport of high intensity laser-generated hot electrons in cone coupled wire targets," *Phys. Plasmas*, vol. 16, p. 020701, 2009.

[83] M. H. Key, R. R. Freeman, S. P. Hatchett, A. J. Mackinnon, P. K. Patel, R. A. Snavely, and R. B. Stephens, "Proton fast ignition," *Fusion Sci. Technol.*, vol. 26, pp. 440–452, 2006.

[84] C. Li, F. Séguin, J. Frenje, J. Rygg, R. Petrasso, R. Town, P. Amendt, S. Hatchett, O. Landen, and A. Mackinnon, "Measuring e and b fields in laser-produced plasmas with monoenergetic proton radiography," *Phys. Rev. Lett.*, vol. 97, no. 13, p. 135003, 2006.

[85] T. Yabuuchi, H. Sawada, T. Bartal, D. Batani, L. Gizzi, M. Key, A. Mackinnon, H. McLean, P. Norreys, P. Patel, R. Stephens, C. Spindloe, W. Theobald, M. Wei, and F. Beg, "Proton radiography of intense laser irradiated wire-attached cone targets," *IEEE Transactions on Plasma Science*, vol. 39, no. 11, pp. 2822–2823, 2011.

[86] T. Ma, A. MacPhee, M. Key, S. Hatchett, K. Akli, T. Barbee, C. Chen, R. Freeman, J. King, and A. Link, "Determination of electron-heated temperatures of petawatt laser-irradiated foil targets with 256 and 68 ev extreme ultraviolet imaging," *Rev. Sci. Instrum.*, vol. 79, p. 093507, 2008.